MILANKOVITCH VERSUS THE COMET: CYCLIC AND CATASTROPHIC CLIMATE FORCING AT THE PALEOCENE/EOCENE BOUNDARY

by BENJAMIN STOVALL CRAMER

A Dissertation submitted to the

Graduate School-New Brunswick

Rutgers, The State University of New Jersey

in partial fulfillment of the requirements

for the degree of

Doctor of Philosophy

Graduate Program in Geological Sciences

written under the direction of

Kenneth G. Miller

and approved by

____

____

____

____

____

New Brunswick, New Jersey

October 2002

ABSTRACT OF THE DISSERTATION

Milankovitch versus the Comet: Cyclic and Catastrophic Climate Forcing at the Paleocene/Eocene Boundary

by BENJAMIN STOVALL CRAMER

Dissertation Director:

Kenneth G. Miller

I demonstrate that a large perturbation in the global carbon isotope record at the Paleocene/Eocene boundary is mirrored in smaller pertubations throughout the late Paleocene–early Eocene. The smaller perturbations occur at maxima in the eccentricity of Earth's orbit around the Sun and are the expected result of precession forcing of a system with a built-in long time constant, i.e. the residence time of carbon. The carbon isotope excursion at the Paleocene/Eocene boundary is different both in amplitude and in timing: it is roughly twice as large as any of the other perturbations and occurs out of phase with maxima in eccentricity. This suggests that the trigger for the Paleocene/Eocene carbon isotope excursion was not integral to the biogeochemical carbon cycle. A plausible catastrophic explanation for the carbon isotope excursion is a comet impact, and I present data supporting an impact at the Paleocene/Eocene boundary.

PREFACE

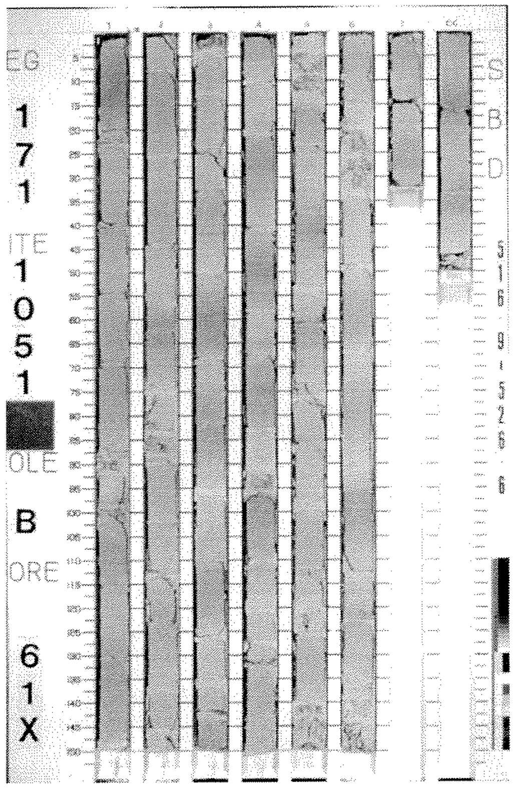

Step back and look at the image above, ignoring for a moment the fact that it is a photograph of a sediment core. There are two primary geometric features that stand out: the first is a series of parallel vertical rectangles (the core sections), the second is a series of parallel diagonals alternating light and dark. The diagonals are created as an interference pattern between two elements: the 1.5 m section length and a $\sim$25 cm alternation of dark and light intervals in the core. The regularity of the interference pattern indicates that both elements are periodic. The 1.5 m section length is periodic because the core was cut to that length. The $\sim$25 cm alternation is periodic because of a sedimentary response to orbital forcing of insolation at the time of deposition. The interference pattern might therefore be called the hallmark of Milankovitch, the defining feature of Earth's climate.

ACKNOWLEDGEMENTS

Table of Contents

Title Page ii

Abstract iii

Preface iv

Acknowledgements v

Table of Contents vi

List of Tables x

List of Figures xi

Introduction 1

1 Latest Paleocene-earliest Eocene cyclostratigraphy: Using core photographs for reconnaissance geophysical logging 5

1.1 Abstract 5

1.2 Introduction 6

1.2.1 Latest Paleocene-earliest Eocene chronostratigraphy 9

1.3 Methods 11

1.4 Evaluation of the accuracy of the logs 14

1.4.1 Hole 1051A: Comparison with spectrophotometer measurements 14

1.4.2 Hole 690B: Comparison with XRF Ca and Fe intensity 17
1.4.3 Summary 17
1.5 Chron C24r cyclostratigraphy 18
1.5.1 Results 18
1.5.2 Discussion 23
1.5.3 Future work 27
1.6 Conclusions 27

2 Milankovitch and transient carbon isotope events near the Paleocene/Eocene boundary 29

2.1 Abstract 29
2.2 Introduction 30
2.3 Methods and results 31
2.4 Discussion 35
2.4.1 Modeling the δ^{13}C eccentricity response 35
2.4.2 General implications for interpreting δ^{13}C records 40
2.4.3 Implications for the cause of the PETM 41
2.5 Conclusions 42

3 The age of the Paleocene/Eocene boundary: An orbitally tuned integrated carbon isotope, calcareous nannofossil, magnetic polariy, and radioisotope chronology 44

3.1 Abstract 44
3.2 Introduction 45
3.3 Methods and results 47
3.3.1 Material 47
3.3.2 Carbon isotopes 48

3.3.3 Geophysical logs 50
3.3.4 Magnetostratigraphy 51
3.3.5 Error analysis 52
3.4 Construction of the astronomical timescale 54
3.4.1 The framework 54
3.4.2 Temporal representation 58
3.4.3 Integration of magneto- and biostratigraphy 60
3.5 Discussion 62
3.6 Conclusion 68

4 A comet impact trigger for the Paleocene/Eocene thermal maximum and carbon isotope excursion? 70

4.1 Abstract 70
4.2 Introduction 71
4.3 Magnetic nanoparticles at the CIE 71
4.4 Lithologic changes at the CIE 75
4.5 Other evidence for an impact 77
4.6 Estimate of comet size from carbon isotope evidence 78
4.7 Contribution from gas hydrates 80
4.8 Greenhouse warming 81
4.9 Conclusions 82

5 Synthesis 83

5.1 Introduction 83
5.2 Astronomical tuning in the absence of a calculated target curve . . . 85
5.3 Carbon isotope transients: artifact or climate signal? 90
5.4 Estimating residence-time from the autocovariance of δ^{13}C records . . 92

5.5 Milankovitch forcing during the PETM 94

5.6 Coda 96

A Core Photo Processing **98**

A.1 Introduction 98

A.2 Image theory 100

A.3 Pre-processing 105

A.4 The control panel 106

A.4.1 File Access 106

A.4.2 Manipulation (tabs) 107

A.4.3 Geometry 107

A.4.4 Sections 107

A.4.5 Color 110

A.4.6 Export 111

A.4.7 Marquee 113

Curriculum Vita **129**

List of Tables

1.1 Levels used for stratigraphic correlation in Holes 1051A and 690B. . . 13

1.2 Comparison of durations from cycle counts and previous timescales. . 19

3.1 Calibrated ages of eccentricity maxima. 56

3.2 Sample identifications and calibrated ages of miscellaneous stratigraphic marker events. 56

3.3 Sample identifications and calibrated ages of magnetic polarity reversals. 61

3.4 Sample identifications and calibrated ages for nannofossil zonal boundaries. 63

3.5 Calibrated ages of various stratigraphic marker events surrounding the Paleocene/Eocene boundary. 64

5.1 Estimates of the residence time for carbon based on δ^{13}C records. . . 93

3.5 Stacked δ^{13}C record, paleomagnetic inclinations, and nannofossil zonations. 55
3.6 Geophysical logs for Sites 550, 690 and 1051. 57
3.6 Geophysical logs (cont.). 58
3.6 Geophysical logs (cont.). 59
3.7 Comparison of published durations for magnetic polarity zones. . . . 65
3.8 Evolution of the $\sim$0.4 m.y. eccentricity period over 200 Ma. 67
3.9 Phase comparison calculated and δ^{13}C -based eccentricity cycles. . . . 68

4.1 Location map for Ancora, Bass River, and Clayton drill sites. 72
4.2 Hysteresis loop and theoretical grain size dependence. 73
4.3 Lithologic, isotopic and magnetic hysteresis profiles across the CIE interval in New Jersey. 74
4.4 TEM bright field image of a magnetite grain. 75
4.5 Iridium concentrations from Zumaya and δ^{13}C records from Zumaya and Site 690. 77
4.6 Mass of carbon required to produce a -1 ‰ shift in the carbon reservoir. 80

5.1 Sedimentation rates based on precession cycle identification. 87
5.2 Eccentricity-forced variations in precession cycle duration. 88
5.3 Bulk sediment δ^{13}C and δ^{18}O records. 90
5.4 Benthic foraminiferal δ^{13}C and δ^{18}O records. 91
5.5 Modeled CIE response compared with records from Sites 690 and 1051 94

Introduction

Cyclic variations in insolation, due to variations in the eccentricity and obliquity of Earth's orbit and the precession of Earth's spin axis, have long been accepted as a significant feature of Earth's climate, producing recognizable cyclic features in many sedimentary successions. In recent decades, orbitally forced lithologic cyclicity has been widely and successfully used to produce cyclostratigraphies providing precise constraints on sedimentation rate models in a wide variety of environments (e.g. [52, 55, 56, 97, 99, 118, 140]. However, in the pivotal publication by Hays et al. [51] that identified Milankovitch as the Pacemaker of the Ice Ages the emphasis was on orbital forcing as a paradigm for understanding Earth's climate rather than as a chronologic tool. This paradigm has been underemphasized in investigations of pre-Pleistocene climate change.

As with any nascent science, paleoceanography has been primarily a descriptive science with a substantial amount of research devoted to the simple cataloguing of events in geologic history. After several decades, we now have an reasonably good understanding of what happened to Earth's climate and when for the last $\sim$100 m.y. We have a much poorer understanding of why. Paleoceanographic explanations of why events happened have dominantly been speculative scenarios tying together events that appear to have occurred at roughly the same time, often with surprisingly little regard for the plausibility of proposed cause-and-effect relationships. Paleoceanographers have also naturally gravitated toward big historical events, to the detriment of understanding climate variability during the more mundane intervals that account for most of geologic time.

The Milankovitch climate paradigm suggests a different strategy for paleoceanographic research. On the one hand, it provides a framework for investigating the mundane parts of the geologic record. Rather than simply being thick, dull, repetitive successions, the repetitions are archives recording climate variability in response to a highly predictable forcing mechanism. There is vast potential for understanding the mechanisms of climate change in any part of the geologic record by identifying the amplitude and timing of the Milankovitch response in various climate proxies. On the other hand, the variability of climate in response to Milankovitch provides a much needed context for understanding big events, either emphasizing their anomalous nature or revealing them as the expected result of modulation of the insolation forcing.

The shift from descriptive history to empirical climate research has more or less been completed in Pleistocene paleoceanography [15, 48, 49, 50, 51, 57, 58, 59, 98, 102, 117] and the level of detail has increased so that sub-Milankovitch cyclicity is now the major thrust of research [16, 17, 18, 19, 24, 48, 86, 87]. There are relatively very few studies that have attempted to apply the Milankovitch paradigm in pre-Pleistocene paleoceanography, other than as a primarily chronologic tool [80, 85, 147]. These few studies clearly demonstrate the necessity of understanding the Milankovitch context as they reveal that the timing of the major steps in the growth of ice during the Neogene resulted from insolation forcing.

In this dissertation I lay the groundwork for a revised understanding of the Paleocene/Eocene thermal maximum (PETM) in the context of Milankovitch forcing. The PETM is an anomalous event marked by a large carbon isotope excursion, indicating the input of a large volume of ^{12}C-poor carbon into the ocean-atmosphere reservoir, and a synchronous oxygen isotope excursion, indicating that global temperatures exceeded those recorded at any other time in the Cenozoic [10, 22, 65, 67, 132, 133, 149, 151]. These geochemical events are accompanied by evolutionary changes among numerous groups, most prominently a major benthic foraminiferal extinction [65, 132, 133] and a significant turnover in mammalian faunas [46]. The last decade has witnessed the publication of a voluminous literature on the PETM, including several volumes resulting from scientific meetings specifically dealing with the Paleocene-Eocene transition, to which the reader is referred for background information [8, 46, 71, 115, 143].

In the first three chapters, I establish an astrochronology for the Paleocene–Eocene boundary interval. In Chapter 1 I present a method for constructing usable geophysical logs from core photographs. This is supplemented in Appendix A by a procedure file and accompanying help file written for Wavemetrics Igor Pro that implements a graphical user interface for generating these logs. Chapter 1 also presents preliminary cyclostratigraphies for the ODP Site 1051 and 690 uppermost Paleocene–lowermost Eocene sections. The correlation of the two cyclostratigraphies highlights the problems inherent in using precessional cyclicity alone to establish a cycle-based chronology, mainly that the errors can easily be greater than the errors involved in bio- and magnetostratigraphic techniques. To circumvent this problem, it is crucial to be able to confidently identify eccentricity cycles, which provide a more reliable chronometer simply by virtue of being longer duration and therefore not so susceptible to systematic error. In Chapter 2 I demonstrate that carbon isotope records provide a reliable eccentricity proxy as a result of the residence time of carbon being of the same order as the eccentricity period. In Chapter 3 I extend the carbon isotope method in conjunction with sediment color and magnetic susceptibility logs to establish a chronology for the latest Paleocene-earliest Eocene. While this astrochronology is in some sense hanging, as it is not directly tied to calculated orbital solutions or to the present, it is tied to the $^{40}Ar/^{39}Ar$ chronologic framework using ash layers present at DSDP Site 550.

Although much of this thesis is concentrated on establishing an orbital chronology, the paleoceanographic implications of the orbital framework are, to me, of more fundamental importance. Chapter 2 is meant to demonstrate that prominent events in the geologic record, such as the PETM, cannot be fully understood without examining the geologic record away from such events at equivalent resolution. The carbon isotope records presented in Chapter 2 conclusively demonstrate that the PETM cannot be explained as an amplified response to orbital forcing. Evidence for a comet impact at the onset of the PETM, which would explain the anomalous timing of the event, is provided in Chapter 4. The final chapter synthesizes the implications of the preceding chapters and includes more speculative ideas regarding the influence of Milankovitch on the detailed evolution of the PETM.

Chapter 1

Latest Paleocene-earliest Eocene cyclostratigraphy: Using core photographs for reconnaissance geophysical logging*

1.1 Abstract

I present a new method for reconnaissance cyclostratigraphic study of continuously cored boreholes: the generation of detailed sediment color logs by digitizing Ocean Drilling Program (ODP) core photographs. The reliability of the method is tested by comparison with the spectrophotometer color log for the uppermost Paleocene-lowermost Eocene section (Chron C24r) at ODP Hole 1051A. The color log generated from Hole 1051A core photographs is essentially identical to the spectrophotometer log. The method is applied to the Chron C24r section at Holes 1051A and 690B, producing the first high-resolution geophysical log for the latter section. I calculate astronomically calibrated durations between bio- and chemostratigraphic events within Chron C24r by correlating the cyclostratigraphies for Holes 1051A and 690B. These durations are significantly different from previous estimates, indicating that the chronology of events surrounding the Paleocene/Eocene boundary will have to be revised. This study demonstrates that useful geophysical logs can be generated from digitized ODP and DSDP core photographs. The method is

*B.S. Cramer, *Earth and Planetary Science Letters*, 186:231-244, 2001.

of practical use for sections lacking high-resolution logs, as is the case for most lower Paleogene sections.

1.2 Introduction

Since the recognition of "Milankovitch" orbital forcing as the "pacemaker of the ice ages" [51], cyclostratigraphy has become widely used as a metronome to parse time in the geologic record at a resolution of 10-100 k.y. (e.g. [56, 97, 119]). Cyclostratigraphy is the only known method useful throughout the geologic record for correlation of the stratigraphic record to a numerical timescale at such a high resolution. Where cyclostratigraphies can be linked to the present, they have superseded radiometric dating as the primary tool for estimating the ages of events in geologic time (e.g. [107, 118]).

In marine sections, numerical ages of specific stratigraphic horizons and sedimentation rates between horizons are typically estimated by correlation with the integrated magnetobiochronologic scale of Berggren et al. [13, ; henceforth BKSA95]. Essentially, BKSA95 correlates the Cenozoic planktonic foraminiferal and calcareous nannoplankton biozonations via magnetostratigraphy with the geomagnetic polarity timescale of Cande and Kent [28, 29, ; henceforth GPTS]. The GPTS exploits the seafloor magnetic anomaly pattern and the hypothesis that seafloor spreading rates vary smoothly through time to calibrate the age of magnetic polarity reversals against an interpolated age for the oceanic crust.

The astronomical polarity timescale (APTS) exploits lithologic cycles in sedimentary successions that can be correlated with cycles in the precession, obliquity, and eccentricity of the Earth's orbit around the Sun. The orbital periodicities are physically predictable, and so sedimentary cycles can be correlated with a calculated history of insolation variations [59]. This allows extremely precise dating of magnetic polarity reversals in the sedimentary record, ideally to within a fraction of an average precession cycle ($\sim$21 k.y.). Consequently, the APTS was used to constrain the seafloor spreading rate curve from the present to 5.23 Ma in the GPTS.

The Earth's orbit is not fully predictable because of chaotic elements and uncertainties in tidal dissipation [77]. As a result, an APTS constructed by direct correlation with the calculated orbital solution is probably only reliable to $\sim$10 Ma. Alternative methods must be used for older sections. Although more sophisticated methods exist, simple cycle counting using the assumption that cycle durations are similar to the present is a useful first step in evaluating the durations of biochrons estimated in BKSA95 [54]. It must be emphasized that the assumption that cycles reflect orbital forcing is not tested by cycle counting. This assumption can be bolstered if 1) the cycle counts are approximately consistent with magnetobiochronology or other age information, 2) the cycles can be shown to be periodic, and 3) the lithologic proxy being used is shown to vary in response to orbital forcing in a similar sedimentary environment.

Cycles are expressed as lithologic changes in sedimentary sections. In order to determine whether such cyclicity is periodic it is necessary to parametrize the lithology. One option is to assign a numerical scale to sediment type and simply characterize the lithology with a number (e.g., [97]). Because it is labor-intensive to generate a high-resolution log in this manner, it is more common to use a core or downhole geophysical log as a lithologic proxy. By default, magnetic susceptibility, GRAPE and spectrophotometer logs have been used because they are rapidly generated with a minimum of equipment (e.g., [119]).

The oxygen isotope records that have been used to calibrate the Plio-Pleistocene APTS are a more direct proxy for Earth's climate (as reflected by the size of continental ice sheets) rather than for lithology. The spectral pattern of variations in $\delta^{18}O$ and consistency with climate models have conclusively demonstrated that these records reflect orbital forcing of climate [51, 59, 118, 119]. They can therefore be taken as a standard example of orbital forcing in a sediment sequence. During the

Plio-Pleistocene prior to 1 Ma, obliquity (41 k.y.) forced fluctuations in the size of ice sheets resulted in variations in $\delta^{18}O$ of amplitude 0.7-1.0 ‰ [118] while during the late Oligocene this amplitude was only 0.5-0.6 ‰ [148]. It is likely that $\delta^{18}O$ measurements are not sufficiently sensitive to resolve orbitally forced changes in early Paleogene ice sheets; even if ice sheets existed during the Paleocene-Eocene they were small and would result in <0.3 ‰ variations in $\delta^{18}O$ on a m.y. timescale [27]. Moreover, using $\delta^{18}O$ in this manner requires closely spaced (~2-4 k.y.) samples and is time consuming and expensive. Hence, the development of cyclostratigraphy virtually requires a cheap, rapid geophysical log.

The effort to use cyclostratigraphy as a correlation tool is hindered by the lack of high-resolution geophysical logs for many of the Deep Sea Drilling Project (DSDP) and Ocean Drilling Program (ODP) sections that have become widely used for paleoceanographic reconstruction, especially in the older record. This study addresses that problem by exploiting the archive of high-quality color core photographs that are available for all DSDP and ODP cores. It is shown here that, by digitizing these photographs, it is possible to generate a high-resolution, accurate sediment color log with minimal effort. Previous studies have used core photographs to generate gray-scale reflectance logs useful for cyclostratigraphic (e.g. [53, 54]) and sedimentologic (e.g. [23]) analysis. This study builds on that work by 1) demonstrating that background lighting effects can be corrected, allowing more rigorous analysis of the spectral content of the logs, and 2) utilizing the color information contained in core photographs rather than simply grayscale.

Sediment color logs generated from core photographs are tested against direct spectrophotometer measurements of color reflectance [100]. The spectrophotometer log available for ODP Hole 1051A [100] provides a direct means of evaluating the accuracy of logs generated from core photographs as a measurement of sediment color. Because the spectrophotometer log and the log generated from core photographs measure the same parameter (sediment color) on the same core, correlation between them

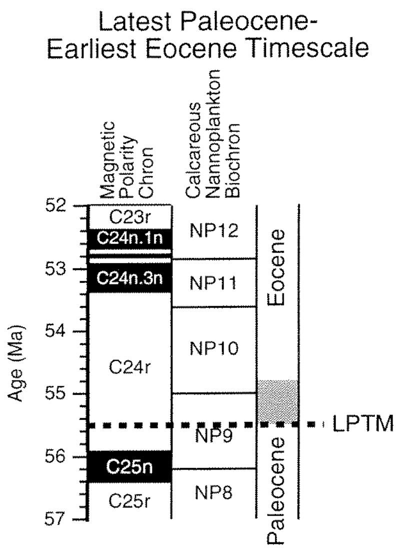

Figure 1.1: Integrated magnetobiostratigraphic timescale for the latest Paleocene-earliest Eocene (after [13], with the age of the LPTM from [6]).

should be high regardless of the forcing mechanism or sedimentation rate changes. The method also produces similar results to recently published XRF Fe and Ca intensity logs [109] in a ~7 m section in ODP Hole 690B.

1.2.1 Latest Paleocene-earliest Eocene chronostratigraphy

I demonstrate the potential utility of color logs by constructing a cycle-based correlation between the latest Paleocene-earliest Eocene (magnetic polarity Chron C24r) sections in ODP Holes 690B and 1051A (Figure 1.1). Chron C24r has received special attention recently for two primary reasons. 1) It contains the latest Paleocene thermal maximum (LPTM), a runaway greenhouse event that has been the subject of intensive study over the last decade (e.g. [35, 65, 67, 149]). 2) It contains the Paleocene/Eocene Series boundary and all candidate levels being considered by the International Global Correlation Project (IGCP) Project 308 for redefinition of the P/E boundary (e.g. [4]). The sections from ODP Sites 690 and 1051 are crucial both to the study of the LPTM (e.g. [10, 65, 67, 95, 109]) and to the construction of a Chron

C24r chronostratigraphy (e.g. [6, 95]. However, logs suitable for cyclostratigraphic analysis have only been available for Site 1051.

Attempts at magnetobiostratigraphic correlation between Chron C24r sections have concluded that very few, if any, sections are complete through all of Chron C24r [6, 7]. As a result, stratigraphic correlation between sites has not been straightforward. The BKSA95 calibration of biostratigraphic datums within Chron C24r and the calibration for the age of the LPTM by Aubry et al. [6] (Figure 1.1) relies on splicing the sections from Hole 690B and DSDP Hole 550 using biostratigraphic and isotopic correlation [3, 6]. The interpolation of ages within the 690B-550 composite section must be tested by constructing a cycle-based chronostratigraphy.

In constructing the 690B-550 composite section, realized that the 55 Ma tiepoint used in estimating the seafloor spreading history that forms the basis for the GPTS was substantially in error. This age was calculated for the NP9/NP10 contact at DSDP Site 550 by extrapolating sedimentation rates down from two $^{40}Ar/^{39}Ar$ dated ash layers which occur within Zone NP10 [129]. Aubry et al. [6] determined that the NP9/NP10 contact is unconformable at Hole 550 and that the tiepoint used in constructing the GPTS was misplaced. In order to maintain consistency with both the GPTS and the original radiometric dates at Hole 550, the NP9/NP10 Zonal boundary was fixed at 55 Ma in BKSA95, despite the recognition that this was inconsistent with extrapolation of sedimentation rates derived from magnetostratigraphy [3, 6]. As a result, the durations of Zones NP9 and NP10 given in BKSA95 were almost guaranteed to be wrong.

Recently, a section was drilled at Site 1051 that is likely complete through Chron C24r and appears to have a good magnetic polarity record [100]. A cyclostratigraphic calibration of the age of the LPTM relative to the base of Chron C24r has been proposed using magnetic susceptibility and Fe intensity logs at Site 1051 [95]. This was the first application of cyclostratigraphy in Chron C24r, primarily because nearly all other LPTM sites lack high-resolution geophysical logs. Fe and Ca intensity logs

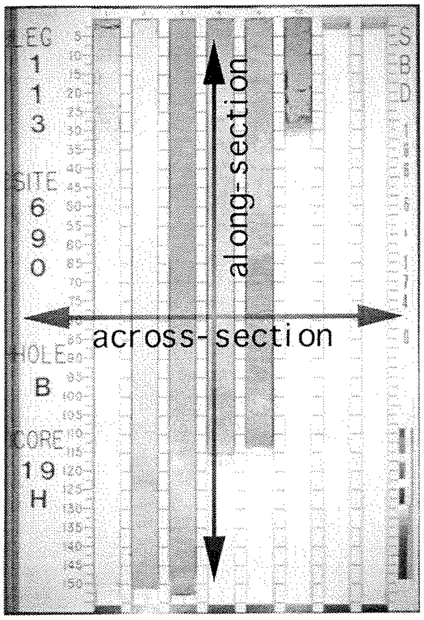

Figure 1.2: Illustration of typical ODP core photograph. Photographs are obviously darker at the edges than in the center. The model used to correct for this lighting effect is illustrated by the arrows: correction is first made for along-section variations in lighting and then for variations in lighting between sections.

have also been generated for a ~7 m section containing the LPTM in Hole 690B and were used to facilitate cycle-based correlation of the LPTM interval between Sites 690 and 1051 [109]. The cycle-based age of ~54.94-54.96 Ma for the LPTM is at odds with the estimate of 55.52 Ma based on interpolation of sedimentation rates between the base of C24r and the top of Zone NP9 at Site 690 [6]. It is also at odds with the 55 Ma age assigned to the base of Zone NP10 [6, 13], a level which is stratigraphically above (and therefore must be younger than) the LPTM.

1.3 Methods

Core photographs (35 mm color slides) obtained from ODP were digitized using a flatbed scanner at a resolution of 1200 ppi (pixels per inch), which results in a scaling of approximately 1 pixel in the digitized photograph per mm in the actual core. Each photograph displays one ODP core, with sections of the core arranged parallel to one another (Figure 1.2). Individual sections were cropped from the photograph using Adobe Photoshop 4.0 for macintosh and rescaled with a standard scaling factor of 1 pixel per mm in the actual core (a 1.5 m section is then 1500 pixels long). Processing of the photographs into a color log was performed by a macro written for Wavemetrics Igor Pro 3.14 for macintosh. Color logs reflect the mean value for each row of pixels in the central 3 cm of each core, resulting in a "sampling" interval equivalent to 1 mm. The resulting log contains three channels, representing red, green, and blue (RGB) values of the digitized photograph.

The effects of lighting are clearly visible in the photographs, with the edges of the photograph darker than the center, and the bulk of the processing macro is devoted to correcting for the background lighting. I remove the background using a simplistic model in which it is assumed that the lighting effects can be characterized by two third-degree polynomials, one along-section and one across-section (Figure 1.2). Third degree polynomials are appropriate because the lighting effect results from a line rather than a point source. The along-section background is approximated by averaging all sections from a single core and performing a least-squares fit of a third-degree polynomial to the resulting curve. The across-section background is approximated by calculating a mean value for each section (after correcting for along-section background), identifying these values by tray position in the photograph, and performing a least-squares fit to the resulting distribution of values for all cores analyzed from an individual hole. Although this model is not sophisticated, it is sufficient for the cores analyzed here.

Core depths (mbsf: meters below seafloor) were adjusted by removing all voids and contracting cores for which the measured length is longer than the drilled length (adjusted depths are given the units ambsf). This preserves the logged depth at the top of every core. For analysis, I have resampled the logs at 2 cm (using adjusted depths) equivalent sampling interval by taking the mean value in each 2 cm length.

Separate Blackman-Tukey spectra using a triangular window were calculated for each of the red, green, and blue channels and then averaged to obtain a spectral estimate for the lithologic variations. Evolutive spectra were calculated using a win-

Stratigraphic datum levels				
	Hole 1051A depths		Hole 690B depths	
Datum	mbsf	adj. mbsf	mbsf	adj. mbsf
Base C24n	450.75	450.677	—	—
Base NP11	460.65	460.611	137.8	137.652
Base NP10	—	—	148.9	148.874
LPTM	coring gap	513	170.26	170.26
Base C24r	524.5	524.5	—	—
Base NP9	528.95	528.815	185.9	185.9

Table 1.1: Levels used for stratigraphic correlation in Holes 1051A and 690B. Note that errors due to sampling interval are ignored here and in the discussion in the text. The level of the LPTM is approximated based on the record in Hole 1051B.

dow length of 10 m with a step of 5 m between analyses. A Gaussian filter was used to remove variation with wavelength >10 m prior to calculation of evolutive spectra.

Because cycle counting provides no significance test for cycle recognition, there is an inherent error due to non-cyclic variations (i.e. noise) in lithology. In order to estimate the magnitude of this error, minimum and maximum cycle counts were made using conservative and liberal criteria for cycle recognition. Bandpass filters were designed to visually enhance the dominant cyclicity in each section; a large bandwidth was used to minimize forcing the signal into the wavelength of the filter. Counting was performed on the original logs, using filtered logs as a reference. An estimate was made for the number of cycles missing in coring gaps based on an assumption of constant cycle length. Cycle counts were converted to temporal duration by assuming an average precessional cycle length of 0.021 m.y. [54].

Published magneto- and biostratigraphies were used to tie the cyclostratigraphy to the integrated magnetobiostratigraphic timescale [13] (Table 1.1). Calcareous nannoplankton biozonations were assigned using the definitions of Martini [83] as discussed in BKSA95 and Aubry et al. [6]. For Hole 690B, calcareous nannoplankton biostratigraphy was taken from Aubry et al. [6] and Pospichal and Wise [105]. Ali et al. [1] made a careful paleomagnetic study of Hole 690B and concluded that the polarity record primarily represents a drilling overprint rather than the original magnetization of the sediment. The extent of Chron C24r in the section is obscured by this overprint. For Hole 1051A, the calcareous nannoplankton biostratigraphy and magnetostratigraphy were taken from the Site Report [100]. The LPTM can also be used as a point of stratigraphic correlation. The level of the LPTM in Hole 690B was taken from [67]. Although the LPTM occurs in a coring gap in Hole 1051A, the event was recovered at Hole 1051B [10, 65]. The error introduced by extrapolation to the level of the LPTM within the coring gap in Hole 1051A is minimal and can be evaluated by comparison with the analysis of Norris and Röhl [95]. Hole 1051A was used here rather than Hole 1051B because of the better delineation of magnetic polarity reversals and biostratigraphic zones in the former. For the sake of simplicity I assume that all magnetobiostratigraphic horizons are associated with discrete depths (Table 1.1), ignoring error in the location of those horizons.

1.4 Evaluation of the accuracy of the logs

1.4.1 Hole 1051A: Comparison with spectrophotometer measurements

Shipboard spectrophotometer measurements for Hole 1051A, taken at 5 cm intervals [100], are available from ODP. The spectrophotometer directly measures the reflected light intensity in 10 nm wavelength bins. The resulting spectrum can be converted into a tricoordinate color space (i.e., RGB) using standard conversion tables [146]. In this case, the standard CIE (Commission Internationale de lEclairage) XYZ color space was used.

The RGB logs generated from core photographs are measurements made within a tricoordinate color space. In order to compare this with the spectrophotometer log, one log must be converted into the tricoordinate space of the other. Any tricoordinate color space is a linear transform of any other tricoordinate color space, related by the equation [146]:

$$\begin{bmatrix} R' \\ G' \\ B' \end{bmatrix} = \begin{bmatrix} c_{11} & c_{21} & c_{31} \\ c_{12} & c_{22} & c_{32} \\ c_{13} & c_{23} & c_{33} \end{bmatrix} \begin{bmatrix} R \\ G \\ B \end{bmatrix}$$

Consequently, core photograph RGB values should be related to XYZ values through the equation above. Values for the constants (c_{mn}) in this equation must be determined empirically, because they depend on uncontrolled factors such as lighting conditions at the time the photographs were taken, the film used, and the development process. The constants were determined by least-squares fit of the XYZ values to the RGB values, resulting in spectrophotometer logs that can be displayed in color.

There is a very high correlation between sediment color logs from spectrophotometer measurements and core photographs (R (linear correlation coefficient)$= 0.87$ for red, $R = 0.87$ for blue, $R = 0.89$ for green). Visual examination of the two logs shows that variations in the spectrophotometer logs are of slightly larger amplitude than variations in the logs from digitized photos (dark areas are darker and light areas are lighter; Figure 1.3). This may be attributed to a smoothing effect introduced by downsampling the much higher resolution logs from the digitized photos or to the fact that the spectrophotometer gives a linear measure of the intensity of all reflected light while the sensitivity of the slide film is most likely somewhat non-linear with respect to light intensity. In any case, this lower amplitude is of no consequence to cyclostratigraphic analysis.

The power spectrum for the spectrophotometer and photograph logs is also essentially identical (Figure 1.4A). There is one significant difference between the two spectra: the peak at $\sim$0.7 cycles/meter ($\sim$1.4 m wavelength) in the spectrophotometer spectrum is significantly reduced in the digitized photograph spectrum. This is almost certainly the result of the correction for lighting effects at the core section (1.5 m) scale.

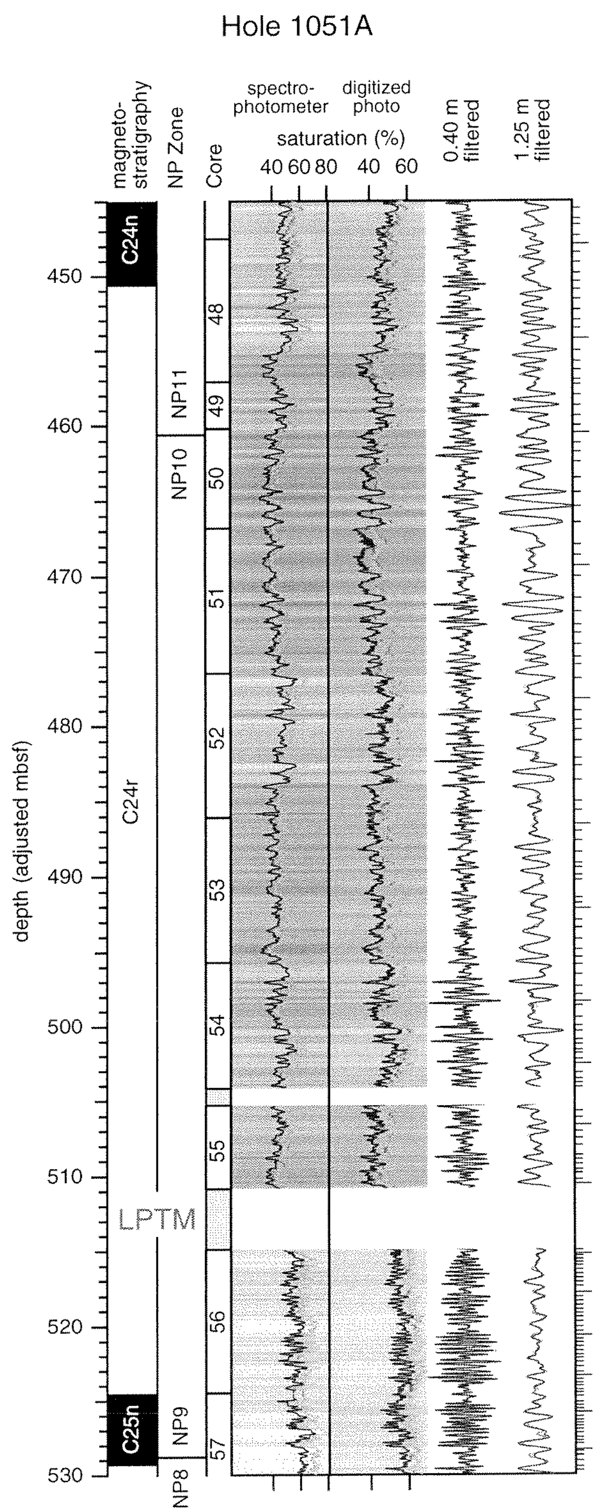

Figure 1.3: Hole 1051A spectrophotometer and digitized photograph color logs. The spectrophotometer log has been fitted to the same color space as the digitized photograph log. The rightmost two traces are the digitized photograph color log bandpass filtered with filters centered on 1.25 and 0.40 m wavelength. In the magnetostratigraphy, black represents normal polarity intervals, white represents reversed polarity intervals, and split black/grey represents intermediate polarity. Ticks along the right side represent best-guess cycle counts, with every 10th cycle emphasized (emphasis uses an estimated cycle count through coring gaps, to be consistent with Table 1.2).

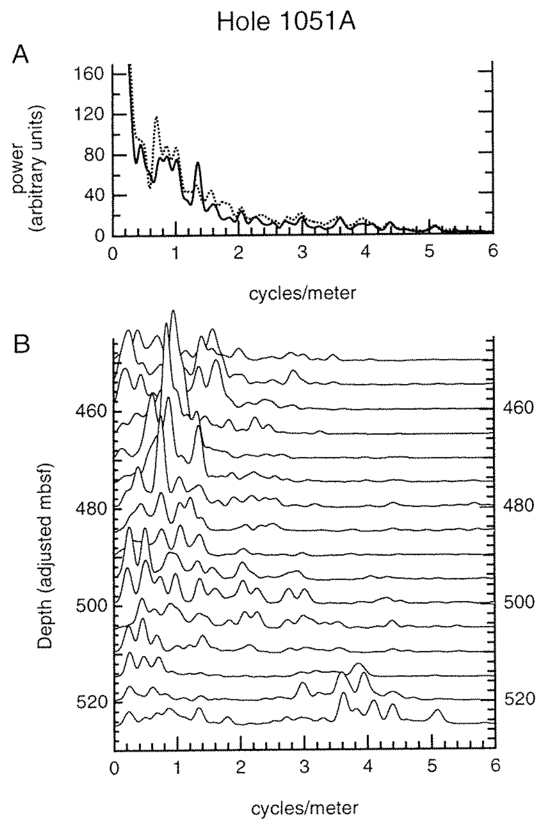

Figure 1.4: Power spectra for Hole 1051A. A: Blackman-Tukey power spectrum (lag 10% of series length) for the digitized photograph color log (solid) and the spectrophotometer color log (dashed). B: Evolutive spectrum (lag 70%) for the digitized photograph color log. Red line traces the evolution of peaks interpreted as reflecting obliquity forcing; blue lines trace two peaks interpreted as reflecting precessional forcing.

1.4.2 Hole 690B: Comparison with XRF Ca and Fe intensity

Röhl et al. [109] have published Ca and Fe intensity logs generated using an XRF scanner for the ~7 m core containing the LPTM in Hole 690B (core 19H). Sediment color logs generated for the same interval are very similar to these logs, especially to the Fe log (Figure 1.5). As Röhl et al. [109] noted, cyclicity disappears in Fe intensity in the upper part of the section and the color logs are similarly affected. Similar intervals (although typically less severe) contribute to the error in cycle counting.

1.4.3 Summary

It is clear from the comparison of core photograph and spectrophotometer logs at Hole 1051A that the former is an accurate measure of sediment color. One shortcoming of

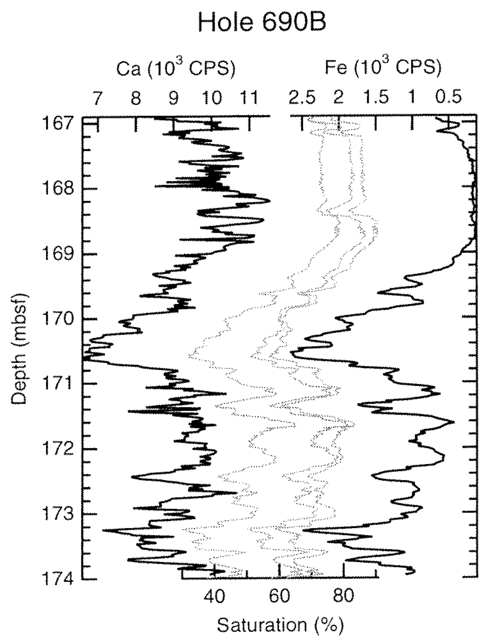

Figure 1.5: Lithologic logs for ODP Core 690B-19H. Heavy lines on the left and right are XRF Ca and Fe counts, respectively (from [109]). Thin lines in the center are saturation in red, green, and blue color channels (refer to Figure 1.6 to identify channels).

these logs results from the necessary correction for background lighting: the amplitude of any cyclicity with a wavelength of ~1.5 m will likely be dampened in the color logs. This observation suggests another probable shortcoming: background lighting effects will be more dominant in sections with smaller amplitude variations in sediment color. In the sections analyzed in this study, the amplitude of sediment color variations is large compared with the background lighting effect. It may be more difficult to create usable color logs for sections in which the amplitude of color variations is of the same magnitude as the background lighting effect.

1.5 Chron C24r cyclostratigraphy

1.5.1 Results

The most well-developed cyclicity at Hole 1051A occurs at 20-30 cm wavelength between 515 and 525 ambsf and at a wavelength of 75-100 cm between 455 and 485 ambsf (Figure 1.3). Cyclicity in the latter interval is not as well developed as in the former.

Cycle-based interval durations					
	Cycle counts		Durations		
Interval	Hole 1051A	Hole 690B	Timescale	Hole 1051A	Hole 690B
Chron C24r	115-157	—	2.557	2.856±0.441	—
Base NP11-Base C24n	14-17	—	0.26	0.33±0.032	—
Zone NP10	—	25-31	1.39	—	0.588±0.063
LPTM-Base NP10	—	48-60	0.52	—	1.134±0.126
Base C24r-LPTM	41-45	—	0.38	0.90±0.042	—
LPTM-Base NP11	60-95	73-91	1.91	1.628±0.368	1.722±0.189
Base NP9-LPTM	59-64	35-40	0.68	1.292±0.053	0.788±0.053

Table 1.2: Comparison of durations between stratigraphic horizons from referenced timescales [6, 13, 29] and from cycle counting at Holes 1051A and 690B. Ranges reflect only the difference between conservative and liberal cycle counts; errors in the position of magnetobiostratigraphic datums are not incorporated in these estimates.

In the evolutive spectrum, the 20-30 cm cyclicity appears as several discrete peaks between 3 and 6 cycles/meter; the 75-100 cm cyclicity appears as a high peak between 0.8 and 1 cycles/meter with several surrounding peaks (Figure 1.4B). The ratio of the peaks between 3 and 6 cycles/meter is consistent with that of the several precessional peaks (16, 19 and 23 k.y. in the Plio-Pleistocene) caused by modulation of precession by eccentricity. It is difficult to trace these peaks upsection, in part due to the coring gap at 510.5-515 ambsf. One possibility is that the very low amplitude peaks in the range 2-3 cycles/meter represent precessional peaks, whereas the high-amplitude peak at $\sim$1 cycle/meter is the result of obliquity forcing. Alternatively, there is a large increase in sedimentation rate between 500 and 490 ambsf (as suggested by [95]) and the several peaks in the range 1-2 cycles/meter are the result of precessional forcing. It is noted that the ratio of the low frequency peaks is not the same as that of the precessional peaks below 510 ambsf. However, cycle counting indicates that the longer cycles must be precessional: if they were obliquity it would require almost a doubling of the duration of Chron C24r (Table 1.2). Bandpass filters were designed to isolate cyclicity with wavelength 15-50 cm (6-2 cycles/m) and 60-150 cm (1.7-0.7 cycles/m) (Figure 1.3). The filtered record clearly demonstrates the poorly developed cyclicity in the interval 495-510 ambsf with well-developed short-wavelength cyclicity below and long-wavelength cyclicity above.

At Hole 690B, well-developed cyclicity occurs at wavelengths of 40-60 cm between 150 and 160 ambsf and between 180 and 185 ambsf (Figure 1.6). Spectral analysis shows several peaks in this range (1.7-2.5 cycles/meter) that are consistent with precessional forcing (Figure 1.7A). Most of the peaks in the spectrum can be explained by Milankovitch forcing with constant sedimentation rate, although there are obvious misfits that suggest some change in sedimentation rate. It is difficult to trace the peaks from the lower part of the section (175-190 ambsf) to the upper part of the section in the evolutive spectrum (Figure 1.7B), primarily because of the perturbation caused by the LPTM (~170 ambsf). Therefore, it is difficult to interpret confidently the dominant peak in the spectrum between 150 and 160 ambsf at ~2 cycles/m (50 cm wavelength) as either precessional or obliquity forcing, although if this is an obliquity peak it suggests a large decrease in sedimentation rate between this interval and the section below. Again, because of magnetobiostratigraphic constraints on the duration represented by this interval [13], the cycle count is more compatible with interpreting this as a precessional peak (Table 1.2). Bandpass filters were designed to isolate precessional cyclicity (30-70 cm wavelength) and obliquity cyclicity (70-130 cm wavelength) (Figure 1.6).

Using the identification of cycles and an assumed average cycle duration of 21 k.y., it is possible to reconstruct sedimentation rates throughout the sections analyzed (Figure 1.8). While sedimentation rates reconstructed for Hole 690B remain essentially constant at ~2 cm/k.y., sedimentation rates for Hole 1051A more than double from ~1.5 cm/k.y. in the lower portion of the section to >3 cm/k.y. in the upper portion. These results are consistent with cycle identification made for parts of these sections by Norris and Röhl [95] and Röhl et al. [109] using Fe and Ca intensity and magnetic susceptibility logs. A minimum and maximum cycle count was made in each section between stratigraphic datums (Table 1.2). The largest error in the cycle

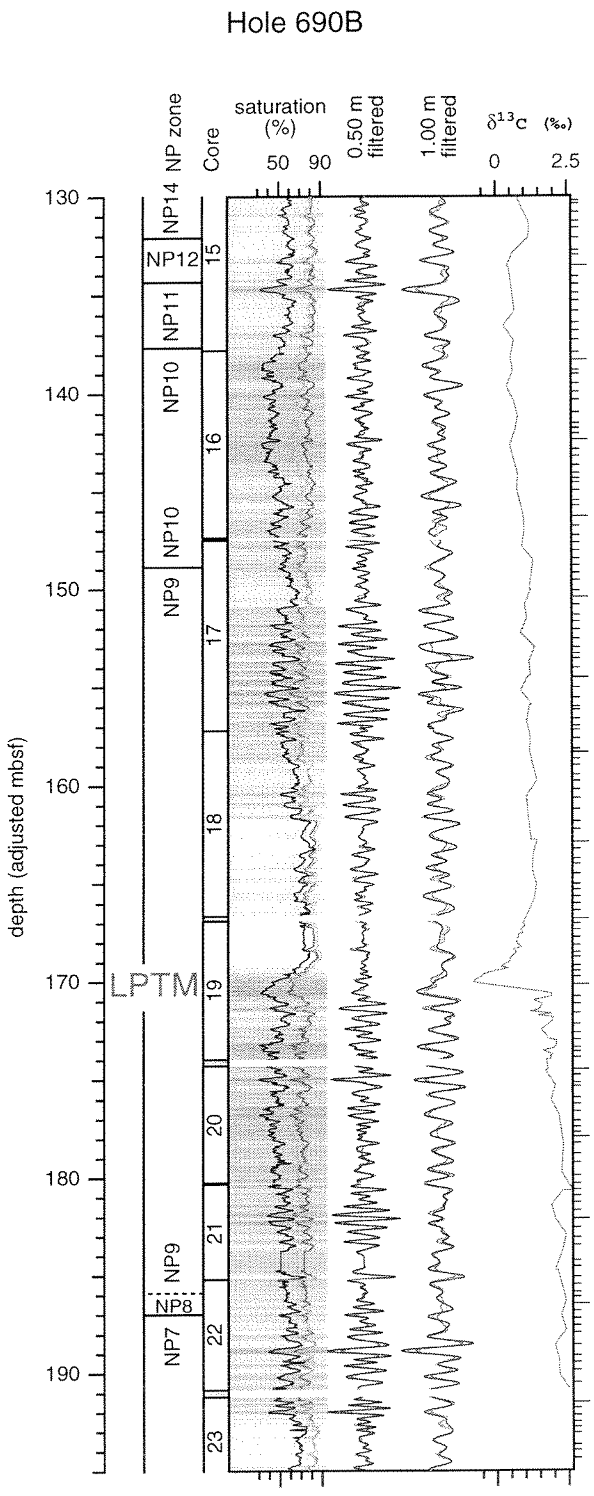

Figure 1.6: Hole 690B digitized photograph color logs and benthic foraminiferal delC record (from [67]). The middle two traces are the color log band-pass filtered with filters centered on 1.00 and 0.50 m wavelength. Ticks along the right side represent best-guess cycle counts, with every 10th cycle emphasized.

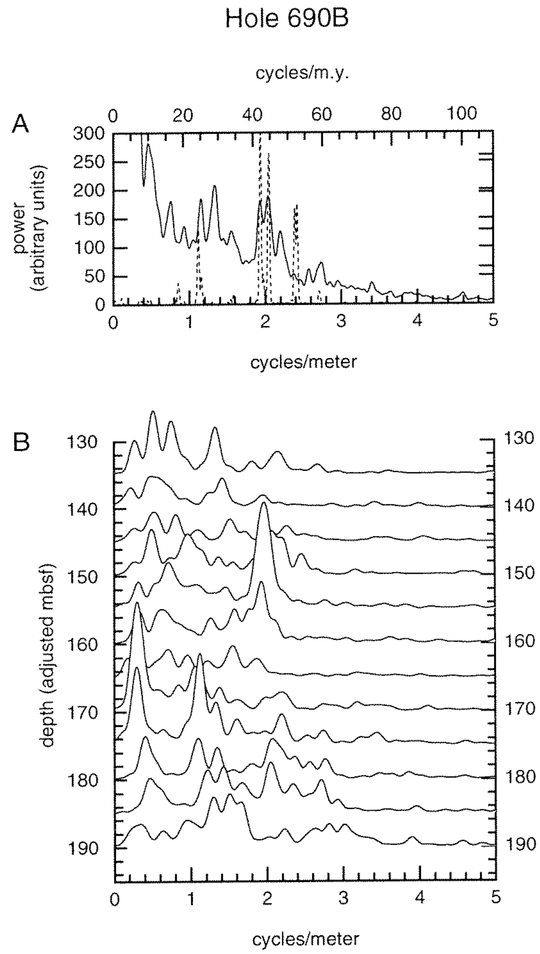

Figure 1.7: Power spectra for Hole 690B. A: Blackman-Tukey power spectrum (lag 20%) for the digitized photograph color log (solid, plotted against bottom axis) and calculated mean January insolation at 60S (dashed, plotted against top axis) [77]. B: Evolutive spectrum (lag 70%) for the color log.

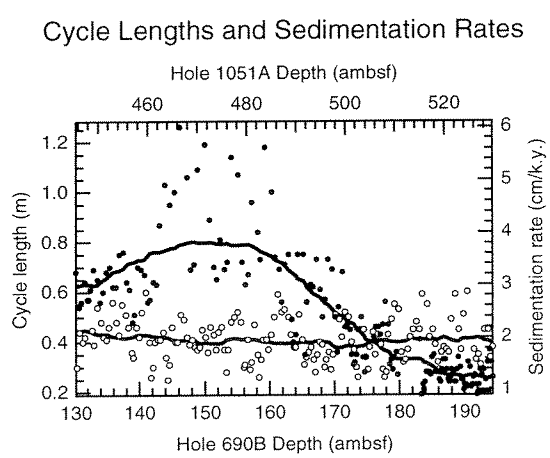

Figure 1.8: Cycle length and sedimentation rate through the sections analyzed in Holes 690B (open circles) and 1051A (filled circles). Cycle length was transformed into sedimentation rate using an assumed 21 k.y. cycle duration. Individual points represent individual cycles; lines are a 41 point running average. Note that precessional cycles are not expected to be of constant duration, so the running average is more meaningful than the individual points.

count occurs at Hole 1051A in the interval between 495 and 510 ambsf. The gradual increase in cycle wavelength that occurs in this interval leads to greater uncertainty in cycle identification (Figure 1.8). As a result, there is a large discrepancy between conservative and liberal delineation of cycles.

1.5.2 Discussion

Based on the cycle count presented here for Hole 1051A, the LPTM is 903±42 k.y. younger than the base of Chron C24r (Table 1.2). This is consistent with the estimate of 924-966 k.y. made by Norris and Röhl [95] using magnetic susceptibility and Fe intensity logs for Site 1051. It contrasts with the estimate of ~480 k.y. made by Aubry et al. [6] based on interpolation of sedimentation rates in Hole 690B. The estimate made here is less accurate than that of Norris and Röhl [95] because the LPTM occurs in a coring gap in Hole 1051A; Norris and Röhl [95] spliced logs from Holes 1051A and 1051B to cover this gap. The full duration of Chron C24r at Hole 1051A (2.856±0.441 m.y.) is not very well constrained due to uncertainty in cycle identification caused by the gradual increase in cycle length in the interval above the LPTM (Figure 1.8). Although the mean duration calculated for Chron C24r is longer than the duration estimated in the GPTS, the cycle-based estimate for the duration of Chron C24r cannot be used to evaluate the accuracy of the GPTS because of this large error on the cycle counts (Table 1.2).

The carbon isotope excursion (CIE) which marks the onset of the LPTM can be assumed to be globally synchronous and this event together with the cyclostratigraphy can therefore be used to correlate Holes 1051A and 690B (Figure 1.9). There are two reasons to make this correlation. 1) The NP9/NP10 boundary is not delineated in published data from Hole 1051A. The cycle count at Hole 690B allows a calibration for this biostratigraphic datum. 2) The error in cycle counting is much smaller in Hole 690B in the interval above the LPTM. Correlation between the two sites and creation of a spliced section allows a more accurate estimate for the duration of

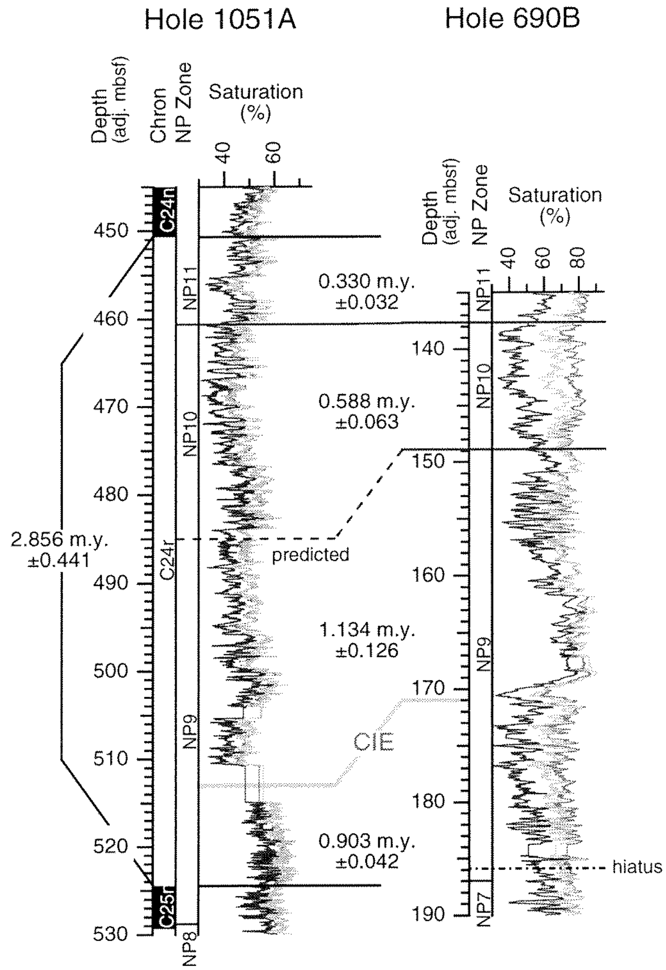

Figure 1.9: Correlation between Holes 1051A and 690B. The correlation allows a more precise calculation for the duration of Chron C24r and calculation of the duration between the NP9/NP10 boundary (which is not delineated at Site 1051) and other stratigraphic datums. Note that the position of the Zone NP9/NP10 boundary in Hole 1051A is predicted based on cycle correlation with Hole 690B.

Chron C24r. The magnetostratigraphy for Hole 690B is strongly overprinted and so the cyclostratigraphy can not be directly tied to magnetostratigraphy [1]. The quality of magnetobiostratigraphic data available for Holes 690B and 1051A is typical of Chron C24r sections. No single section can be relied on to produce a standard (chrono)stratigraphy. Instead, it will be necessary to tie numerous sections together using available magnetobiostratigraphic datums and test the resulting correlations through cycle-based estimates of temporal duration. The analysis presented here is intended to represent a preliminary step in this process which will be further advanced as more data becomes available.

In order to splice the sections a second correlation level must be used in conjunction with the CIE. Because the biostratigraphy at Hole 1051A is incomplete, the only level that can be used is the NP10/NP11 contact. This introduces a substantial amount of uncertainty because it has been inferred that biochron NP10 is not completely represented in Hole 690B [6, 7]. However, because the cycle-based duration between the LPTM and the base of Zone NP11 is consistent at both sites (Table 1.2) it is likely that the duration of any hiatuses in Hole 690B must be less than the error in the cycle counts. Eventually, the duration of these inferred hiatuses and the timescale on which diachrony of biostratigraphic datums is important can be tested using cycle-based correlation with other sections. For simplicity, the interval between the LPTM and the base of Zone NP11 is taken to be complete in Hole 690B in this discussion.

The duration of Chron C24r should be equivalent to (or slightly longer than) the summed durations in the spliced section of the intervals Base NP11-Base C24n (1051A), NP10 (690B), LPTM-Base NP10 (690B), and Base C24r-LPTM (1051A) (Table 1.2; Figure 1.9). The total duration of this spliced section is 2.955 ± 0.263 m.y., within the error for the Chron C24r cycle count at Hole 1051A. However, this duration is 5-25% longer than the duration estimated in the GPTS. This duration may be an underestimate because the duration of any hiatuses within Zone NP10 in Hole 690B are not included.

Both the cycle count in Hole 1051A and the duration in the spliced 690B-1051A section suggest that Chron C24r may be 300-400 k.y. longer than the 2.557 m.y. duration estimated in the GPTS. However, it is likely that this discrepancy is at least partially due to other factors, including: 1) The limits of Chron C24r may be incorrectly delineated at Hole 1051A. 2) Biostratigraphic datums may be diachronous between Holes 1051A and 690B, so that the record is incorrectly spliced. 3) The duration of an average precessional cycle may have been shorter than 21 k.y. at 55 Ma. It would be premature to conclude that any one of these factors is primarily responsible for the discrepancy based on the data presented here. The duration for Chron C24r estimated in the GPTS is much more robust than any estimate that could be made based on existing cyclostratigraphic data. The following testable hypotheses can be drawn from the correlation between Holes 1051A and 690B (Figure 1.9):

1. A ~500 k.y. hiatus occurs in the interval between the base of NP9 and the LPTM in Hole 690B, accounting for the difference in the number of cycles between these two datums in Holes 690B and 1051A (Table 1.2, Figure 1.9). Zone NP8 is very thin in Hole 690B, suggesting that the hiatus is longer than 500 k.y. and encompasses most of Zone NP8 and the base of Zone NP9. As a result, the age estimate for the LPTM based on the assumption of a conformable NP8/NP9 boundary and good magnetostratigraphy at Site 690B [6] is too old.

2. The duration of nannofossil Zone NP9 was greatly underestimated and the duration of NP10 was overestimated in BKSA95 (Table 1.2, Figure 1.9). Zone NP9 is ~2.4 m.y. long (rather than 1.18 m.y. and NP10 is ~0.6 m.y. long (rather than 1.39 m.y.). This difference was predictable, since the NP9/NP10 Zonal boundary was forced to be 55 Ma in order to be consistent with certain assumptions made in constructing the GPTS (see above). The error introduced into the GPTS by using the 55 Ma tiepoint can be (very roughly) estimated by examining the cyclostratigraphic calibration presented here. The $^{40}Ar/^{39}Ar$ date for the lower ash layer at Hole 550 is 54.51±0.05 Ma. Because this ash layer occurs within Zone NP10 it provides a constraint on the minimum age at the base of that zone. Using 54.6 Ma for the base of Zone NP10 and the cycle-based durations, the top of Chron C24r is ~53.7 Ma rather than 53.347 Ma as given in the GPTS. The age of the LPTM would then be between 55.3 and 55.7 Ma, depending on the total duration used for Chron C24r.

3. The NP9/NP10 boundary should be found at ∼485 mbsf in Hole 1051A (Figure 1.9). This prediction is made based on cycle counting down from the NP10/NP11 boundary but is consistent with counting up from the LPTM.

1.5.3 Future work

Using only Holes 1051A and 690B it is impossible to improve the age calibrations for the GPTS in this interval because there is no independent age for any level in either section. In order to modify the GPTS it will be necessary to directly tie a cyclostratigraphy to the $^{40}Ar/^{39}Ar$ dates using Hole 550 or another section with datable ash layers. Similarly, diachrony of biostratigraphic datums cannot be evaluated using the data presented here because the errors in the cycle count are too large and published biostratigraphies for Hole 1051A do not permit full delineation of all zones and subzones recognized by Aubry et al. [6, 7] in Hole 690B.

Although cycle counts can be very accurate, there is no means of estimating that accuracy other than making a conservative and liberal count as I have done. A more robust, astronomically based chronostratigraphy can be produced by tuning logs to exploit the full spectrum predicted by orbital theory [77, 97, 119]. Ultimately, the test of any timescale is consistency between geographically separate sections. This can only be gauged through attempted correlation between available sections, even when the points of correlation are not ideal. Using sediment color logs from core photographs will greatly advance this process by providing a means to retrofit high-resolution lithologic logs for many sections which have become crucial for paleoceanography and chronostratigraphy.

1.6 Conclusions

Color logs produced by digitizing core photographs provide an easy means of generating high-resolution geophysical logs for ODP and DSDP sites which lack such logs. This method will be useful for cyclostratigraphic calibration of many sites which were drilled before core and downhole logging was standard practice. The logs are reliable both as absolute measures of sediment color and as accurate recorders of sediment cyclicity, although the amplitude of cyclicity at the core section (1.5 m) scale is somewhat dampened.

The discrepancy between the cycle counts in the Chron C24r sections at Holes 1051A and 690B and the GPTS is fairly small, but too large to be reconciled based solely on the data from these two sections. The astronomically calibrated durations of calcareous nannofossil zones within Chron C24r presented here is substantially different from that in BKSA95 and Aubry et al. [6]. Using color logs generated from core photographs will make it significantly easier to test these calibrations in other sections and, eventually, to revise the GPTS in this interval. Because chronostratigraphy provides the sole means of assessing rates and relative timing of climate processes, it can be expected that future, astronomically-based revisions to the timescale will have repercussions in the interpretation of Earth's climate history in the late Paleocene-early Eocene.

Chapter 2

Milankovitch and transient carbon isotope events near the Paleocene/Eocene boundary*

2.1 Abstract

Carbon isotope records from the North Atlantic (ODP Site 1051) and Southern (ODP Site 690) oceans show that orbital forcing strongly influenced Earth's climate in a ~4 m.y. interval spanning the Paleocene/Eocene boundary, the warmest interval of the Cenozoic. Precession-forced oscillations of 0.1–0.2 ‰ amplitude are evident in the $\delta^{13}C$ records, but the most prominent orbital features are 0.5–1.0 ‰ transient decreases coincident with maxima in Earth's orbital eccentricity. A simple mathematical model accounts for the eccentricity response as the effect of the residence time of carbon (of order 10^5-years) on a nonlinear carbon cycle response to precession forcing. The magnitude of the transients is similar to the amplitude of eccentricity-scale $\delta^{13}C$ variations in the Neogene, suggesting a similarity in the sensitivity of the carbon cycle between the Paleogene greenhouse climate and the glaciated Neogene. The transients are similar to the larger amplitude carbon isotope excursion at the Paleocene/Eocene boundary, but the latter occurred near a 405-k.y. eccentricity minimum and thus must have had a different, unique cause.

*B.S. Cramer and J.D. Wright, manuscript submitted to *Science*, 2002.

2.2 Introduction

The Paleocene/Eocene (P/E) boundary (~55 Ma) is characterized by a transient 2–5 ‰ decrease in marine and terrestrial $\delta^{13}C$ records [67, 72, 73]. The onset of this carbon isotope excursion (CIE) occurred in <50 k.y., followed by an exponential recovery over ~150 k.y. to pre-excursion values [65, 95, 109]. It was accompanied by an equally abrupt excursion to extremely low $\delta^{18}O$ values in marine records, indicating that global temperatures exceeded those recorded at any other time during the Cenozoic and leading to the designation of the event as the Paleocene/Eocene thermal maximum [PETM; formerly latest Paleocene thermal maximum, 149]. Extensive research has detailed the evolution of this event at numerous locations [10, 20, 21, 22, 32, 65, 67, 72, 73, 95, 109, 114, 127, 132, 133] and it has been suggested that the CIE was just the largest in a series of similar "hyperthermals" [e.g., 134].

It is recognized that variations in the geometry (precession, obliquity, and eccentricity[†]) of Earth's orbit around the sun are a primary driver of climate change on timescales $<10^6$ years [e.g., 51, 80, 85, 97, 117, 151]. Precession cycles in geophysical logs have been used to constrain the timing and duration of the P/E CIE [95, 109], but the timing of the event relative to normal variations in the amplitude of climate change (e.g., eccentricity modulation of the precession amplitude) has not previously been investigated. This leaves open the question whether the PETM climate perturbation was truly anomalous or instead simply the largest in a series of events whose timing might be controlled by orbital forcing.

[†]Variations in Earth's orbit result from gravitational interactions between all of the bodies in the solar system. These result in periodic variations in the distribution of insolation on Earth's surface due to precession (wobble of Earth's axis relative to a fixed reference frame; ~19 and ~23 k.y. periods) and variations in obliquity (tilt of the axis of rotation; ~41 k.y. period). The amplitude of the insolation changes also varies depending on the eccentricity of Earth's orbit (~100 and ~400 k.y.

2.3 Methods and results

The presence of high-amplitude (~1 ‰) eccentricity-controlled cyclicity in upper Paleogene–Neogene (<30 Ma) δ^{13}C records [38, 44, 145, 148, 150] suggests a strategy for investigating the relationship between Milankovitch forcing and the P/E CIE: if similar eccentricity-scale cyclicity is identifiable in upper Paleocene–lower Eocene records, then it should be possible to determine whether the P/E CIE is in phase with that cyclicity. We generated bulk carbonate stable isotope records (Figure 2.1[‡]) at <10 k.y. resolution for a 3–4 m.y. interval spanning the P/E boundary at Ocean Drilling Program (ODP) Sites 690 (Maud Rise, Atlantic sector Southern Ocean, 65°9′S, 1°12′E) and 1051 (Blake Nose, western North Atlantic Ocean, 30°3′N, 76°21′W). The PETM interval has been thoroughly characterized at both of these sites [10, 65, 67] and our analyses are consistent with previously published data.

We produced preliminary age models based on magnetostratigraphies for the two sites [1, 96, additional paleomagnetic analyses for Site 1051 performed for this study], a nominal age of 55 Ma for the P/E CIE [after 95], and cycle counts in geophysical logs (see Chapter 1). The most obvious feature of the δ^{13}C records is the 2.5 ‰ decrease at the P/E boundary — the CIE. Several similar, albeit lower amplitude (0.5–1.0 ‰), transient decreases occur at the two ends of the interval (<53.5 and >55 Ma), and even smaller but still recognizable events occur in the

periods). The periods listed here are only the primary ones recognized in climate records; many more are necessary to accurately characterize the variations in orbital parameters.

[‡]Samples were reacted in phosphoric acid (H_3PO_4) at 90°C in a Multiprep peripheral attached to a Micromass Optima mass spectrometer at Rutgers University. The analytical precision (2 σ) of the standards analyzed (either NBS19 or an in house standard referenced to NBS19) was <0.04 ‰ (δ^{13}C) for each sample run; reproducibility of sample analyses between runs was typically within the analytical precision. Interpretation of bulk carbonate isotopic analyses can be compromised due to nannofossil assemblage changes, size fraction changes, and diagenesis. However, the presence of precession cyclicity having the appropriate amplitude relative to eccentricity cyclicity argues against any of these factors being a significant consideration (see Figures 2.3 and 2.4 and discussion in text).

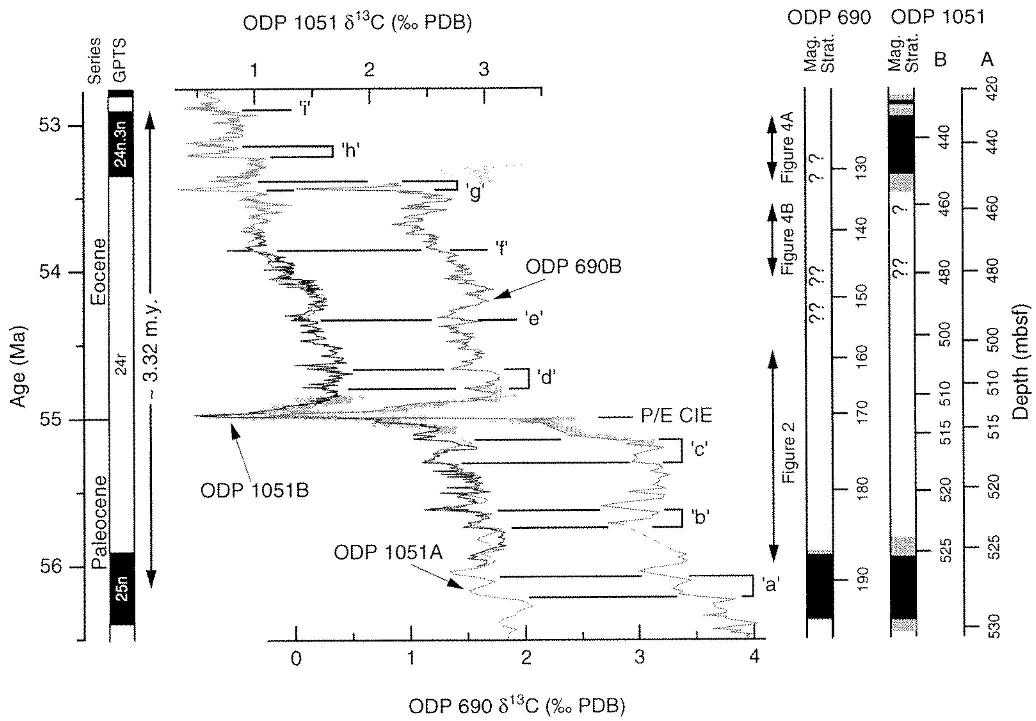

Figure 2.1: Bulk carbonate δ^{13}C records plotted relative to the geomagnetic polarity timescale of [28, 29, see text for description of age model]. Horizontal lines indicate transient δ^{13}C events used as tie-points for correlation and interpreted as resulting from eccentricity forcing; events or paired events are assigned letters sequentially from the bottom for reference in the text and other figures. Arrows to the right indicate the intervals displayed in Figures 2.2 and 2.4. The dashed interval in the lower portion of the 690 record indicates a coring gap; analyses for samples taken above an unconformity at the top of the 690 section are plotted as unconnected dots. For clarity, data from the two holes drilled at Site 1051 (Holes 1051A and 1051B) are plotted separately, although the records could easily be integrated. High-resolution bulk carbonate records through the PETM from [10] are also plotted as unconnected symbols.

interval immediately above the P/E CIE. Only minor adjustments to the age models were necessary to allow correlation of these δ^{13}C events (Figure 2.1).

There is a pattern in the distribution of the events: short intervals between events alternate with long intervals, although the CIE and the two lone, very low amplitude events in the upper part of Chron C24r distort this rhythm (Figure 2.1; secondary events could be identified near these two, but they are not obviously correlative between the two sites). The rhythmic pattern suggests a periodic process, which would indicate Milankovitch forcing. Indeed, by excluding the CIE and treating the closely spaced events as single markers (labeled 'a'–'i'in Figure 2.1), the events demarcate eight intervals with a cumulative duration of ~3.32 m.y., yielding a mean duration between events or paired events of ~0.415 m.y. The recurrence rate is therefore consistent with interpretation of these events as controlled by the ~0.406 m.y. eccentricity component, similar to cyclicity documented in upper Paleogene–Neogene δ^{13}C records [38, 44, 145, 148, 150]. Justification for this interpretation is provided in the following paragraphs.

In order to better understand the timing of the CIE relative to the smaller δ^{13}C events, we compared the occurrence of δ^{13}C transient events with cyclicity observed in sediment color logs[§]and attributed to precession forcing [31, 95, 109]. This cyclicity is best developed in the interval between the CIE and the base of Chron C24r (Figure 2.2), but the observation that ~20 precession cycles occur within each of the eight intervals noted above holds throughout the records. Assuming a mean precession cycle duration of ~21 k.y. [e.g., 11, 54], the δ^{13}C events are therefore separated by ~420 k.y., again consistent with an eccentricity response. Moreover, 4–6 cycles are identified in the short intervals between paired events, consistent with a cyclicity controlled by the ~100 k.y. eccentricity component. However, the CIE is separated by only 7–9 cycles from the next lower pair of δ^{13}C events; it is difficult to confidently identify precession-scale cyclicity in the PETM interval itself (e.g., compare [95] vs. [109]) but no more than 13 precession cycles occur in the interval between

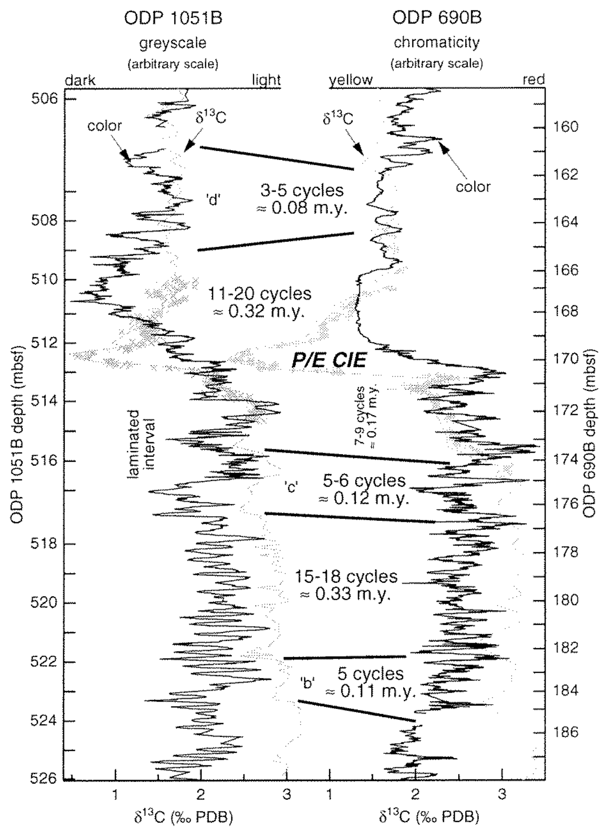

Figure 2.2: Sediment color logs and carbon isotope records from Sites 690 and 1051 for a ~1.5 m.y. interval including the CIE. Lines between the two records demarcate the δ^{13}C events; cycle counts in the logs constrain the duration between these events. The different character of the log at Site 1051 in the interval from ~514.5 to ~517 mbsf is due to a change in lithology from bioturbated sediments below to laminated/bedded sediments within this interval, which we interpret as having been deposited rapidly. The records are plotted relative to total core recovery, but depth labels have been adjusted to correspond to ODP standard mbsf. Tick marks on the depth axis are uneven at certain levels due to excess recovery or voids.

the CIE and the next higher δ^{13}C event. Since the total interval (i.e., 11–20 precession cycles) between the next lower (`'c'`) and next higher (`'d'`) events surrounding the CIE is consistent in duration with other long intervals in the records (~17 cycles), the occurrence of the CIE in this interval appears to be anomalous.

§Color logs were generated from core photographs using the Igor utility described in Appendix A. For Site 690, chromaticity values were obtained by normalizing the RGB tristimulus values to the mean of the three channels. The lighting artifact was reduced by taking the first principal component of the chromaticity values; the second principal component is dominated by the lighting effect. This technique could not be applied to the Site 1051 logs because the sediment color varies within shades of grey, so that the intensity variations induced by the ambient lighting are not analytically separable from the actual variations in sediment color. Instead, we used a greyscale log generated by taking the mean of the RGB tristimulus values. The resulting log was used in preference to the shipboard

2.4 Discussion

2.4.1 Modeling the $\delta^{13}C$ eccentricity response

Marine carbon isotope variations reflect the relative rates of erosion/dissolution versus deposition of carbonate and organic carbon: a net increase in organic carbon deposition results in increasing $\delta^{13}C$ values [44, 90, 116, 138, 145, 148]. Such variations may be expected to reflect precession forcing of productivity through processes such as alteration of nutrient distributions by insolation forcing of atmospheric and oceanic circulation. Since eccentricity only affects climate through modulation of the precession amplitude, it has been recognized that the presence of eccentricity-scale cyclicity in climate proxy records implies an asymmetric response to precession forcing [e.g., 147]. However, this alone cannot explain the character of the carbon isotope records: simple truncation of a precession signal would result in a precession amplitude during eccentricity maxima equivalent to the amplitude of the eccentricity cycle itself. In the $\delta^{13}C$ records presented here, the amplitude of precession cycles during the transient events is nearly an order of magnitude smaller than the amplitude of the eccentricity events, as it is in records from other parts of the Cenozoic [148, 150, 151].

The prominence of the eccentricity signal in $\delta^{13}C$ records results from the residence time of carbon in the ocean-atmosphere-biosphere reservoir, which is of order 10^5 years [e.g., 25, 111, 125] and effectively acts as an analog low-pass causal (i.e., phase-shifting) filter transferring spectral power from the precession band to the eccentricity band. Provided there is any nonlinearity in the carbon cycle response to precession forcing, a strong eccentricity signal in $\delta^{13}C$ records is expected due to the carbon residence time. We model the $\delta^{13}C$ records as the convolution of an asymmetric precession-like curve with an exponential decay function representing the residence time of carbon (see caption to Figure 2.3 for details). The character of the resulting

spectrophotometer logs (to which it compares well [e.g, 31]) because of the higher sampling resolution and because of evident artifacts in the spectrophotometer logs.

curve is very similar to the $\delta^{13}C$ records and we have used it loosely as a "target" for constructing a $\delta^{13}C$ -based orbital timescale (Figure 2.3). While we recognize that the precession periods used in constructing the synthetic curve are not strictly valid for the early Paleogene [11, 78], the timing of the transient spikes is almost entirely controlled by the eccentricity modulation. Since the modulatory periods can be expected to remain constant through geologic time [11, 78], the exact values used for the precession periods are essentially irrelevant so long as the interaction results in modulation at the correct eccentricity periods.

Several features of the $\delta^{13}C$ curves are explained by consideration of the residence-time effect.:

1. The rapid decreases in $\delta^{13}C$ values result from successive high-amplitude precession cycles at eccentricity maxima where the residence time of carbon prevents full recovery of $\delta^{13}C$ values between each cycle. The interval of most rapidly decreasing values should correspond with the eccentricity maximum itself.

2. The paired events result from successive short eccentricity cycles at a long (~400 k.y.) eccentricity maximum; during long eccentricity minima, the short eccentricity amplitude is not large enough to result in a rapid shift.

3. Somewhat unexpectedly, the interval of low amplitude events (0.4–1.3 m.y. from CIE, Figure 2.3) is matched by a very similar interval in the synthetic curve and results from a minimum in the long period (~2 m.y.) eccentricity modulation. We emphasize, though, that our records are not long enough to accurately evaluate the duration of this modulatory period, which is not necessarily expected to remain constant through time [78].

Our model predicts that precessional cyclicity should be present in $\delta^{13}C$ records with an amplitude an order of magnitude smaller than the magnitude of the transients. In intervals where the $\delta^{13}C$ records are sampled at sufficiently high resolution

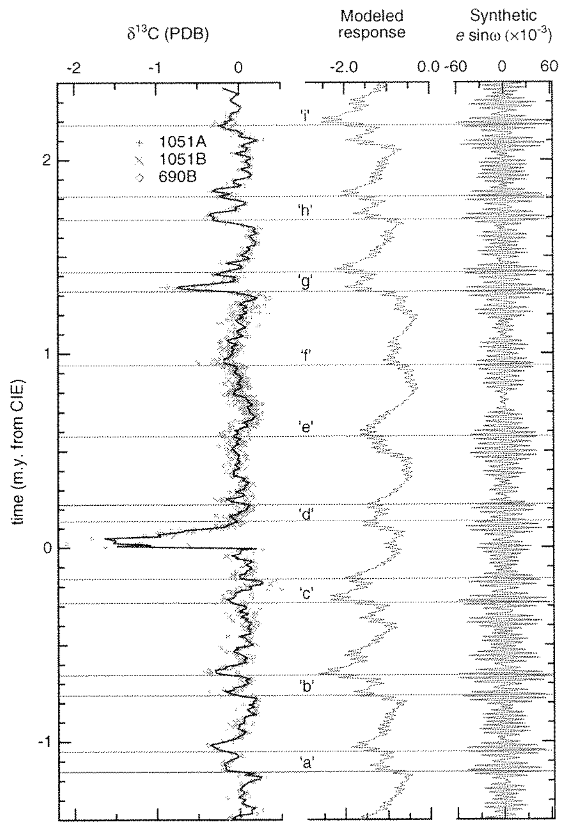

Figure 2.3: Comparison of the stacked carbon isotope record with the modeled response. Carbon isotope records from Sites 690 and 1051 were differentially stretched to match transient events with the synthetic curve (the P/E CIE was placed at 0 on the time axis as a matter of convenience) and detrended by subtracting a low-pass gaussian filter with a 0.1 response at a frequency of 2.5 cycles/m.y. Data from a 0.1 m.y. interval following the P/E CIE were removed prior to applying the low-pass filter (the high-amplitude CIE will heavily influence the filter) but were retained in the detrended records. A smooth curve was generated through the stacked records using a low-pass gaussian filter with a 0.9 response at a frequency of 12 cycles/m.y. The synthetic precession curve on the right was constructed using the equation $e\sin\omega = \sum_{i=1}^{5} A_i \cos\left(\frac{2\pi(t-t_0)}{P_i} + \phi_i\right)$, where $e\sin\omega$ is the precession parameter, values for A (amplitude), P (period), and ϕ (phase) were taken from [78], and t_0 =54.77 m.y. was used to visually match the δ^{13}C record. The synthetic curve in the middle was obtained by transforming the precession curve using the equation $\left[\exp\left(-\frac{0.1}{0.03}\right) - \exp\left(-\frac{e\sin\omega+0.1}{0.03}\right)\right]$ and convolving the result with the function $\left[\exp\left(-\frac{t}{T_{res}}\right)\right]$ where $T_{res} = 0.1$ m.y. was used to approximate the residence time of carbon [e.g., 25, 111, 125, this value can be varied by a factor of 3 without altering the character of the resulting curve].

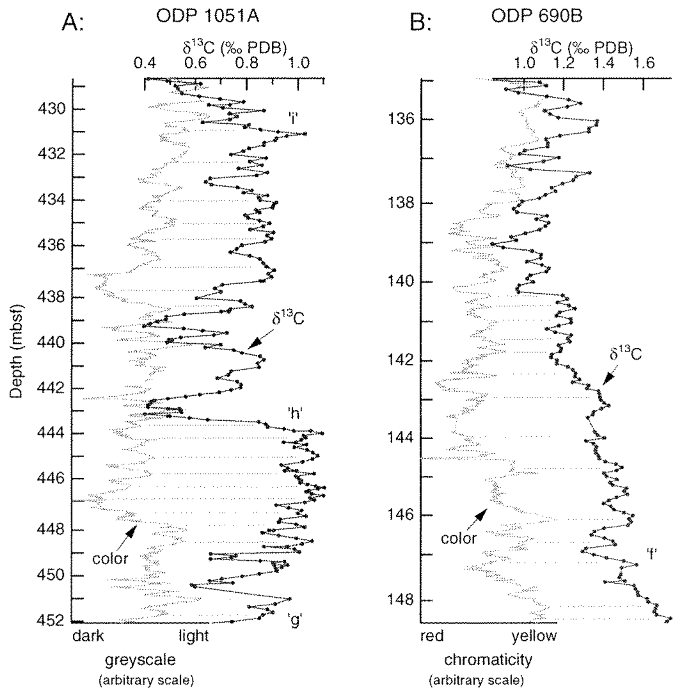

Figure 2.4: Intervals of $\delta^{13}C$ records from Sites 1051 (A) and 690 (B) sampled at $\sim$4 k.y. resolution that display precession-scale cyclicity consistent with cyclicity in sediment color logs. Horizontal lines are intended as a visual guide and do not demarcate every precessional cycle. Letters next to the $\delta^{13}C$ records refer to events labeled in Figure 2.1. The records are plotted relative to total core recovery, but depth labels have been adjusted to correspond to ODP standard mbsf. Tick marks on the depth axis are uneven at certain levels due to excess recovery or void spaces.

($\sim$4 k.y.) there is a fine-scale cyclicity in the $\delta^{13}C$ records that correlates with cyclicity in geophysical logs (Figure 2.4). The cyclicity in the geophysical logs has been attributed to precession forcing [31, 95, 109] and spectral analysis relative to our eccentricity-based timescale reaffirms this interpretation (Figure 2.5). While there is not a one-to-one correlation of cycles between the $\delta^{13}C$ records and the geophysical logs, the match is remarkably good considering that the amplitude of the $\delta^{13}C$ cycles (generally $\sim$0.1 ‰) is close to the precision of the analyses. On its own, this cyclicity could plausibly be explained as a local effect or as the result of changes in the carbonate composition due to varying abundances of different nannoplankton species. However, our model for the eccentricity-controlled transients implies a whole ocean effect: the residence time effect applies only on a global basis, so precession

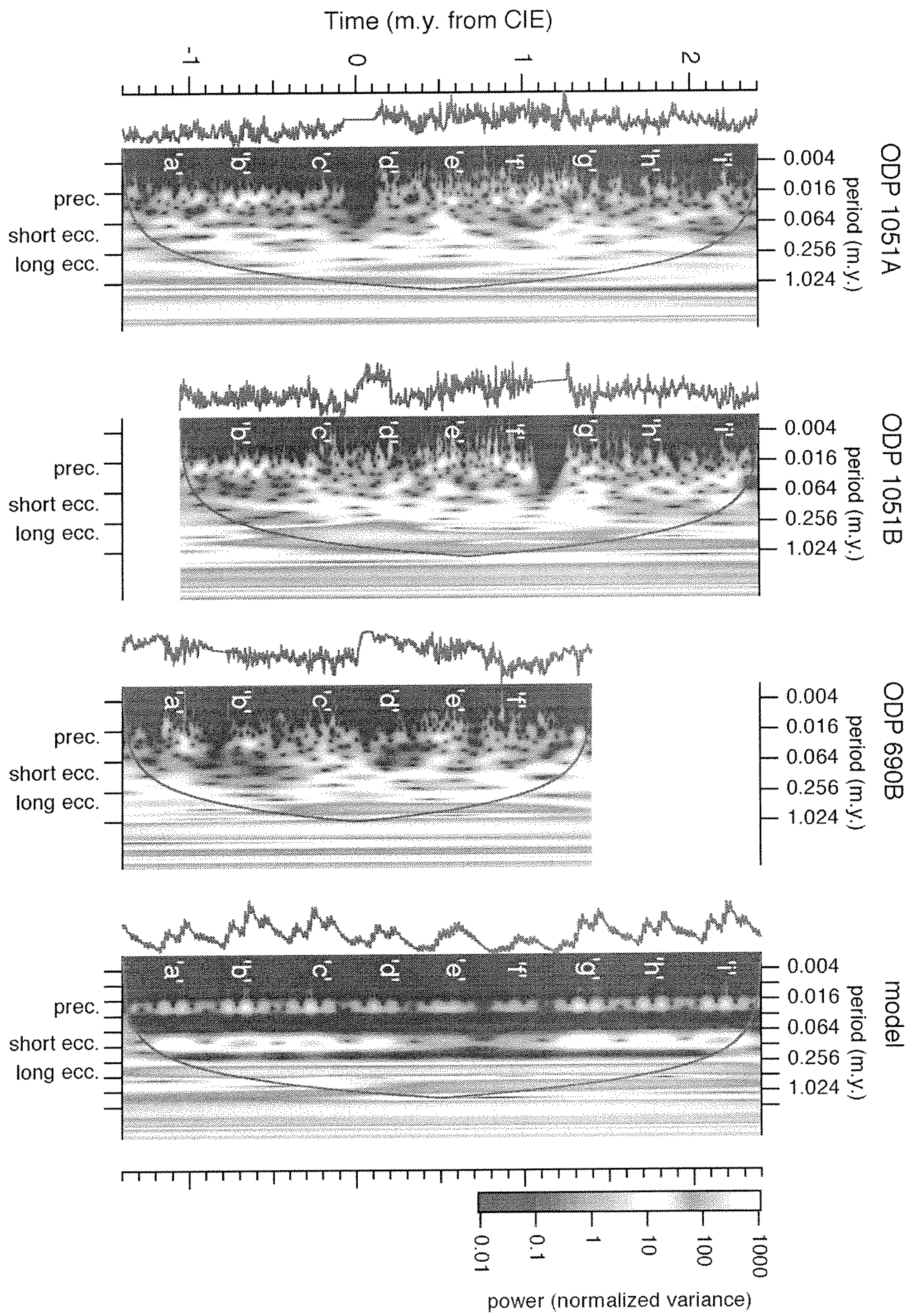

Figure 2.5: (Caption on following page.)

Figure 2.5: (Previous page.) Wavelet analysis of sediment color logs from Sites 690 and 1051 relative to the $\delta^{13}C$ -based eccentricity timescale. Logs were interpolated to 1 k.y. sampling interval and standardized to unit variance before analyzing using methods described in [136]. A Morlet wavelet was used with $\omega_o = 6$ and the series were zero-padded to extend the series length to the next higher power of two. The red line indicates the "cone of influence"; regions to the right of the line are subject to end effects — mainly damping of power due to the zero-padding. For comparison, equivalent analysis was performed on the modeled $\delta^{13}C$ response.
Power in the precession band at Sites 690 and 1051 is significant at the 1% level (99% confidence) while power in the short eccentricity band is significant only at the 35% level (65% confidence) when tested against a red noise model (lag 1 autoregressive process). No other bands of power are significant in the <1 m.y. period range. Note the distinct modulation of the precession amplitude by both the ~0.1 and ~0.4 m.y. eccentricity components, confirming that the $\delta^{13}C$ events occur at maxima in the precession amplitude.

cyclicity must be present in whole ocean $\delta^{13}C$ values in order to obtain the observed eccentricity signal.

2.4.2 General implications for interpreting $\delta^{13}C$ records

The relatively long residence time of carbon necessarily implies a decoupling of $\delta^{13}C$ records from the actual evolution of the carbon cycle on Milankovitch timescales. The smoothing effect of the residence time transfers spectral power from higher-frequency $\delta^{13}C$ oscillations (e.g., precession) into the eccentricity band, but this effect does not act on actual variations in carbon fluxes. For instance, the eccentricity response observed in the carbon isotope records presented here does not necessarily imply an eccentricity-scale cyclicity in Earth's climate. The eccentricity response should instead be taken as an indication of robust precessional forcing of the carbon cycle during the late Paleocene-early Eocene. Moreover, the similar amplitude of the eccentricity-scale variations in the $\delta^{13}C$ records presented here and in records from the Neogene [e.g. 38, 44, 150, 151] implies that precession-scale carbon cycle changes during the warm climate of the early Paleogene and the glacial climate of the Neogene were of a similar magnitude. It should be emphasized that interpretation of the amplitude of precession-scale features in $\delta^{13}C$ records as a reflection of variability in the carbon cycle must be undertaken with care: the smoothing effect of the residence time diminishes the amplitude of precession-scale changes apparent in $\delta^{13}C$ records relative to actual variations in relative fluxes of carbonate and organic carbon. The very similar character of the $\delta^{13}C$ records and the synthetic curve presented here suggests that much of the variance in the $\delta^{13}C$ records can be explained by this model. If the system really is so simple, there may be potential to invert the model and extract estimates of parameters such as the carbon residence time and carbonate/organic carbon fluxes. The expectation of a strong eccentricity signal also makes $\delta^{13}C$ records extremely attractive for the construction of astronomical timescales.

2.4.3 Implications for the cause of the PETM

Having confirmed the influence of Earth's orbital eccentricity on upper Paleocene–lower Eocene $\delta^{13}C$ records, we note that the P/E CIE occurs in between two long eccentricity maxima (Figure 2.3). This temporal calibration relative to eccentricity is very robust. It is not possible to shift the PETM so that it occurs coincident with a long eccentricity maximum because, as noted above, the integration of precessional cyclicity in the geophysical logs with the carbon isotope records constrains the duration between the preceding ('c') and following ('d') eccentricity transients to 400 k.y. Furthermore, we cannot have erred in identifying these two long eccentricity maxima because a duration of 400 k.y. to the next lower ('b') and higher ('e') eccentricity maxima is also consistent with the precession cyclicity. The data presented here conclusively demonstrate that the P/E CIE occurred near a long eccentricity minimum, in an interval which should be characterized by only gradual changes in $\delta^{13}C$ values.

There is good evidence that gradual tectonic changes can result in rapid climate change as the climate system is forced across some critical physical threshold, but that the timing of the final crossing of that threshold occurs as a result of Milankovitch forcing: high amplitude climate variations resulting from modulation of precession and obliquity cyclicity have been implicated in the intensification of glaciations during the Neogene [80, 85, 147, 151]. In the first description of the PETM, Kennett and Stott [67] noted that the event occurred superposed on the long-term late Paleocene-early Eocene warming trend. They hypothesized that the event represented a rapid transition between climate states due to the crossing of some critical climate threshold that triggered an ocean circulation change, shifting deepwater formation from high to low latitudes. This basic hypothesis has subsequently been elaborated to explain the CIE through release of ^{12}C-enriched methane as the switch to warmer low-latitude-sourced deep/intermediate waters resulted in the melting of methane hydrates [10, 21, 35, 36, 147].

However, our data indicate that a cyclicity-triggered threshold event did not result in the PETM. On the one hand, we have demonstrated that a series of high amplitude transient $\delta^{13}C$ events did result from modulation of precession forcing, with similarly rapid onset and exponential recovery as recorded at the P/E CIE. On the other hand, we have also demonstrated that the timing of the P/E CIE is inconsistent with that event being an amplification of the normal Milankovitch response. The location of the P/E CIE relative to smaller, eccentricity-controlled excursions is more consistent with an anomalous triggering event, such as slope failure [64] or a comet impact [68].

2.5 Conclusions

Orbital forcing of insolation exerted a dominant control on variability in upper Paleocene–lower Eocene $\delta^{13}C$ records on 10^4–10^6 year timescales. This conclusion should not come as a surprise, since Milankovitch forcing has been recognized in climate proxy records throughout the geologic record [e.g., 51, 54, 56, 97]. However, the amplitude of the orbital imprint on the early Paleogene greenhouse climate has not been fully appreciated: orbitally-forced variations in the Paleogene carbon cycle were similar in amplitude to variations in the Neogene. Although we have suggested that transient climate events do not necessarily accompany the transients in the $\delta^{13}C$ record, benthic foraminiferal assemblage changes have been used to infer a series of transient climate events in the late Paleocene–early Eocene [134] and $\delta^{13}C$ events are generally linked to climate change in the Neogene [38, 44, 145, 148, 150, 151] and changes in atmospheric pCO_2 in the Pleistocene [e.g., 117]. Further study is needed to fully constrain the climate response to insolation changes during the early Paleogene, but data presented here clearly point to the potential for understanding the sensitivity of the greenhouse climate in the context of the Milankovitch pacemaker.

Chapter 3

The age of the Paleocene/Eocene boundary: An orbitally tuned, integrated carbon isotope, calcareous nannofossil, magnetic polarity, and radioisotope chronology*

3.1 Abstract

We present a revised correlation of stratigraphic events in the latest Paleocene–earliest Eocene among Ocean Drilling Program Sites 1051 and 690 and Deep Sea Drilling Project Sites 550 and 577. The new correlation is cyclostratigraphically constrained based on recognition of (~405 k.y.) eccentricity cycles in carbon isotope records and confirmed by precession cyclicity in geophysical logs. Recognition of eccentricity cycles in the $\delta^{13}C$ records allows precise correlation, independent of magneto- and biostratigraphic data, at the <100-k.y. scale among the four sites. Astronomically calibrated durations for magnetic polarity chrons C25n, C24r and C24n.3n are 0.38 ± 0.06, 2.30 ± 0.05, and 0.68 ± 0.09 m.y., respectively. Calcareous nannoplankton biostratigraphic datums are found to be synchronous within <0.1 m.y. among Sites 1051, 550, and 577; datums at Site 690 are delayed by as much as 0.6 m.y.

We tie this cyclostratigraphic framework to $^{40}Ar/^{39}Ar$ ages for two ash layers from the Fur formation in Denmark that have been correlated with ash

*B.S. Cramer, M.-P. Aubry, C.C. Swisher, III, D.V. Kent, J.D. Wright, manuscript in preparation for submission to *Earth and Planetary Science Letters*, 2002.

layers identified at DSDP Site 550. The resulting ages of the C24n/C24r and C24r/C25n boundaries are 53.49 $\pm$ 0.07 and 55.86 $\pm$ 0.07 Ma, respectively. The age of the carbon isotope excursion that has been adopted as the defining criterion for placement of the Paleocene/Eocene boundary is found to be 54.97 $\pm$ 0.07 Ma.

3.2 Introduction

Correlation and temporal calibration of events surrounding the Paleocene/Eocene (P/E) boundary has proven to be a particularly thorny problem in chronostratigraphy. The placement of the boundary itself within a chronostratigraphic scheme has been problematic, as evidenced by the identification only of a "Paleocene/Eocene boundary interval" in the most recent Cenozoic integrated magnetobiochronology [13]. This has been resolved in a recent vote of the International Subcommision on Paleogene Stratigraphy establishing the carbon isotope excursion (CIE) in magnetic polarity Chron C24r as the primary criterion for global correlation of the P/E boundary [ISPS Newsletter no 9, p. 13] and a more recent proposal to establish a Global Standard Stratotype-section and Point for the P/E boundary at this level at the Dababyia section in Egypt [5].

However, the numerical chronology of events in the Paleocene–Eocene boundary interval has remained relatively unconstrained. The fundamental problem encountered in attempting to establish a numerical chronology for this interval is its placement within the ~2.5-m.y.-long reversed polarity interval of magnetic polarity Chron C24. As a result, correlation among sites has been dependent on the identification of biostratigraphic events and the assumption that such events are more or less synchronous at all sites. Using such correlations, Berggren and Aubry [12] and Aubry et al. [6] established a provisional numerical chronology for the P/E boundary interval using a composite section of ODP Site 690 for the older portion and

DSDP Site 550 for the younger portion of the chron. Based on this composite section they determined a relative position of the CIE 0.15 up in Chron C24r, with an age of 55.52 Ma relative to the timescales of Cande and Kent [28, 29] and Berggren et al. [13].

Cyclostratigraphy provides an alternate method for time-scale calibration not reliant on interpolation of seafloor spreading rates and sedimentation rates or on assumptions of synchrony of biostratigraphic datums [e.g., 55, 56, 118, 122]. Norris and Röhl [95] presented the first attempt at a cyclostratigraphic calibration of the age of the CIE based on counting cycles up from the base of Chron C24r at ODP Site 1051A and assuming correlation with precessional cycles. They concluded that the CIE occurred 924–966 k.y. following the C24r/C25n polarity reversal, which would place the CIE 0.37 up in Chron C24r with an age of ~54.96 Ma relative to the Cande and Kent [28, 29] GPTS.

In Chapter 1 I investigated using the same methodology of cycle counting to refine the calibration of biostratigraphic datums within Chron C24r and produced a biocyclostratigraphic correlation between Sites 1051 and 690. However, Chapter 1 demonstrated that the error inherent in precessional cycle recognition is too large to allow any real test either of the Cande and Kent [28, 29] calibration or of the assumption of minimal biostratigraphic diachrony.

We use a new strategy to provide a firm astronomical timescale of the C24n.3n–C25n interval as well as high-resolution (<100 k.y.) correlation among geographically distant sites. We use detailed carbon isotope records to identify the ~0.4-m.y.-period component of eccentricity variations. Use of this long eccentricity component to generate robust astronomical timescales has been proven in the late Neogene [56] and Triassic [97] and theoretically justified by Laskar [78] as the most reliable method of constructing cyclostratigraphies for time periods >30 Ma. A robust eccentricity signal has been documented in late Paleogene–Neogene carbon isotope records [38, 44, 145, 148, 150] and interpretation of an eccentricity forcing for the carbon isotope cyclicity

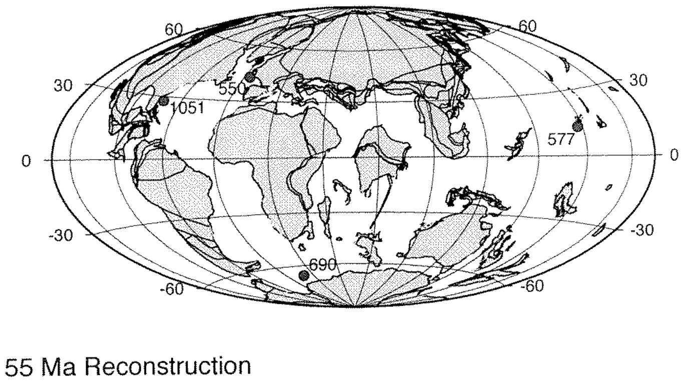

Figure 3.1: Paleogeographic reconstruction for the early Paleogene showing the location of the four sites used in this study. Reconstruction made using the web-based software available at <http://www.odsn.de /odsn/services/paleomap>

presented here is well-founded (see Chapter 2). The eccentricity-forced cyclicity in the $\delta^{13}C$ records is consistent among sites from the North Atlantic, Southern, and Pacific Oceans, providing a robust means of high-resolution correlation to complement other correlation tools.

The resulting relative chronology can be tied directly to a radioisotope geochronology due to the presence of ashes in the lowermost Eocene section at Site 550. These ashes are related to volcanism associated with the opening of the northern North Atlantic and can be correlated with the -17 and $+19$ ashes in the Fur Formation of Northern Denmark where they have been dated using the $^{40}Ar/^{39}Ar$ geochronometer.

3.3 Methods and results

3.3.1 Material

We analyzed material from four sites: Deep Sea Drilling Project (DSDP) Sites 550 and 577 and Ocean Drilling Program (ODP) Sites 690 and 1051. The sites were chosen based on two primary considerations:

1. These sites provide the global geographic coverage needed to demonstrate the correlation potential of eccentricity cycle recognition in $\delta^{13}C$ records (Figure 3.1). Of the four sites, two are in the North Atlantic Ocean (DSDP Site 550 and

ODP Site 1051), one is in the Southern Ocean (ODP Site 690), and one is in the Pacific Ocean (DSDP Site 577).

2. These sites have provided the basis for previous temporal calibrations for the early Paleogene. Sites 690 and 550 were used by Berggren and Aubry [12] and Aubry et al. [6] to establish a provisional timescale for the Paleocene–Eocene boundary interval. The magnetostratigraphy for this interval is fairly clean at Sites 550 and 577 and, as a consequence, these sites were used for many of the calibrations in Berggren et al. [13]; the age for the -17 and +19 ash layers correlated to Site 550 are integral to the GPTS of Cande and Kent [28, 29]. Site 1051 was used for the only proposed cyclostratigraphic calibration of the P/E boundary carbon isotope excursion [95] and preliminary magnetostratigraphic studies for this site were encouraging [96].

3.3.2 Carbon isotopes

We sampled for bulk carbonate δ^{13}C analysis from Holes 690B, 1051A, 1051B, 550, and 577 at an interval sufficient to provide <20 k.y. temporal resolution throughout and ~4 k.y. resolution for large portions. Relatively large (~1 cc) samples were taken so that subsamples could be analyzed from the interior of the core. Isotope analysis was performed at Rutgers University, NJ. Bulk sediment subsamples (1–10 mg) were reacted in phosphoric acid (H_3PO_4) at 90 °C in a Multiprep peripheral attached to a Micromass Optima mass spectrometer. The analytical precision (2 σ) of the standards analyzed (either NBS19 or an in house standard referenced to NBS19) was <0.04 ‰ (δ^{13}C) for each sample run; reproducibility of sample analyses between runs was typically within the analytical precision.

Each of the four δ^{13}C records contain several distinctive transient excursions of amplitude 0.5–1.0 ‰ in addition to the larger amplitude P/E CIE (Figure 3.2). In Chapter 2, I modeled the carbon isotope record as the convolution of an exponential

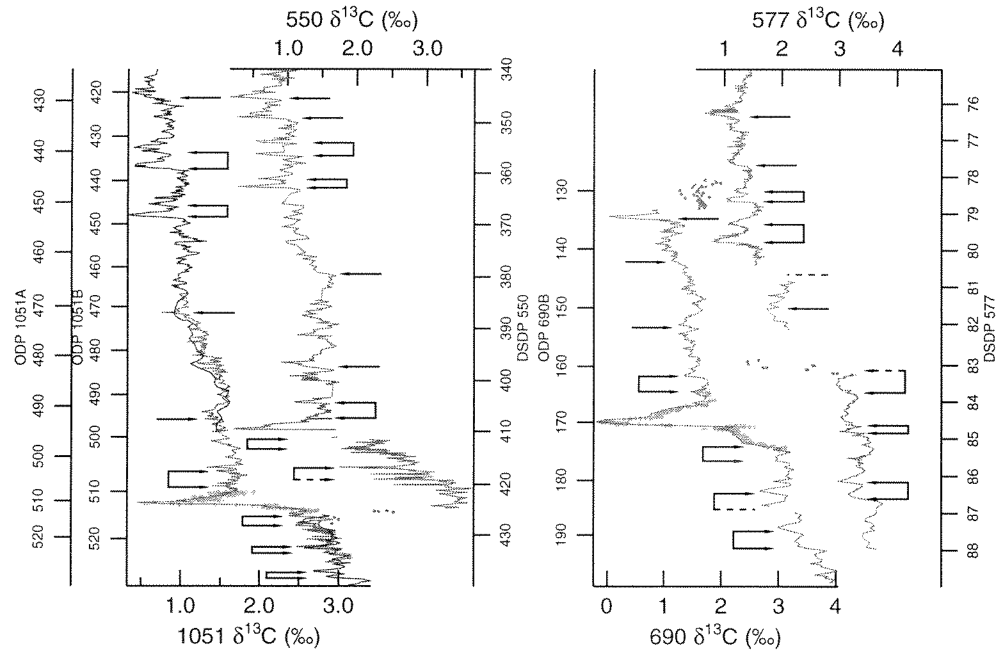

Figure 3.2: Carbon isotope records for Sites 1051, 690, 550, and 577. Arrows indicate transient δ^{13}C events interpreted as eccentricity maxima, connected arrows are paired short eccentricity maxima occurring at a long eccentricity maximum (see Chapter 2).

function (representing the residence time of carbon in the ocean-atmosphere-biosphere reservoir) with an asymmetric precession response (generated using the five main precession periods from Laskar [78]) and demonstrated that these carbon isotope transients occur coincident with eccentricity maxima, with the exception of the P/E CIE which must have had a different cause (Figure 3.3). The transient events reflect forcing by the ~0.1 m.y. short eccentricity component, but the amplitude of these transient excursions is modulated by the ~0.4 m.y. long eccentricity component: prominent transients occur near long eccentricity maxima while at long eccentricity minima the amplitude is too small to be obvious in the δ^{13}C records. Modulation by longer period eccentricity cycles is also evident: the low amplitude of the several events in the middle portion of the records results from a minimum in the ~2.4-m.y. cycle.

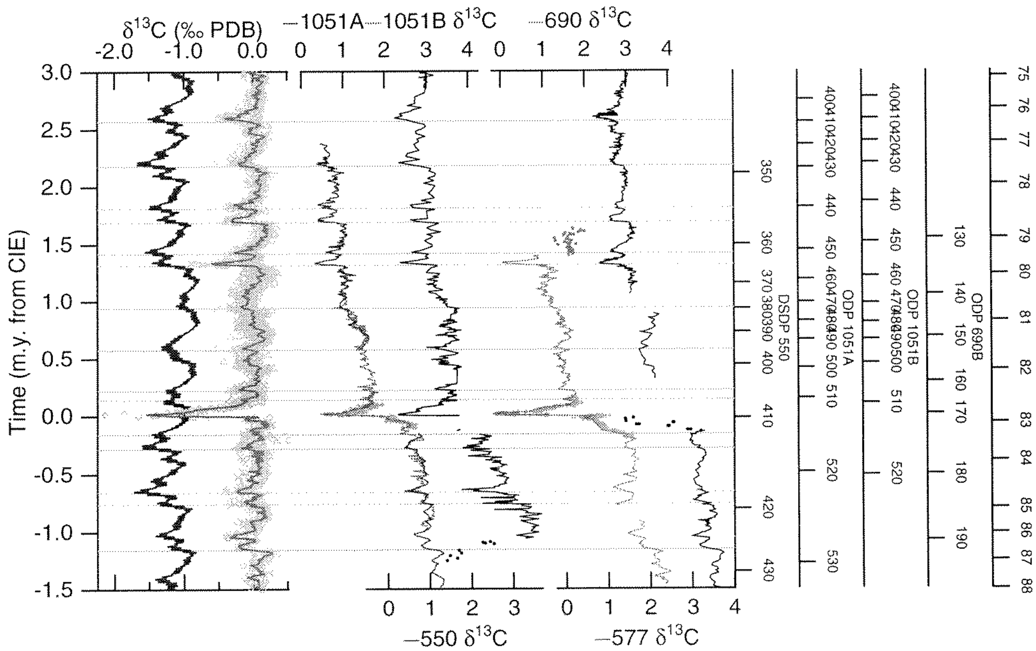

Figure 3.3: Carbon isotope records for Sites 1051, 690, 550, and 577 plotted against the relative astronomical timescale from Chapter 2. Horizontal lines mark eccentricity maxima and are equivalent to the arrows in Figure 3.2. To the left, the modeled response from Chapter 2 is plotted along with the detrended and stacked $\delta^{13}C$ records. The relative timescale was generated by matching the $\delta^{13}C$ events with events in the modeled response.

3.3.3 Geophysical logs

Sediment color logs were generated for all sites from core photographs using a modification of the method described in Chapter 1 and Appendix A. In order to further reduce the effects of lighting variations in the photographs, tristimulus values (red, green, and blue) were converted to chromaticity values by normalizing to a grayscale value for Sites 550, 577, and 690. The three chromaticity channels were then reduced to a single log by taking the first principal component. This approach was not useful for Site 1051 because the sediment color varies primarily in shades of grey, hence the lighting imparts variations that are not analytically separable from sediment color variations. Instead, the mean of the three tristimulus channels was used. By comparison with shipboard spectrophotometer measurements [100], we were able to confirm that the artifact introduced by the lighting is minimal (see Chapter 1). The sediment color logs were supplemented with magnetic susceptibility logs for Sites 1051 [100], 690, and 550. Magnetic susceptibility logs were generated for Sites 690 and 550 at the ODP core repository at Lamont-Doherty Earth Observatory using a Bartington MS/2 meter with a MS2F probe capable of obtaining independent measurements at 2 cm intervals.

The geophysical logs for sites 690 and 1051 show a robust cyclicity that we attribute dominantly to precession [following 31, 95, 109], as confirmed in Chapter 2. A less robust obliquity response dominates the logs from site 550. The sedimentary response at site 550 involves a switch from carbonate to siliceous deposition, which imparts an extremely non-linear response and results in a highly distorted cyclicity that imperfectly reflects the underlying obliquity signal. Sediment color logs from Site 577 are unreliable: although there is a clear cyclicity consistent with precession forcing in some intervals, in other intervals the signal is overwhelmed by the lighting artifact and poor core preservation is a problem throughout.

3.3.4 Magnetostratigraphy

Additional samples were taken to constrain the magnetostratigraphy at Site 1051. Samples were cut to fit in standard ODP cubes (5 cc) by staff at the ODP core repository in Bremen. Natural remanent magnetism (NRM) was measured on a 2G DC SQUID 3-axis cryogenic magnetometer at Lamont-Doherty Earth Observatory. Step demagnetization of NRM at 5 mT increments to 45 mT was performed using a large-volume alternating field (AF) demagnetization coil. Some samples were further demagnetized using a single-specimen AF demagnetization coil. The most stable paleomagnetic direction was calculated from linear demagnetization trends using the method of least-squares analysis [70].

3.3.5 Error analysis

The error in our temporal calibrations comes from four different sources:

1. *Sampling interval.* The distance between (reliable) samples analyzed results in a significant error in location of magneto- and biostratigraphic zonal boundaries.

2. *Astronomical tuning.* This encompasses both the error in the tuning target used and the error in matching the δ^{13}C records to this target. The error in the tuning target is trivial ($\ll$0.02 m.y.). We use the tuning only to establish a relative timescale based on known eccentricity periods, which should be correct within $\sim$1 % [11], or $\ll$0.01 m.y.; the error in the phase is substantially greater for the early Paleogene and prohibits using the astronomical cycles to obtain an accurate numerical age. The error in matching the δ^{13}C records to the target results primarily from our use of linear interpolation between δ^{13}C events. We suspect that actual sedimentation rates vary in response to orbital forcing of climate and should therefore be cyclic. In this case, the linear interpolation used will be close to the mean sedimentation rate over the period of the dominant cycle, and the age model at any point should not be in error by more than some fraction of that period. If sedimentation rates vary with eccentricity, then the pertinent cycle would be that of short eccentricity ($\sim$0.1 m.y.). We therefore adopt what we consider a conservative error estimate of $\pm$0.03 m.y., or $\sim \frac{2}{3}$ of a short eccentricity period (if eccentricity is not reflected in sedimentation rate variations, the pertinent cycle would be that of obliquity ($\sim$0.04 m.y.) or precession ($\sim$0.02 m.y.) and the error would therefore be smaller).

3. *$^{40}Ar/^{39}Ar$ analysis.* Analytical error in the ^{40}Ar/^{39}Ar age determination for the -17 ash.

4. *$^{40}Ar/^{39}Ar$ calibration.* The "true" error in the ^{40}Ar/^{39}Ar age determination is unknown and results from the calibration of the decay rate.

Calibrated ages for a given event are not necessarily equivalent among the four sites. In part, the discrepancy results from the errors outlined above. When the difference between sites is larger than expected, we suspect that the data are somehow compromised (e.g., overprinting of the magnetic polarity) or that it is due to diachrony of biostratigraphic datums. For calibrated ages, the combined sampling interval for all sites is used.

We do not attempt to correct for the error in the $^{40}Ar/^{39}Ar$ calibration, noting only that all of our calibrated ages will shift uniformly with a revised determination of the decay rate. The analytical error in the $^{40}Ar/^{39}Ar$ age is propagated through all of our age calibrations, but not through the calibrated durations of magnetic polarity and calcareous nannoplankton zones. Errors in the astronomical tuning and due to the sampling interval are propagated through all calibrated ages and durations. We assume that the $^{40}Ar/^{39}Ar$ and tuning errors can be approximated as normally distributed, but the error due to the sampling interval is distinctly non-normal: the probability of the stratigraphic event occurring is constant for every level between the sampled levels. If the sampling interval is larger than the other errors it will dominate the total error such that other sources of error can be ignored. If it is smaller than the other errors, its contribution to the total error can be approximated by adding the equivalent variance for a constant distribution. Errors in calibrated durations and ages are therefore calculated as:

$$\varepsilon_{age} = \max \left\{ \begin{array}{l} \sqrt{\varepsilon_{Ar}^2 + \varepsilon_{tuning(-17ash)}^2 + \varepsilon_{tuning(datum)}^2 + \frac{\varepsilon_{sampling}^2}{3}} \\ \varepsilon_{sampling} \end{array} \right\}$$

$$\varepsilon_{duration} = \max \left\{ \begin{array}{l} \sqrt{\varepsilon_{tuning(datum1)}^2 + \varepsilon_{tuning(datum2)}^2 + \frac{\varepsilon_{sampling}^2}{3}} \\ \varepsilon_{sampling} \end{array} \right\}$$

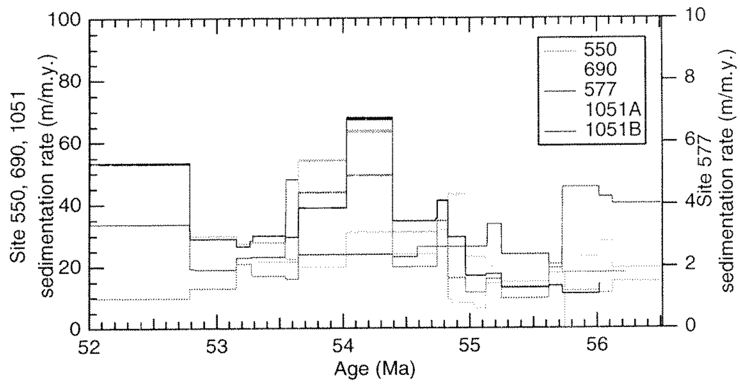

Figure 3.4: Sedimentation rates implied by astronomical age calibration.

3.4 Construction of the astronomical timescale

3.4.1 The framework

The presence of $\delta^{13}C$ events is determined by long eccentricity, but their timing is controlled by short eccentricity. Therefore, it cannot be assumed that they occur at exactly 404 k.y. intervals, the period of the long eccentricity cycle (e.g., short eccentricity cycles are of variable duration and, in any case, the long eccentricity period is not an even multiple of short eccentricity periods). Instead, we constructed age models for each site by matching the $\delta^{13}C$ events to events in the modeled response curve of Chapter 2 and using a linear interpolation to calculate sedimentation rates between events (Figure 3.4). A more pleasing smooth sedimentation rate model could have been obtained using a spline interpolation method, but this would probably not be more accurate. Actual sedimentation rates are likely to vary cyclically in response to Milankovitch forcing and an accurate reconstruction of this cyclicity would require additional control points.

Nine full long eccentricity cycles occur in the $\delta^{13}C$ record from Site 1051. We adopt a nomenclature to refer to individual eccentricity cycles, defining them as the interval between successive eccentricity maxima and numbering them sequentially from the base of magnetic polarity zones (Figure 3.5, Table 3.1). This nomenclature

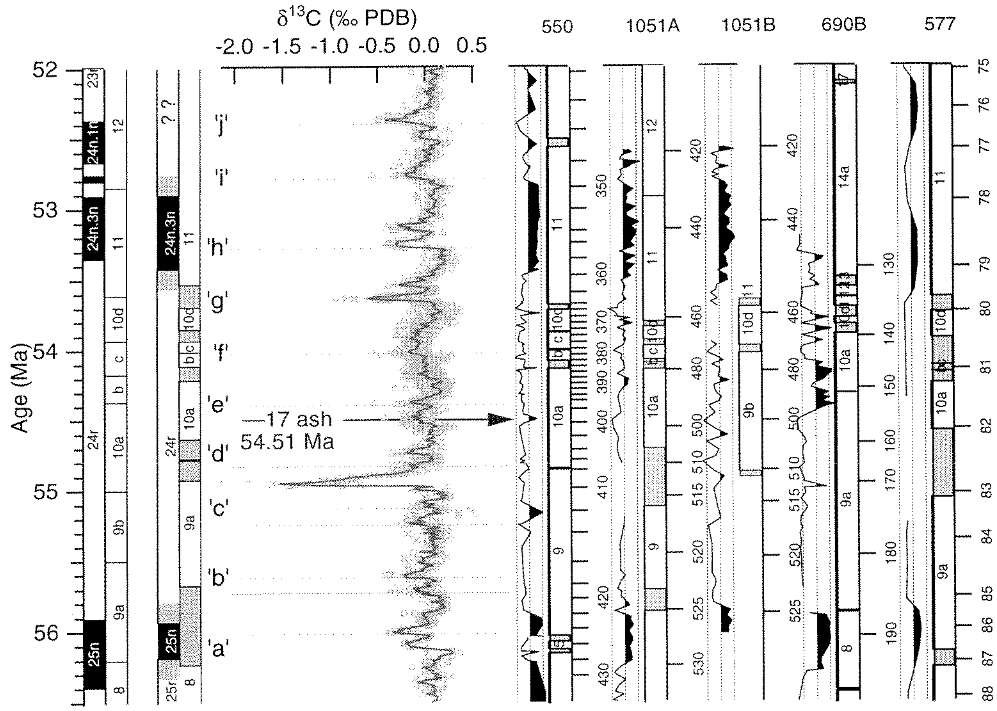

Figure 3.5: Stacked carbon isotope record, paleomagnetic inclinations, and nannofossil biostratigraphic zonations for Sites 1051, 690, 550 and 577 plotted relative to the astronomically calibrated timescale. To the left is a proposed revised calibration of ages for magnetic polarity reversals and nannofossil zonal boundaries with the timescale of Berggren et al. [13] for reference.

provides a means of identifying individual eccentricity cycles independent of any numerical chronology. We have adjusted the relative astronomically-tuned timescale to the age of 54.51 Ma at 399.74 mbsf in Hole 550, the level of the −17 ash (pers. comm. R.W.OB. Knox). This results in an astronomically calibrated age for the level of the +19 ash (392.98 mbsf) of 54.3 Ma, consistent with the $^{40}Ar/^{39}Ar$ age of 54 ± 0.53 Ma (Table 3.2).

It is possible to count the cycles in geophysical logs in intervals between carbon isotope transients; the number of cycles is consistent with the eccentricity-based tuning and confirms that no significant hiatuses exist between eccentricity-controlled

Eccentricity maximum	Age (Ma)	Depths of $\delta^{13}C$ events				
		1051A	1051B	690B	550	577
'j'	52.396	409.30	410.89	—	345.58	76.38
'i'	52.786	429.44	431.28	—	349.17	77.69
	53.156	440.26	441.74	—	353.97	78.40
'h'	53.276	443.55	444.93	—	356.71	78.68
	53.546	450.78	452.89	132.74	361.29	79.30
'g'	53.646	453.02	455.84	134.90	362.88	79.79
'f'	54.026	472.45	471.52	142.26	379.56	—
'e'	54.391	495.24	495.85	153.44	397.39	81.59
'd'	54.743	507.08	507.66	161.72	404.60	—
	54.828	510.57	509.00	164.42	407.54	—
'c'	55.126	515.50	515.64	174.26	411.64	—
	55.248	517.27	516.99	176.72	413.46	83.75
'b'	55.621	522.30	521.89	182.32	417.07	84.65
	55.726	523.70	523.33	—	419.24	84.85
	56.016	526.96	—	189.33	—	86.17
'a'	56.121	528.16	—	192.33	—	86.62

Table 3.1: Calibrated ages for short eccentricity maxima recognized in carbon isotope records and depths for Holes 1051A, 1051B, 690B, 550, and 577. Ages have an assumed error of ±0.08 m.y. due to the analytic error in the $^{40}/^{39}$Ar age (±0.05 m.y.) and the estimated error in the actual interval between eccentricity maxima (±0.03 m.y.)

Datum	Hole	samples	age range
+19 ash	550*	32-6, 98 to 32-6, 99	54.30–54.30
−17 ash	550*	33-5, 4 to 33-5, 6	54.51–54.51
P/E CIE	1051A		
	1051B	60-2, 50 to 60-2, 52	54.97–54.97
	550*		
	690B		
	577*		

Table 3.2: Sample identifications and calibrated ages of miscellaneous stratigraphic marker events for individual holes. The range represents the uppermost and lowermost samples delineating the events. Sample identifications are given in the form 'core-section, cm'. Note that the age of the −17 ash is the registration point for other calibrations and is defined by the $^{40}Ar/^{39}Ar$ age.

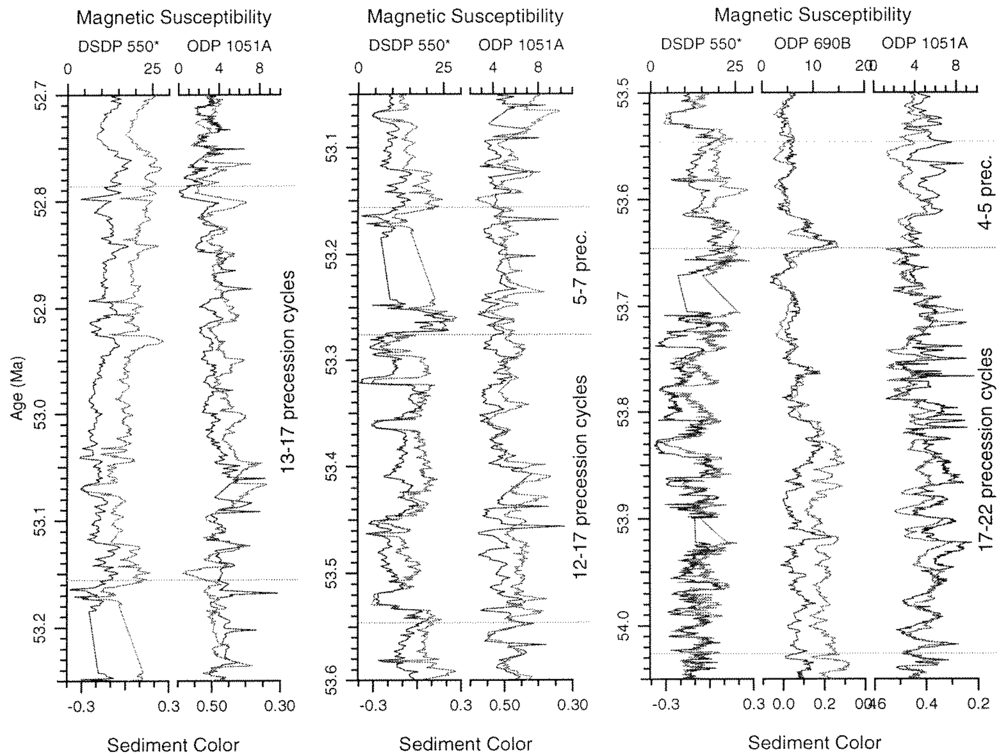

Figure 3.6: Geophysical logs for Sites 550, 690, and 1051 showing the consistency of cycle counts at Sites 690 and 1051 with the durations between eccentricity maxima determined from δ^{13}C records.

δ^{13}C transients at any site (Figure 3.6). If a suitable target curve was available it would likely be possible to refine the eccentricity-based tuning by further tuning to the precession cyclicity. Without such a target we note that the uncertainty in recognition of individual precession cycles is too large to be useful for refining the timescale. We have only attempted to do so at the P/E CIE, which occurs 7–9 cycles above eccentricity maximum 'd' at Site 690 (Figure 3.6). We have therefore imposed an age for the CIE ~0.15 m.y. younger than eccentricity maximum 'd' at all four sites (Table 3.2).

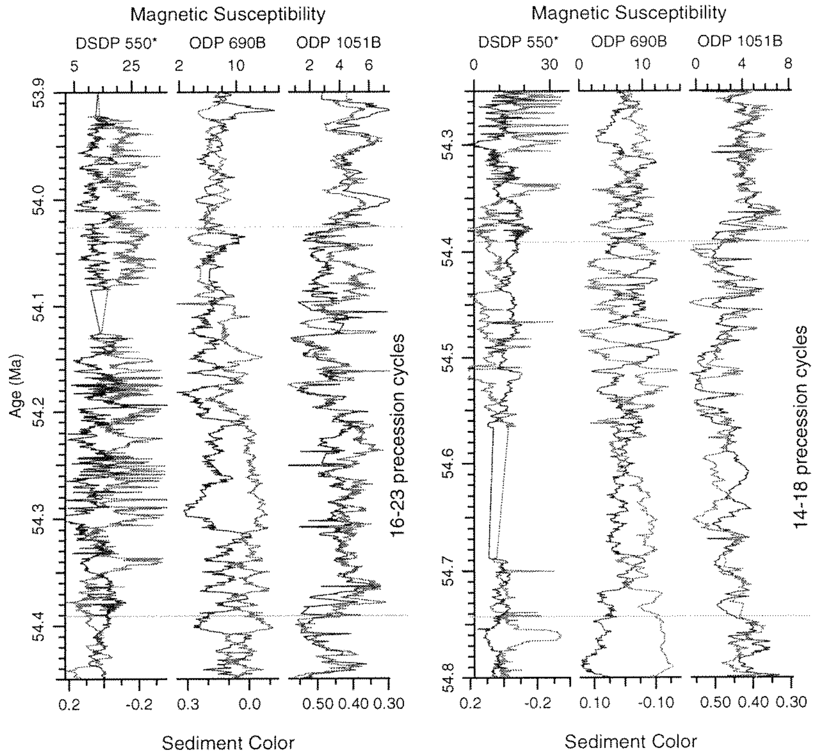

Figure 3.6: Geophysical logs (cont.).

3.4.2 Temporal representation

We recognize only two hiatuses in the sections studied, each of which is clearly identifiable by the carbon isotope records as well as being implied by magneto- and biostratigraphic correlations. The first occurs in Hole 690B between samples 15-4-51 and 15-4-66. There is not a prominent lithologic change at this level, although the thickness of (precessional) cycles decreases substantially. The hiatus is obvious from the carbon isotope record as an abrupt 0.8 ‰ increase where correlation with the other three sites indicates that values should decrease if the section were continuous. The increase corresponds with a contact between nannofossil zones NP11 and NP14, supporting the presence of a hiatus. The second hiatus occurs at Site 550 and is marked by a manganese-rich interval that is unmistakeable in the core. Carbon isotope values decrease by >1.5 ‰ through this interval which also contains a contact

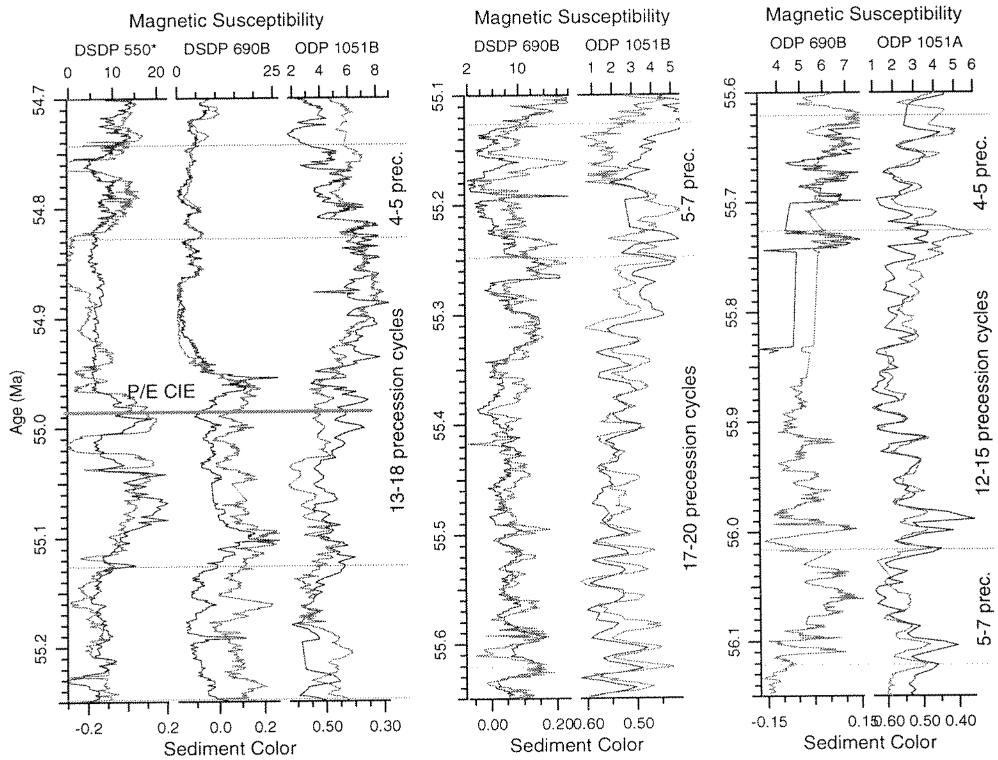

Figure 3.6: Geophysical logs (cont.).

between zones NP5 and NP9 and truncates the base of Chron C25n. The difference in lithologic expression between these two hiatuses likely reflects a difference in mechanism: the hiatus at site 550 appears to represent a period of sediment starvation resulting in a thick manganese-rich condensed interval while the lack of a lithologic expression at site 690 implies instead an erosional mechanism with no period of slow sedimentation.

The Site 690 record encompasses only eccentricity maxima 'a'-'g', due to the hiatus at the top of this section, and the hiatus at Site 550 appears to truncate the base of eccentricity maximum 'a', although the quality of the δ^{13}C data in the overlying interval is poor due to low carbonate content and it is therefore difficult to delineate the eccentricity cycles. Much of the middle portion of the record is compromised at Site 577 due to poor core recovery and a 30 cm organic geochemistry sample. The cycles are easily correlated among the four sections and the correlation is reinforced by the similarity of long term (>1 m.y.) trends in isotope values (Figure 3.3). The records at Site 1051 and 550 therefore span >3.645 m.y.; the record from Site 690 spans the lower >2.43 m.y. of this interval with a gap of ~0.15 m.y. between Cores 21 and 22 and the record from Site 577 spans the entire interval with two gaps of ~0.2 m.y. where the organic geochemistry sample was taken and ~0.4 m.y. between Cores 9 and 10.

3.4.3 Integration of magneto- and biostratigraphy

The correlation of magnetic polarity reversals among the four sites relative to the eccentricity timescale is excellent (Figure 3.5). There are some short normal polarity intervals near the top of C24r that are questionable and likely reflect overprinting. However, the fact that some normal polarity intervals appear to be approximately correlative at sites 690 and 1051 suggests that there may be some consistency imparted either by one or more cryptochrons or (more likely) a time period of low field intensity. We also note the presence of a single normal polarity sample coincident with the LPTM at sites 550, 690, and 1051. This is most likely due to the lithologic change that occurs at all sites during this event; we would regard it as exceedingly fortuitous if a geomagnetic field perturbation occurred coincident with the biogeochemical perturbation. The C24n.2r/C24n.3n reversal occurs immediately below eccentricity maximum 'i' at Site 550 and 1051; the reversal is somewhat lower at Site 577, but the discrepancy is actually due only to a single sample. The C24n/C24r reversal occurs in the lower portion of the interval between eccentricity maxima 'g' and 'h' at Sites 577, 550 and 1051. Neither of these reversals is present at Site 690 due to a hiatus. The C24r/C25n reversal is located between eccentricity maxima 'b' and 'a' at all four sites while the base of Chron C25n occurs just below maximum 'a' at Sites 577, 690, and 1051. The latter reversal is not present at Site 550 due to a hiatus. In general,

Chron	Hole	Samples	Duration	Age at base
C24n.2r	1051A	46-2, 5 to 46-3, 63	—	52.80–52.87
	1051B	50-2, 145 to 50-3, 94	—	52.79–52.82
	550*	28-2, 138 to 28-3, 36	—	52.80–52.84
	690B	—	—	—
	577*	9-4, 24 to 9-4, 64	—	(52.97–53.17)
C24n.3n	1051A	48-1, 144 to 48-5, 65	(0.61–0.87)	(53.48–53.67)
	1051B	52-3, 137 to 52-4, 80	(0.70–0.76)	53.52–53.55
	550*	29-3, 34 to 29-3, 103	0.59–0.67	53.43–53.47
	690B	—	—	—
	577*	9-5, 21 to 9-5, 61	(0.41–0.72)	(53.58–53.69)
C24r	1051A	57-1, 57 to 57-1, 108	(2.19–2.42)	55.86–55.90
	1051B	61-5, 129 to 61-6, 39	2.25–2.34	55.80–55.86
	550*	35-6, 101 to 36-1, 22	(2.38–2.48)	(55.85–55.91)
	690B	22-1, 86 to 22-1, 137	—	55.86–55.87
	577*	10-2, 82 to 10-2, 122	(2.10–2.28)	55.79–55.87
C25n	1051A	57-4, 51 to 57-4, 120	0.31–0.40	56.21–56.26
	1051B	—	—	—
	550*	36-2, 101 to 36-2, 117	(0.13–0.20)	(56.04–56.05)
	690B	23-3, 137 to 23-4, 12	0.41–0.44	56.28–56.29
	577*	10-3, 119 to 10-4, 63	(0.35–0.66)	(56.21–56.45)

Table 3.3: Calibrated ages of magnetostratigraphic marker events. See Table 3.2 for explanation. Age calibrations enclosed in parentheses indicate that the calibration is suspect and not included in the age calibrations in Table 3.5.

the error in the calibrated age at each site is greater than the mismatch between sites (Table 3.3).

Boundaries between nannofossil zones are correlative within ~100 k.y. among sites 577, 550 and 1051, except for the NP8/NP9 boundary which is significantly different between Sites 577 and 1051 (the boundary is not present at Site 550 due to a hiatus) (Figure 3.5, Table 3.4). At Site 690, the bases of Zones NP11 and Subzone NP10d correlate well with the other sites. However, the base of Zone NP10 is delayed by ~0.6 m.y. at Site 690 relative to the other sites and the base of Zone NP9 is delayed by ~0.3 m.y. relative to Site 577 (although correlative with Site 1051). These discrepancies cannot be explained by inserting hiatuses; all eccentricity maxima are reflected by $\delta^{13}C$ events at each site and the calibration is confirmed by cycle counts in the geophysical logs for Site 690 (Figures 3.6, 1.6). In Chapter 1, I suggested that a hiatus was present at Site 690 between the CIE and the base of NP9 and we note that the carbon isotope records imply a temporal gap at the level of the NP8/NP9 contact. However, this temporal gap occurs between cores 21 and 22; core 21, section 4 is severely disturbed due to a collapsed liner while the upper 40 cm of core 22, section 1 shows severe drilling disturbance. We therefore prefer to interpret this temporal gap as lack of recovery rather than a hiatus in sedimentation.

3.5 Discussion

The method used to construct the chronology presented here is robust because it combines the cyclostratigraphic and chemostratigraphic advantages of $\delta^{13}C$ records. Carbon isotope records have been used as a correlation tool in previous studies of the latest Paleocene-earliest Eocene [121, 127] but only from an empirical standpoint: similarities in carbon isotope records were assumed to correlate due to the two-order-of-magnitude difference between the ocean mixing time (10^3 yr) and the residence time of carbon (10^5 yr). Placing the variations in $\delta^{13}C$ within a Milankovitch framework adds a predictable element that is lacking for most correlation tools: there is a temporal implication to the identification of carbon isotope events. The use of $\delta^{13}C$ records is also an improvement over most other cyclostratigraphic proxies, which are of little use in site-to-site correlation. It is similar to the now ubiquitous use of oxygen isotope records in the Pleistocene.

The calibrated durations of magnetic polarity chrons C25n, C24r, and C24n.3n are 0.38 ± 0.06, 2.30 ± 0.05, and 0.68 ± 0.09 m.y., respectively (Table 3.5). Cande and Kent [28, 29] gave durations for the same polarity zones of 0.487, 2.557 and 0.444 m.y. Our calibrations therefore differ from the calibrations of Cande and Kent [28, 29] by 21%, 10%, and 53% for the three chrons. We do not believe that the differences in

Zone	Hole	Samples	Duration	Age at base
NP11	1051A	50-1, 57 to 50-2, 115	—	(53.80–53.84)
	1051B	52-6, 66 to 53-1, 32	—	53.64–53.70
	550*	29-6, 66 to 30-1, 20	—	53.50–53.55
	690B	15-6, 30 to 15-7, 30	—	53.67–53.71
	577*	9-5, 40 to 9-5, 72	—	53.62–53.73
NP10d	1051A	51-1, 44 to 51-2, 115	(0.09–0.17)	53.93–53.97
	1051B	54-2, 108 to 54-4, 17	0.27–0.39	53.97–54.03
	550*	30-5, 113 to 30-6, 7	0.24–0.30	53.87–53.87
	690B	16-1, 41 to 16-2, 28	(0.05–0.19)	(53.82–53.89)
	577*	9-5, 116 to 9-6, 13	(0.18–0.49)	(53.92–54.11)
NP10c	1051A	51-6, 85 to 52-1, 14	0.10–0.16	54.07–54.09
	1051B	—	—	—
	550*	31-3, 6 to 31-3, 39	0.14–0.15	53.99–54.00
	690B	—	—	—
	577*	9-6, 13 to 9-6, 24	(<0.24)	(54.11–54.16)
NP10b	1051A	52-1, 14 to 52-2, 145	<0.07	54.09–54.14
	1051B	—	—	—
	550*	31-5, 88 to 32-1, 17	0.09–0.16	54.07–54.13
	690B	—	—	—
	577*	9-6, 24 to 9-6, 43	(<0.13)	(54.16–54.24)
NP10a	1051A	55-1, 56 to 56-1, 55	(0.57–1.03)	(54.70–55.12)
	1051B	—	—	—
	550*	34-3-125 to 34-4-2	0.62–0.70	54.84–54.85
	690B	17-3, 43 to 17-3, 43	—	(54.31–54.31)
	577*	9-6, 123 to 10-1, 30	(0.34–0.90)	(54.58–55.05)
NP9b	1051A	—	—	—
	1051B	59-3, 95 to 60-1, 38	—	(54.68–54.72)
	550*	—	—	—
	690B	—	—	—
	577*	—	—	—
NP9	1051A	56-6, 104 to 57-1, 57	(0.59–1.15)	55.71–55.86
	1051B	—	—	—
	550*	36-2, 84 to 36-3, 7	(1.11–1.16)	(56.03–56.07)
	690B	22-1, 50 to 22-1, 68	(1.55–1.56)	55.86–55.87
	577*	10-3, 90 to 10-3, 135	(1.08–1.68)	56.14–56.25

Table 3.4: Calibrated ages of nannofossil biostratigraphic marker events. See Table 3.2 for explanation. Age calibrations enclosed in parentheses indicate that the calibration is suspect and not included in Table 3.5.

Datum or Zone	Duration	Error	Age at base	Error
C24n.2r	—	—	52.83	0.07
C24n.3n	0.68	0.09	53.49	0.07
NP11	—	—	53.61	0.08
NP10d	0.32	0.06	53.92	0.07
NP10c	0.13	0.05	54.04	0.07
NP10b	0.08	0.06	54.11	0.10
+19 ash	—	—	54.30	0.07
−17 ash	—	—	54.51	0.05
NP10a	0.66	0.05	54.85	0.07
NP9b	—	—	54.70	0.07
P/E CIE	—	—	54.97	0.07
C24r	2.30	0.05	55.86	0.07
NP9	(1.2)	(0.3)	55.95	0.28
C25n	0.38	0.06	56.25	0.07

Table 3.5: Calibrated ages of various stratigraphic marker events. The error estimates for these calibrated ages reflect errors from several sources. All reflect the error of ± 0.05 m.y. for the $^{40}Ar/^{39}Ar$ analysis on the −17 ash. An error of ± 0.06 m.y. is added due to the astronomical calibration (0.03 m.y. each for registry of the −17 ash and the calibrated marker, as discussed in the text). Finally, the error due to sampling intervals and mismatch between sites is added (see Tables 3.2– 3.4).

duration of C25n and C24r are significant. The difference in duration of C24r (10%) is close to the error cited by Cande and Kent [28] for the width of anomaly 24 (9.4%) while the error in our calibration of the duration of C25n (primarily due to spacing between samples for sediment magnetic polarity records) combined with an error of 9.7% for the width of anomaly 25 [28] is sufficient to reconcile the two calibrations. As confirmation of this assessment, the durations presented here are within the range of calibrations for these chrons by previous authors (Figure 3.7 [88]). The duration for C24n.3n is more troublesome. While Cande and Kent [28, 29] used a slightly misplaced calibration point of 55 Ma for a position within anomaly 24 to construct the seafloor spreading rate history on which their timescale is based, we have recalculated the spreading rate history using a revised calibration point based on the chronology presented here to confirm that this cannot account for the differences cited above. The duration calculated for C24n.3n indicates either 1) there was an anomalously rapid

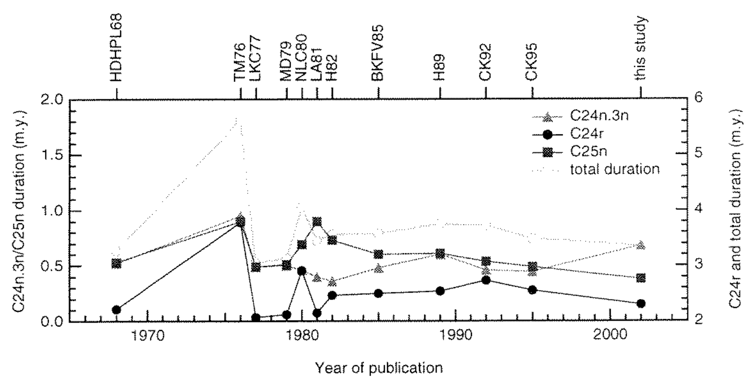

Figure 3.7: Comparison of estimated durations for magnetic polarity zones according to year of publication.

increase in spreading rates in the South Atlantic during this time or 2) the magnetic polarity records for the sites presented here are compromised in some fashion. While we find no supporting evidence for the latter possibility (in fact, the total duration of the three chrons is slightly lower than in Cande and Kent [29, Figure 3.7]), we find the former conclusion sufficiently unlikely (spreading rates would have had to be 50% higher than predicted by the assumption that spreading rates should vary smoothly) that we recommend caution in using our calibration for this interval until it is validated by longer records. Conversely, the fact that the durations for C24r and C25n presented here are not significantly different from the calibrations of Cande and Kent [29] leads us to conclude that this portion of our chronology is quite robust.

Our calibrated age for the P/E CIE of 55.97 $\pm$ 0.07 Ma (Table 3.5) is 0.38 up in Chron C24r. This estimate differs from that of Aubry et al. [6] due primarily to the much shorter duration between the CIE and the base of Zone NP10 used in the present calibration. By correlating the Zone NP9/NP10 contacts at Sites 550 and 690, Aubry et al. [6] assumed that a hiatus had to be present at Site 550, thereby artificially extending the upper part of Chron C24r. Our calibration places the CIE 0.88 m.y. above the base of Chron C24r, differing by $\sim$0.07 m.y. from the calibration of Norris and Röhl [95] who placed the P/E CIE 0.924-0.966 m.y. above the base of Chron C24r. Norris and Röhl [95] also estimated a duration for Chron C25n of 0.481–0.523 m.y., which differs from our calibration of 0.38 (±0.17) m.y. The latter discrepancy results from the improved magnetostratigraphy presented here. Although the difference in the position of the C24r/C25n reversal is only ~1 m, the precession cycles in this interval are ~20 cm thick so the difference amounts to ~100 k.y. However, this means that the actual difference between our cyclostratigraphy and that of Norris and Röhl [95] in the interval below the CIE is ~0.17 m.y. The lithologic cyclicity is extraordinarily well-defined throughout most of this interval (Figure 3.6), and the two cyclostratigraphies are nearly identical as a result. However, in the ~4 m interval immediately below the CIE (within the interval between the CIE and the base of E2.C24r) there are two intervals where the lithologic cyclicity is disturbed. The upper interval is noted as an intraformational mud clast horizon (Hole 1051B, Core 60X, Section 2, 42-65 cm, [100]; 512.76-512.98 MCD in [95]) at the very base of the CIE, as highlighted by Katz et al. [65]. The lower interval shows an alternation of burrow-homogenized sediment and laminated intervals (Hole 1051B, Core 60X, Section 4, 0-118 cm, [100]; ~515.3-516.5 MCD in [95]). While Norris and Röhl [95] identified 5-6 cycles in the lower interval and 1 cycle in the upper interval this cannot be made consistent with the eccentricity cycles. Instead we suggest that each of these intervals was deposited rapidly (in a fraction of a precession cycle) and that only the cyclicity between the two intervals is interpretable as precession-driven (note that Figure 3.6 does not reflect this interpretation as we have made no attempt to tune our age models at the precession scale). The remainder of the discrepancy can be attributed to differences in the correlation between Holes 1051A and1051B and apparent cycles created by drilling disturbance.

The correlation presented here demonstrates substantial diachrony of some nannofossil first appearances between the Southern Ocean Site 690 and the other sites studied. Significantly greater diachrony was known to exist in this time period among planktonic foraminifera [e.g., 126], but diachrony among nannofossils could not previously be determined. However, we also demonstrate that first appearances are

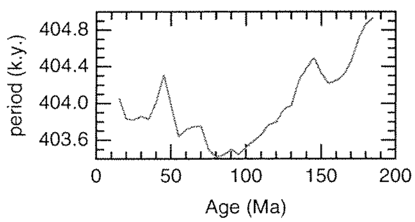

Figure 3.8: Evolution of the ~0.4 m.y. eccentricity period over 200 Ma. The period was obtained by subtracting the secular frequencies of Jupiter and Venus (g2−g5), as calculated for 200 Ma by Laskar [77]. Note that the calculated period cannot be used as the "true" period but instead provides a measure of the expected variability in this period due to chaotic interactions in the solar system.

essentially synchronous between the North Atlantic and North Pacific oceans. This suggests a substantial gradient in the surface ocean environment separating high southern latitudes from the rest of the world. Moreover, the Southern Ocean first appearances at the top of the interval presented here are essentially synchronous with those at the other three sites, consistent with inferences from other data of a decrease in gradients between high and low latitudes in the early Eocene climatic optimum.

It is tempting to try to evaluate the "true" error in the ^{40}Ar/^{39}Ar age (and thus the error in the calibration of the decay rate) by using the orbital solution. We recognize three prominent eccentricity cycles in the δ^{13}C records: ~0.1 m.y., ~0.4 m.y., and ~2.4 m.y. (e.g., Figure 3.3). In order to correctly calculate the phase at ~55 Ma the period of each component would have to be known at a precision <0.1%, <0.4% and <1%, respectively. Due to the chaotic nature of the solar system the periods for the ~0.1 m.y. (~0.3%) and ~2.4 m.y. (~5%) components exceed this threshhold, but the expected variability in the ~0.4 m.y. component is only ~0.2% [see Fig. 8 and Table X in 77]. The period for the latter component varies between 0.4034 and 0.4050 m.y. over the last 200 Ma, and between only 0.4036 and 0.4044 m.y. over the last 60 Ma [Figure protect3.8, calculated based on Fig. 8 in 77].

The resulting expectation for the ~0.4 m.y. eccentricity variation is ~90° (~0.100 m.y.) out of phase with the δ^{13}C variations plotted relative to our timescale calibration (Figure 3.9). This is larger than the analytical error associated with the ^{40}Ar/^{39}Ar age for the −17 ash (54.51±0.05 Ma) and implies that the decay rate

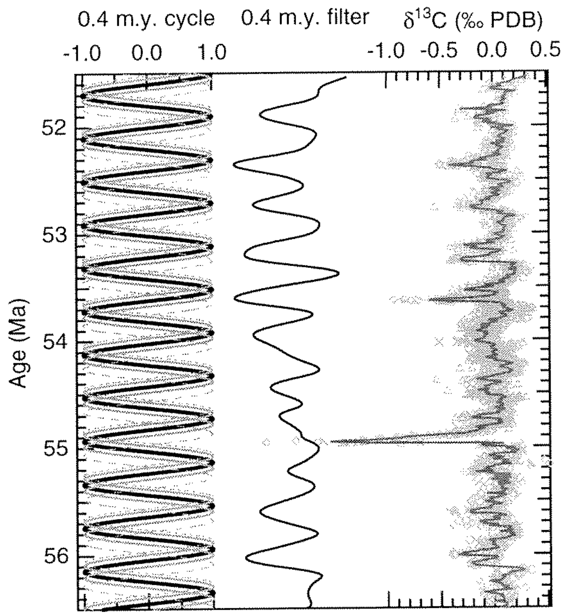

Figure 3.9: Comparison of the phase for the calculated ~0.4 m.y. eccentricity cycle with that obtained from $\delta^{13}C$ records. The stacked $\delta^{13}C$ records (far right) have been filtered to emphasize the ~0.4 m.y. component (center) using a gaussian bandpass filter centered at a period of 0.4 m.y. The minima in this curve should correspond with maxima in calculated eccentricity (far left); the offset in phase suggests that the $^{40}Ar/^{39}Ar$ calibration is in error by a minimum of 0.18%. For the calculated eccentricity cycle, the thick black curve was calculated using a period of 0.4040 m.y., thinner grey curves were calculated using periods of 0.4036 and 0.4044 m.y., and dashed curves were calculated using periods of 0.4034 and 4050 m.y.

calibration is in error by 0.18% at a minimum. Unfortunately, the maximum error in this calibration cannot be estimated because we cannot differentiate errors separated by integer multiples of the ~0.4 m.y. cycle. This could be resolved if it was possible to calculate the period of the ~2.4 m.y. cycle more precisely, but that period will instead have to be calibrated using the geologic record.

3.6 Conclusion

We have demonstrated the usefulness of using carbon isotope records to constrain both astronomical time-scale calibrations and cyclostratigraphic correlations. Barring unforeseen complications, we suggest that this method can potentially allow correlation throughout the Cenozoic and for large portions of the Cretaceous with similar precision to that attained in Pleistocene marine sediments. Moreover, it allows a true test of the accuracy of astronomical timescales through correlation independent of bio- and magnetostratigraphic criteria. The resulting astronomical calibrations will therefore be more robust than those reliant on precession-scale cyclicity at individual sites.

Application of this method to the previously intractable Paleocene/Eocene boundary interval has resulted in a robust chronology with several significant differences relative to previously proposed chronologies. We have determined that, while some nannofossil first appearances are significantly diachronous between the Southern and other oceans, in general the assumption that they are essentially synchronous during this time period is valid. The duration of magnetic polarity chrons as determined here is somewhat different than previous determinations, although only significantly different in the case of Chron C24n.3n. Finally, linking the astronomical chronology to $^{40}Ar/^{39}Ar$ ages results in an age of 54.97 $\pm$ 0.07 Ma for the Paleocene/Eocene boundary and the associated climatic and biotic perturbations.

Chapter 4

A comet impact trigger for the Paleocene/Eocene thermal maximum and carbon isotope excursion?*

4.1 Abstract

We suggest that the rapid onset of the carbon isotope excursion (CIE) at the Paleocene/Eocene boundary (~55 Ma) may have resulted from the accretion of ~900 Gt of ^{12}C-enriched carbon from the impact of a volatile-rich comet, an event which would also trigger greenhouse warming leading to the Paleocene/Eocene thermal maximum. New evidence of an impact is the unusual abundance of magnetic nanoparticles in kaolinite-rich shelf sediments from the Atlantic Coastal Plain that coincide with the onset and nadir of the CIE. TEM observations suggest that the magnetic nanoparticles are not of biogenic origin but, by analogy with the reported detection of iron-rich nanophase material at the Cretaceous/Tertiary boundary, can be interpreted as derived from an impact plume condensate. Published reports of a significant albeit small iridium anomaly at or close to the Paleocene/Eocene boundary provide supportive evidence for an impact.

*D.V. Kent, B.S. Cramer, L. Lanci, D. Wang, J.D. Wright, and R. Van der Voo, manuscript rejected by *Science*, 2001, and *Nature*, 2002.

4.2 Introduction

The Paleocene/Eocene (P/E) boundary (~55 Ma) is marked by a very rapid carbon isotope excursion (CIE) recorded in marine and terrestrial systems [e.g., 67, 73] that is coincident with an equally rapid oxygen isotope excursion interpreted as the P/E thermal maximum [149]. Closely associated with the P/E boundary was the largest deep-sea benthic extinction of the past 90 m.y. [133] as well as a major radiation of mammals [81]. A widely accepted explanation for the CIE is the sudden dissociation of ^{12}C-enriched marine gas hydrates [35, 36, 63]. Such a major dissociation event would seem to require either a thermal [36] or mechanical [64] precursor. However, high-resolution oxygen and carbon isotope records have failed to demonstrate a significant warming immediately preceding the CIE [e.g., 10, 21, 132]) and a geologic event of sufficient magnitude to provide a plausible mechanical trigger has not been identified.

We suggest that the impact of a volatile-rich comet provides an alternative source of ^{12}C-enriched carbon to account for the rapid onset of the CIE. The massive introduction of carbon directly into the atmosphere would account for the concomitantly rapid greenhouse warming, producing newly corrosive and warmer (and hence less oxygenated) bottom waters that have previously been suggested as proximate causal mechanisms for the massive extinction of benthic organisms coincident with the CIE [67, 133]. An impact has been entertained as one of several possible explanations for a small but analytically significant iridium anomaly detected at or very close to the P/E boundary [39, 113]. New evidence for an impact at the P/E boundary is the discovery of abundant magnetic nanoparticles in kaolinitic clays that are closely associated with the CIE in shelf sediments on the Atlantic Coastal Plain.

4.3 Magnetic nanoparticles at the CIE

Anomalously highly magnetized sediments were found uniquely associated with the CIE in a shallow marine section from a borehole drilled at Ancora, New Jersey [76, 92].

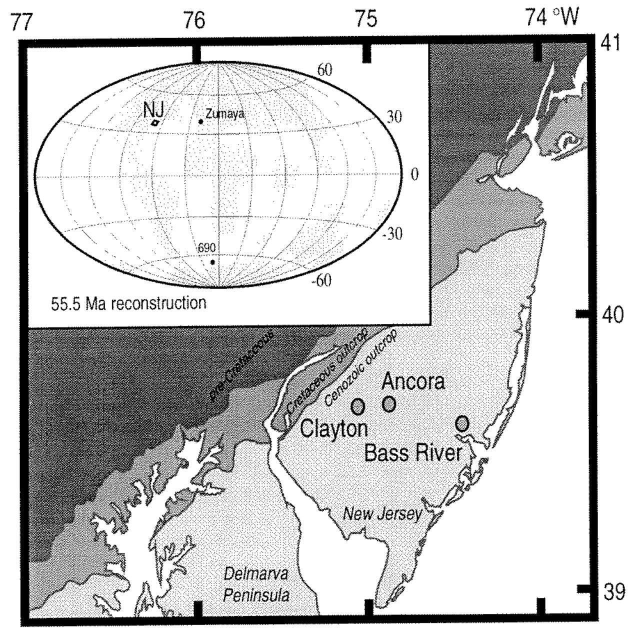

Figure 4.1: Location map for Ancora [92], Bass River [93] and Clayton [45] drill sites on the Atlantic Coastal Plain of New Jersey where the CIE interval was investigated in this study. Inset shows locations of some other CIE sites discussed in the text.

New data substantiate this observation at two other coring sites on the Atlantic Coastal Plain of New Jersey, Bass River [32, 93] and Clayton [45] (Figure 4.1). Magnetic hysteresis measurements on bulk sediment samples (Figure 4.2a) from the ~4.5 to 7.5 m-thick interval in these cored sections are characterized by Ms intensities that are typically an order of magnitude greater than in the underlying or overlying sediments (Figure 4.3). More significantly, moderate coercivities and high Msr/Ms ratios averaging 0.40 at the more proximal (landward) Clayton site, 0.35 at Ancora, and 0.3 at the more distal Bass River site indicate that the high magnetizations correspond to an assemblage of magnetite nanoparticles concentrated in the single domain size range. Experimental data [41] and theory [94, 144] show that, unless elongated, magnetite grains have a very narrow stable single domain size range between the superparamagnetic threshold of 30–50 nm and the multidomain threshold of about 70–100 nm (Figure 4.2b). For example, the average Msr/Ms for randomly oriented, non-interacting cuboid magnetite grains is calculated to drop precipitously from 0.40 for 90 nm grains to multidomain-like values of 0.06 for 10^4 nm grains [94].

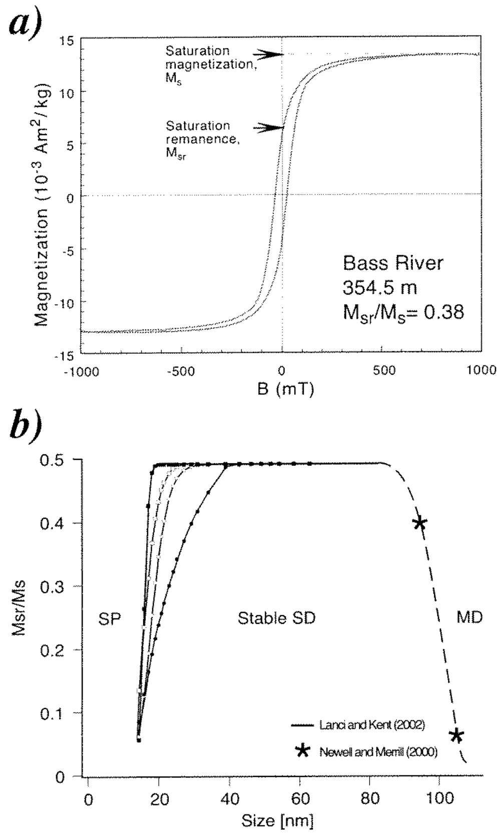

Figure 4.2: a) Example of a magnetic hysteresis loop determined on ~20 mg bulk sediment sample from the CIE interval in the Bass River core. Measurements were made on an alternating gradient force magnetometer (Micromag 2900) using a maximum field of 1.0 T and a standard correction for the high field paramagnetic slope from 0.7–1.0 T. b) Hysteresis parameters Msr/Ms as a function of grain size calculated for cubic magnetite grains showing the range where the thermal activation is effective in changing the magnetic behavior of very fine particles (after [75]). The upper size limit of the stable SD region is illustrated by calculations of the grain-size dependence of Msr/Ms by [94].

The highly restricted magnetic grain-size range is unusual and not expected to result from an assemblage of detrital magnetic minerals and the heterogeneity of neritic sedimentary processes, especially over several meters of section. A TEM study of a sample from the CIE interval at Clayton shows that iron-rich grains are difficult to detect and are likely to be very small. Four iron-rich grains have been observed and two were confirmed as magnetite on the basis of their diffraction pattern. Their grain sizes of ~70nm are well within the single domain grain size range (Figure 4.4), consistent with the hysteresis data. The magnetite grains have equidimensional shapes but they do not occur in elongate strings, suggesting they are not of biogenic origin [30].

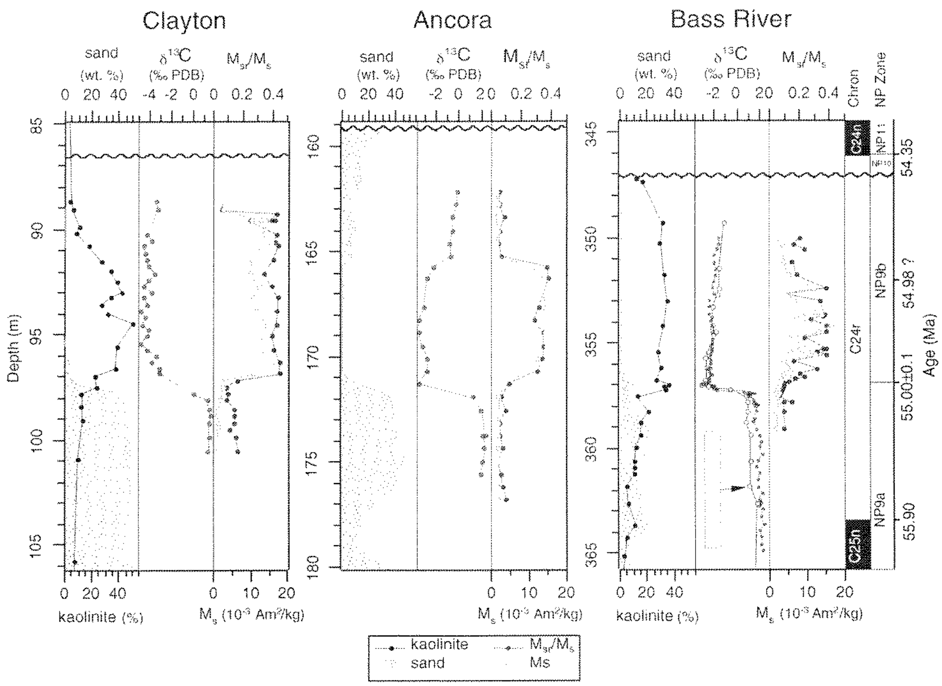

Figure 4.3: Lithologic, isotopic and magnetic hysteresis profiles across the CIE interval in three drill sites on the Atlantic Coastal Plain of New Jersey (see Figure 4.1 for locations). Thick horizontal grey line marks the onset of the CIE interval. Magnetostratigraphic, biostratigraphic, lithologic and benthic foraminiferal isotopic data for Bass River from [32], lithologic data for Clayton from [45]. The sand-fraction record does not differentiate between largely quartz and glauconite sand below the CIE and exclusively biogenic (e.g. foraminiferal) sand within the CIE interval. Bulk carbonate carbon isotope data was generated for this study. Samples for carbon isotope analysis were ground and reacted in phosphoric acid (H_3PO_4) at 90°C in a Multiprep system attached to a Micromass Optima mass spectrometer. The close correspondence between bulk carbonate and benthic foraminiferal δ^{13}C records at Bass River indicates that the bulk carbonate δ^{13}C records accurately reflect local seawater dissolved inorganic carbon at the time of deposition. The magnitude of the δ^{13}C decrease recorded in these sections (-4 to -5 ‰) is substantially larger than that recorded in deep-sea records, but is similar to the atmospheric/surface-ocean records of surface-dwelling planktonic foraminifera [67] and terrestrial carbonates [20, 73]. Magnetic hysteresis parameters were determined on ~20 mg bulk sediment samples, as illustrated in Figure 4.2. Saturation magnetization (Ms) and the ratio of saturation remanence to saturation magnetization (Msr/Ms), a sensitive probe of domain structure [40], were calculated following a standard correction for the high field paramagnetic slope from 0.7–1.0 T.

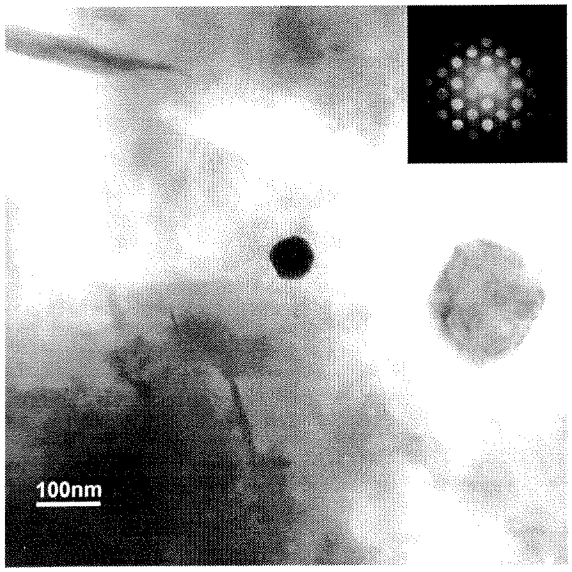

Figure 4.4: TEM bright field image of a magnetite grain (dark object in center of field) from a sample at 96.35 m in the CIE interval at Clayton. Convergent beam electron diffraction (CBED) pattern ([011] diffraction) of the magnetite grain is shown as inset.

Iron-rich nanophase material has been detected using Mssbauer spectroscopy at several Cretaceous-Tertiary (K/T) boundary sites and interpreted as a condensate from an impact ejecta plume [137, 139]. The dominance of magnetic nanoparticles inferred from hysteresis data in the CIE interval at the three Atlantic Coastal Plain sites may have a similar origin and, if so, provides evidence for a major impact at the P/E boundary. Rapid nucleation and limited crystal growth during cooling of an expanding plume vapor can account for the absence of larger magnetic grains. Although ultrafine superparamagnetic grains (<30 nm) that may also be produced in the plume condensation process will have reduced Msr/Ms [75, 130], their volumetric contribution to bulk magnetic hysteresis properties will tend to be small.

4.4 Lithologic changes at the CIE

The CIE interval at the New Jersey P/E sections is closely associated with a clay unit in which the proportion of kaolinite becomes significantly higher and terrigenous sand is conspicuously absent [32, 45] (Figure 4.3). Intervals relatively enriched in kaolinite have been documented coincident with the CIE in shelf sediments around the Tethys [14] and in New Zealand [63], and in deep-sea sediments from the Southern Ocean [108]. Kaolinite is the product of intensive continental weathering, generally under hot, humid conditions over significantly longer time scales (10^5–10^6 years [131]) than is represented by the onset and nadir of the CIE ($<10^3$–10^4 years [109]). One possible explanation for the sudden increase in kaolinite is the reworking of Upper Cretaceous kaolinites, but there is no obvious mechanism for preferential erosion and redeposition of these deposits [32]. Moreover, samples we collected from exposures of the Upper Cretaceous Raritan Fm. at Sayreville, NJ, have very low Msr/Ms ($\sim$0.04), documenting that high Msr/Ms values are not intrinsically associated with kaolinitic deposits.

Alternatively, the sudden increase in kaolinite content may have resulted from an intensification of chemical weathering at the onset of the CIE. Although it is unlikely that this would result from climate change alone [131], enhanced weathering rates would be expected for a layer of very fine-grained dust, such as an impact ejecta blanket. The close correspondence of the kaolinite-rich interval with minimum carbon isotope values (Figure 4.3) indicates that this unit was deposited very rapidly. In open ocean sections, such minimum carbon isotope values occur over an interval of a few decimeters at most [10], suggesting a duration of 20–100 k.y. [e.g., 109]. This is consistent with the presence throughout this interval in the New Jersey sections of calcareous nannoplankton and planktonic foraminiferal taxa that are restricted to the early part of the CIE interval at other locations [7, 9, 33, 66, 92]. We therefore conclude that the CIE clay unit at the New Jersey P/E sections was deposited at rates exceeding 30–70 cm/k.y., as the unconsolidated impact dust blanket was rapidly weathered and eroded from the land and redeposited on the continental shelf. Under these circumstances the remarkable homogeneity of the magnetic, lithologic, and isotopic properties of these sediments is not surprising. Rapid weathering, erosion and redeposition of an impact ejecta blanket would also account for the abrupt transition (over $\sim$10 cm) from typical neritic sandy and silty clays below the CIE to kaolinite-rich

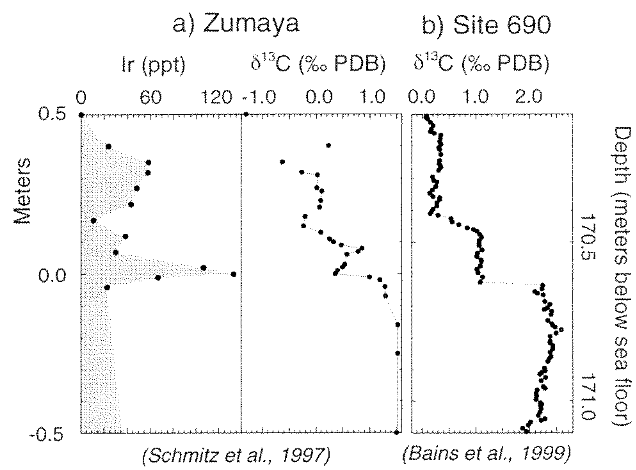

Figure 4.5: a) High resolution profiles of bulk carbonate δ^{13}C and iridium concentrations across the onset of the CIE recorded in Zumaya, Spain (from Figure 2 in [113]. b) High resolution profile of bulk carbonate δ^{13}C across the onset of the CIE from ODP Site 690 from the Southern Ocean (from Figure 2 in [10]). Both records show a stepped decrease in δ^{13}C after the initial -1 ‰ shift, which coincides with the iridium anomaly at Zumaya. Note that no intermediate values are resolved in the initial shift at either site, while subsequent steps are more gradual.

clays containing very little silt and only non-terrigenous (e.g., foraminiferal) sand-size material.

4.5 Other evidence for an impact

Supportive independent evidence of an impact event at the P/E boundary is a reproducible iridium anomaly (quoted values of 143±22 ppt and 133±15 ppt Ir compared to a background of about 38 ppt Ir) in an expanded bathyal section at Zumaya, Spain [113]. The anomaly occurs in a 1 cm-thick grey layer that is coincident with the initial ~1 ‰ decrease in δ^{13}C values marking the onset of the CIE (Figure 4.5a).

Although the iridium enrichment was regarded as enigmatic [113] and could be due to various other causes such as basaltic volcanism [112], the precise coincidence of the sharp iridium anomaly with the base of the CIE at Zumaya is remarkable and predicted for an impact origin (Figure 4.5a). An iridium anomaly has also been reported more recently from near the P/E boundary in flysch deposits in Slovenia [39], although in the absence of carbon isotope data it is not possible to determine if it coincides with the CIE.

Evidence from osmium and helium isotopes is more equivocal. If the onset of the CIE was associated with an extraterrestrial impact it might be expected to have low $^{187}Os/^{188}Os$ isotope ratios. An excursion to higher values of $^{187}Os/^{188}Os$ isotope ratios was found in DSDP Site 549 from the North Atlantic and attributed to a global increase in chemical weathering rates over several hundred thousand years during an interval of unusually warm global climate following the CIE [106]. However, the sampling interval (12 samples over $\sim$400 k.y.) was insufficient to capture the rapid onset of the event and the data is therefore inconclusive regarding the triggering mechanism. As Ravizza et al. [106] point out, in a longer osmium isotope record from North Pacific core GPC3 [101], an osmium isotope minimum occurs in an interval that has been correlated with the P/E boundary [91]. We suggest that although the origin of this minimum is highly uncertain [101, 106], a contribution from extraterrestrial osmium cannot be excluded.

Core GPC3 also yielded a continuous record of extraterrestrial helium borne by the fallout of interplanetary dust particles over the past 70 m.y. [42]. The observation that the Cretaceous/Tertiary boundary, which is identified in these sediments by a large iridium peak [74], has no associated peak in extraterrestrial helium can be explained by devolatization of large bodies during impact [42]. Accordingly, the absence of a significant increase in extraterrestrial helium at around the P/E boundary in this core may not be very relevant to the issue of an impact at that time.

4.6 Estimate of comet size from carbon isotope evidence

Lacking any other major source of sufficiently ^{12}C-enriched carbon, it has been assumed that the CIE resulted from dissociation of seafloor methane hydrate deposits having $\delta^{13}C$ values of ~ -60 ‰ [35, 36]. However, the evidence for an impact event points to an alternative, extraterrestrial source of ^{12}C-enriched carbon. This is feasible because space probe measurements of comet Halley show that cometary dust contains up to ~25% carbon with $^{12}C/^{13}C$ ratios as high as 5000 compared to normal values of about 89 [61]. Interplanetary dust particles collected in the Earth's atmosphere and thought to represent cometary dust are also often rich in carbon [135] and have $\delta^{13}C$ values of −45 ‰ or lower [89].

Assuming a cometary source of ^{12}C-enriched carbon, the magnitude of the CIE can be used to estimate the size of the P/E impactor using a simple mass balance equation. The CIE is characterized by a stepped decrease in $\delta^{13}C$ values, but the initial negative shift of ~1 ‰ is significantly more abrupt than subsequent steps and must have occurred in much less than 1000 years [10] (Figure 4.5b). A comet impact would be called upon to account only for this initial 1 ‰ decrease, which we note is coincident with the Ir anomaly at Zumaya [113]. For a cometary body with −45 ‰ $\delta^{13}C$, ~900 Gt ofextraterrestrial carbon would account for a 1 ‰ decrease in the total exchangeable carbon reservoir (Figure 4.6). The equivalent diameter of such a comet with 25 wt. % carbon and bulk density 2000 kg/m^3 would be ~15 km. This estimate has a large uncertainty given the poorly known properties of comets and magnitude of the perturbed carbon reservoir.

The nominal size of the postulated P/E comet is comparable to the K/T bolide (10±4 km) whose size was estimated primarily from the iridium content of the ~1 cm thick boundary clay [2]. Our suggestion that the P/E impactor was a volatile-rich comet rather than an asteroid, with an order of magnitude lower relative concentration of rockforming elements than associated with carbonaceous chondrites [61], could help explain why there is only a small iridium anomaly found associated with the ~1 cm-thick grey layer at Zumaya [113]. Impacts of large comets are rare but not improbable events; the collision rate for comets larger than 10 km is estimated to be about 10^{-8} yr^{-1}, about a factor of three greater than for >8 km-diameter asteroids [123]. We have not identified the site of the postulated P/E impact. However, large impact

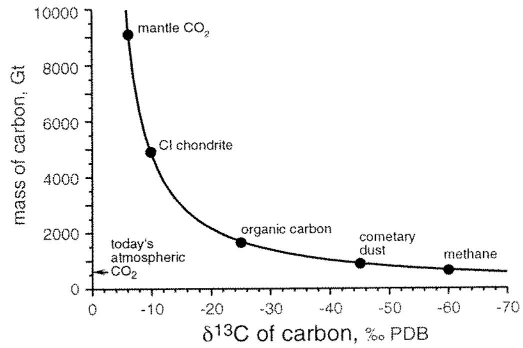

Figure 4.6: Mass of carbon as a function of its carbon isotopic composition required to produce a -1 ‰ shift in the total (40000 Gt) exchangeable ocean-atmosphere carbon reservoir with an initial δ^{13}C of -0.75 ‰ PDB. The mass of carbon necessary to cause an isotopic shift in the carbon reservoir is given by $C_a = C_i\left(\frac{\Delta\delta^{13}C}{\delta^{13}C_a - \delta^{13}C_i - \Delta\delta^{13}C}\right)$ where C_i is the initial mass of carbon of isotopic composition $\delta^{13}C_i$ in the reservoir, C_a is the mass of carbon of isotopic composition $\delta^{13}C_a$ added to the reservoir, and $\Delta\delta^{13}C$ is the change in the δ^{13}C value of the reservoir. We assume an initial reservoir mass of carbon of 40000 Gt, which is comparable to the amount of carbon in the modern ocean-atmosphere-biomass reservoir [26, 124]. The δ^{13}C of oceanic dissolved inorganic carbon immediately prior to the CIE was about 1.5 ‰ [147]; assuming a partitioning between organic and inorganic carbon similar to modern, this indicates an exchangeable carbon isotopic composition of -0.75 ‰. The mass of carbon in todays atmosphere [26, 124] is indicated by arrow on vertical axis. Nominal carbon isotopic compositions are shown for mantle CO_2 [43], CI chondrites [69], organic carbon [43], comets [89], and methane [36].

craters continue to be found on land [e.g., 103]) and, since a larger portion of the Earth's surface area is oceanic rather than continental, it must be acknowledged that the P/E impact may have occurred on oceanic crust. Impact craters of any age have been difficult to find in the ocean basins, although they must exist given the continental crater record [47].

4.7 Contribution from gas hydrates

Simultaneous mechanical disruption of sediments and consequent release of gas hydrates could conceivably be triggered by an impact event. Slumping on the continental slope would presumably have occurred coincident with continental shelf impacts such as those that created the 180 km-diameter Chicxulub crater at the K/T boundary (65 Ma) on Yucatan [128], the 85 km-diameter Chesapeake crater of late Eocene age (35 Ma) on thecoastal plain of Virginia [103] and the 45 km-diameter Montagnais crater of early Eocene age (50.5 Ma) on the Nova Scotia continental shelf [60]. However, no significant negative shift in whole-ocean carbon isotope values has been documented coincident with any of these events [e.g., 34, 147]). This suggests that the amount of methane released as a result of impact-induced slumping is insignificant relative to the whole-ocean carbon reservoir. The highest potential for release of large amounts of gas hydrate would presumably result from a direct impact in an area of gas hydrate accumulation. At the Blake Ridge, which is thought to be hydrate-rich in comparison to other areas, only ~35 Gt of carbon is present either as hydrate or gas in a 26000 km^2 area [37]. This means that the amount of methane that could be released directly by a large impact activating this entire area (equivalent to a ~180 km-diameter crater) would be too small by at least an order of magnitude to produce the initial 1 ‰ decrease at the CIE.

4.8 Greenhouse warming

The P/E impact hypothesis implies that a cometary body introduced ~900 Gt carbon directly into the atmosphere where it would have oxidized to CO_2. While there is little agreement on Paleogene atmospheric CO_2 levels, a recent estimate suggests that they may have been near present-day levels of ~300 ppm [110], or 600 Gt of carbon. The comet impact hypothesis would therefore imply an instantaneous more than doubling of atmospheric pCO_2 and the P/E thermal maximum that occurred synchronous with the CIE is an expected consequence, through greenhouse warming. The massive initial injection of CO_2 and resultant greenhouse warming would also have produced newly corrosive and warmer (and hence less oxygenated) bottom waters that have previously been suggested as proximate causal mechanisms for the mass extinction of benthic foraminifera coincidentwith the CIE [67, 133]. Bottom water warming may also have eventually resulted in thermal dissociation of gas hydrates, accentuating the environmental and carbon isotopic effects.

4.9 Conclusions

In conclusion, we believe that a comet impact provides a viable and direct alternate method of delivery of ^{12}C-rich carbon to initiate the CIE and the P/E thermal maximum. The biotic and environmental response to the hypothesized P/E impact, which included the brief dominance of an exotic excursion plankton assemblage [9, 66], a mass extinction among benthic foraminifera [67, 133], and the appearance of most extant mammalian orders including primates [81], was clearly different from that following the K/T impact [2], which resulted in massive extinctions of plankton but with little effect on benthic communities [34]. These considerations, together with large impacts that have had little apparent long-term environmental consequences [104], suggest that the effects and signatures of large impacts vary and depend strongly on factors such as the composition of the impactor [142] as well as the target area, and Earth's climate state prior to the impact. If supported by further evidence of tracers of extraterrestrial material in CIE deposits, the P/E impact may have implications for the cause of other catastrophic events accompanied by carbon isotope excursions, such as the Permo-Triassic boundary [62].

Chapter 5

Synthesis

5.1 Introduction

In the previous chapters of this thesis I have accomplished two primary goals:

1. Construction of a robust, astronomically calibrated chronology for events in a ~4 m.y. interval of the latest Paleocene-earliest Eocene, including all of Chron C24r. This is a significant accomplishment, resolving long-standing issues of stratigraphic correlation and temporal representation. The chronology presented here can be refined in detail, and the absolute numerical chronology is subject to adjustment, but it is highly unlikely that the relative numerical chronology will be significantly altered. I believe that the strategy employed (i.e. using $\delta^{13}C$ records to delineate eccentricity cycles) points the way to constructing an astronomical chronostratigraphy* for the Cenozoic and upper Mesozoic.

*My use of the phrase "astronomical chronostratigraphy" is intended to draw a distinction with the more widespread practice of establishing astronomical or cyclo- stratigraphies, useful only at individual sites. For astrochronology to succeed it must provide for correlation among sites as well as temporal calibration. In some respects the goal of astrochronologic correlation has been achieved in the Pleistocene in the form of oxygen isotope stages, but these are only informally used as chronostratigraphic units. Orbital forcing is uniquely suited to division of geologic time into chronostratigraphic units: the ~400-k.y. eccentricity cycle is an appropriate duration for investigating long-term changes while ~100-k.y. eccentricity, obliquity, and precession cycles provide natural subdivisions of this basic unit. At the same time, use of the ~400-k.y. cycle as a fundamental chronostratigraphic unit automatically imparts a temporal meaning, since the duration of this cycle

2. Placement of the Paleocene/Eocene carbon isotope excursion (CIE) within a Milankovitch framework. This provides a much-needed reality check on speculation about multiple transient climate events in the early Paleogene and triggering mechanisms for the CIE. Multiple transient $\delta^{13}C$ excursions are not only present in the early Paleogene but predictable within the Milankovitch climate paradigm. On the other hand, the CIE cannot be grouped with these multiple excursions and is anomalous in the context of Milankovitch, strongly arguing for some catastrophic triggering mechanism rather than a mechanism intrinsic to the normal climate system. One plausible catastrophic trigger is a comet impact, and I have presented some evidence in support of this hypothesis.

While these two accomplishments can be considered finished products, there are several issues that, in my own mind, are still outstanding and worthy of future research:

1. What is the best method for refining a cyclostratigraphy at sub-eccentricity resolution in the absence of a usable calculated tuning target?

2. Do the eccentricity-controlled transient $\delta^{13}C$ events correspond with climate perturbations, or are they merely an artifact produced by the interaction of precession cyclicity and the carbon residence time?

3. Is there actually any potential to invert the residence-time model and extract useful information about the evolution of the carbon cycle from $\delta^{13}C$ records, as I suggest in Chapter 2?

4. While the CIE was likely triggered by a catastrophic event, can the imprint of Milankovitch forcing be identified during the onset and recovery from the event?

can be assumed to be constant. Eventually, therefore, the goal of astrochronology must be to formalize a nomenclature for an eccentricity-based zonation integrated with magneto- and biostratigraphic zonations.

I cannot claim to have the answer to any of these questions, leaving the realm of speculation wide open. The remainder of this chapter contains such speculation, hopefully more of the reasoned than wild variety.

5.2 Astronomical tuning in the absence of a calculated target curve

Cyclostratigraphy holds a (somewhat elusive) promise of temporal resolution at the 10^3-year scale. In high resolution studies of events like the PETM such precision of temporal calibration may be critical to interpretations. In order to achieve this, it is necessary to analyze the short period orbital oscillations - obliquity and precession. In the late Neogene (<20 Ma), where numerical orbital solutions can be assumed to be fairly accurate [78], this analysis is accomplished by tuning a climate proxy record (typically a geophysical log) to a calculated insolation curve. Ostensibly, the process of tuning emphasizes the short period oscillations and would seem to ignore longer-period modulatory oscillations. In practice, the tuning is typically accomplished by means of a numerical algorithm that successively refines a sedimentation rate curve in order to maximize the covariance between the log and the tuning target [e.g., 84]. Since variance is simply a measure of the range of the data values, directly related to the amplitude of oscillations, it is likely that this sort of tuning method results in a match of high-amplitude intervals (i.e., modulatory cycle maxima) that is more robust than the claimed match of short-period cycles. This reliance on modulatory periods during the tuning process is explicitly described in Shackleton et al. [120]. It is arguable whether methods such as presented in Chapter 3 and in works by Hilgen [55, 56], Olsen and Kent [97] and Park and Herbert [99] that emphasize recognition of modulatory periods and deemphasize short period oscillations are more or less accurate at the 10^5-year scale than direct tuning to a target curve. The latter method clearly produces a superior temporal calibration at $\leq 10^4$-year scale, since significant sedimentation rate changes at these timescales are presumably ubiquitous given the strong Milankovitch imprint on lithology.

The problem is to incorporate the shorter-period oscillations into a "top-down" cyclostratigraphy based on longer modulatory periods, and doing so in the pre-Neogene where calculated orbital solutions cannot be expected to be accurate. A first attempt can be made by simply counting short-period cycles in geophysical logs. This is a commonly used method for producing a quick-and-dirty cyclostratigraphy in the older record [e.g., 31, 54, 95] that has some severe drawbacks due to problems of cycle recognition, especially in intervals of rapidly changing sedimentation rates (see Chapter 1). Secondary problems involve the fact that precession cycles are expected to be of variable duration and that the discrete periodicities associates with both precession and obliquity are expected to shorten with increasing age [e.g., 11].

Cycle recognition and secular changes in the orbital periods would seem to be the more dangerous problems since they lead to systematic errors that accumulate in a long record. These can be minimized through the use of an eccentricity proxy. For the late Paleocene-early Eocene records at 1051 and 690 I have made an identification of precession cycles, admittedly subjective and somewhat forced in certain intervals in order to maintain consistency with the eccentricity signal in the δ^{13}C records (Figure 5.1). In order to maintain consistency with the eccentricity signal in δ^{13}C records I adopted a mean cycle duration of 20.5 k.y. rather than 21 k.y. applicable for the last 10 m.y. [54]. It is expected that the mean duration was shorter in the Paleogene; although Berger et al.'s [11] estimate would lead to the expectation of a 0.3 k.y. rather than 0.5 k.y. difference this discrepancy can be explained by an error of only +1 cycle in every 100, or 2–3 false precession cycles recognized in the records presented here.

An obvious feature of the cycle-based sedimentation rate curves is an eccentricity-scale cyclicity in the sedimentation rates (Figure 5.1). Perhaps surprisingly, this cyclicity is completely unrelated to orbital forcing of sedimentation rates, instead reflecting the actual precession cycle duration: measured cycle durations in the orbital solution of Laskar [77, 79] also oscillate on eccentricity timescales, and the relative

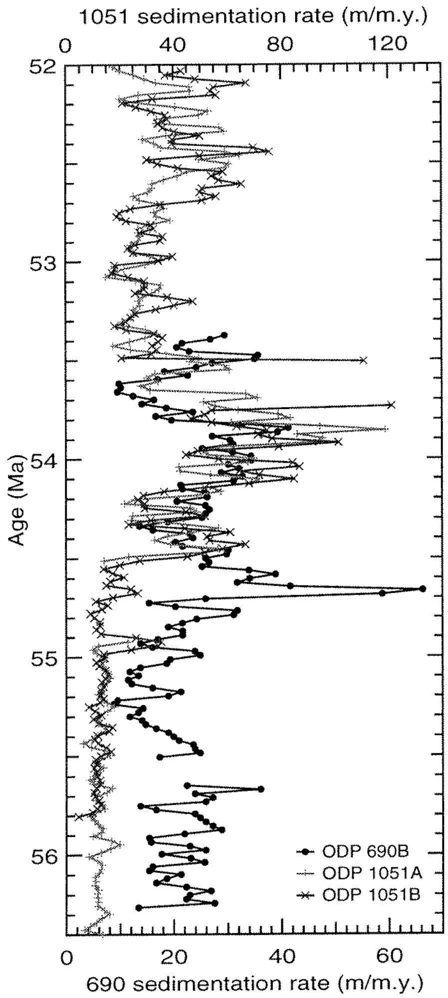

Figure 5.1: Sedimentation rates derived from ODP Sites 690 and 1051 by identifying cycles in sediment color and magnetic susceptibility logs and assuming a duration for each cycle of 20.5 k.y.

amplitude of these oscillations is similar to that observed in the records from Sites 690 and 1051 (Figure 5.2). On the one hand, this is reassuring that the cycle recognition in the geophysical logs is more or less correct (in detail the eccentricity-scale sedimentation rate cyclicity is occasionally marred, indicating either an error in cycle identification or that the records are punctuated by events that resulted in rapid sedimentation rate changes). On the other hand, this indicates that assumption of a constant cycle duration is only applicable on (long) eccentricity timescales: on shorter timescales the assumption can result in a systematic under- or over-estimate of sedimentation rates by ~25 %. Consequently, the assumption of constant cycle duration

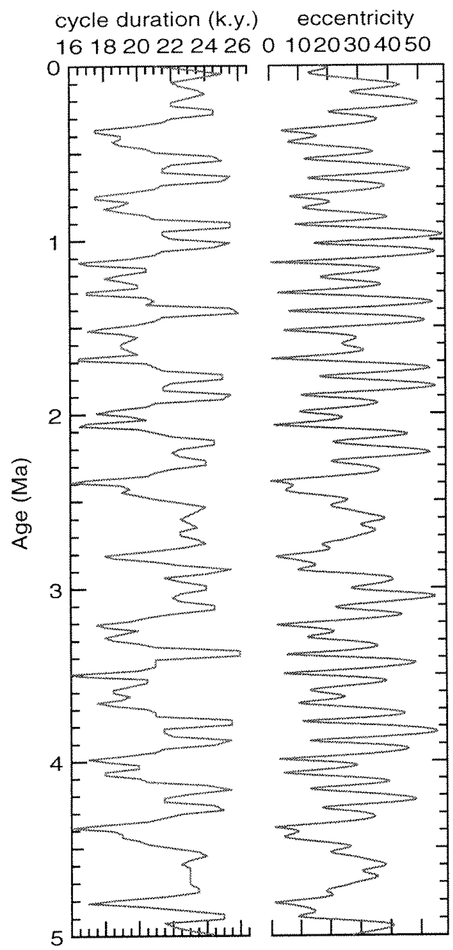

Figure 5.2: Precession cycle durations compared with the eccentricity index in the orbital solution of [79].

is not a useful one for refining the temporal calibration at $< 10^5$-year timescales. It is possible that the method could be refined to accommodate the systematic variations in expected cycle durations, either by fitting to a predicted distribution of cycle durations or by identifying a relationship between eccentricity modulation and expected precession cycle durations. It is worth noting that a significant presence of obliquity cyclicity in the proxy record will render this approach useless. Conversely, though, a proxy record showing primarily obliquity influence should be easily tuned, since obliquity cycles can be expected to be of constant duration. Unfortunately, locations in which the precession influence on insolation is irrelevant make up a tiny percentage of the Earth's surface.

An alternative approach would be to use the mean cycle duration determined by cycle counting as a constraint to generate a synthetic target curve for tuning. Again, this strategy would be made difficult by a significant presence of obliquity since it would be necessary to assume a phase relationship between the precession and obliquity signals. An equivalent procedure is to use a time-frequency decomposition, such as the wavelet transform, to simultaneously identify both the period and location of all components in the signal. Ideally, a sedimentation rate curve could be obtained from such a decomposition simply as the trace of the amplitude maximum representing a given Milankovitch component [e.g., 99]. This technique is ultimately limited only by the Heisenberg uncertainty† which sets a minimum for the combined error in simultaneous estimates of the time and frequency for components of a given signal. In other words, there is a minimum possible area for the error ellipse at each point in the time-frequency decomposition. Eventually, time-frequency decomposition will probably prove extremely useful in cyclostratigraphy, but the time-frequency decomposition techniques currently in use produce an error ellipse that is much larger than the Heisenberg minimum, and somewhat larger than would be desired to produce a high-resolution sedimentation rate estimate. For instance, the wavelet analysis presented in Chapter 2 (Figure 2.5) has a temporal error at each point of about four times the period at that point and the error in the frequency is roughly one-fourth the frequency at each point. As a result, it is impossible to see changes in the precession period on sub-eccentricity timescales, and impossible to delineate the individual frequency components of the precession band. Better methods exist, primarily driven by cutting-edge research in information technology [e.g., 141], and such algorithms are becoming less specialized and more widely available so they will likely soon be used in the analysis of geologic time series.

†sorry - I couldn't resist

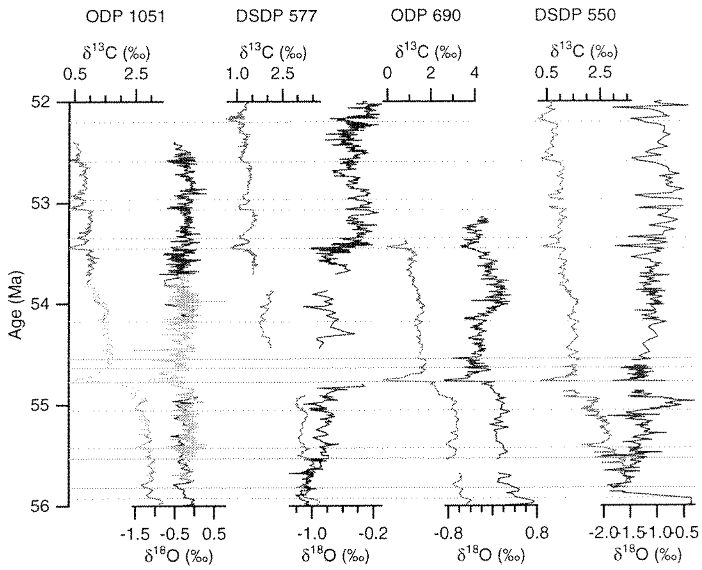

Figure 5.3: Bulk $\delta^{13}C$ and $\delta^{18}O$ records from Sites 1051, 577, 690, and 550. Horizontal lines indicate eccentricity maxima identified in the $\delta^{13}C$ records.

5.3 Carbon isotope transients: artifact or climate signal?

In Chapter 2 I raised the possibility that the eccentricity-controlled $\delta^{13}C$ transient events are wholly an artifact of the carbon residence time, unlike the P/E CIE which is accompanied by dramatic climate change. This is not necessarily true: although the transient events must in part be simply an artifact it is possible that other climatic time-lags result in an actual amplification of climate change on eccentricity timescales. If nothing else, the Pleistocene glacial cycles serve as evidence that the eccentricity modulation can somehow resonate with the climate system, most likely through some effect on the carbon cycle [e.g., 117]. Climate proxy records from the late Paleocene-early Eocene are generally not of high enough resolution or good enough quality to provide an unequivocal answer whether transient climate events accompanied the transient $\delta^{13}C$ events, but available oxygen isotope data from bulk carbonates and foraminifera suggest that water temperature did respond on eccentricity timescales.

Bulk carbonate $\delta^{18}O$ records from Sites 550, 577, and 690 show a convincing and fairly consistent short eccentricity cyclicity (Figure 5.3), with hints of transient events on long-eccentricity timescales at Site 550. Site 1051 does not show any

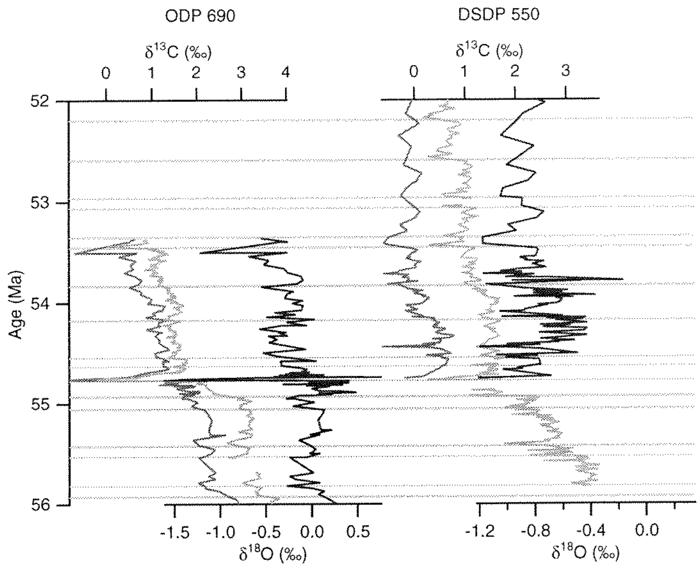

Figure 5.4: Benthic foraminiferal $\delta^{13}C$ and $\delta^{18}O$ records from Sites 690, and 550. Horizontal lines indicate eccentricity maxima identified in the bulk isotope $\delta^{13}C$ records.

obvious eccentricity-scale cyclicity in the $\delta^{18}O$ records, possibly due to diagenetic overprinting as the section was recovered from 400-500 m burial depth. The bulk sediment $\delta^{18}O$ records must be treated with some skepticism, since they may easily be affected by varying proportion of post-depositional carbonate precipitation. For instance, the fact that the long-term trend in the records from Sites 577 and 550 appear to indicate a cooling through time in an interval known to be characterized by warming is not reassuring. However, benthic foraminiferal stable isotope data support the idea that climate (or at least deep-water temperatures) responded on eccentricity timescales in the late Paleocene-early Eocene (Figure 5.4). The available records from Sites 690 and 550 are certainly affected by aliasing, but in conjunction with the bulk sediment $\delta^{13}C$ records they seem to indicate a deep-water temperature response on both short and long eccentricity timescales, including transient warmings associated with eccentricity maxima of 1–4 °C (0.25–1 ‰ $\delta^{18}O$).

5.4 Estimating residence-time from the autocovariance of δ^{13}C records

According to the explanation given in Chapter 2, the δ^{13}C record may be modeled as the convolution of an exponential decay curve, representing the residence time of carbon in the ocean-atmosphere system, with an asymmetric Milankovitch response curve. Equivalently, the δ^{13}C record should be fully characterized as

$$\delta^{13}C_t = \alpha_{\delta t}\delta^{13}C_{t-\delta t} + f\left(I_t\right) + \varepsilon_t,$$

where $\delta^{13}C_t$ is the recorded carbon isotope value at time t, $\alpha_{\delta t}$ is the autocorrelation at lag δt, $f\left(I_t\right)$ is some function of insolation that determines the relative fluxes of ^{12}C and ^{13}C, and ε_t is an error function encompassing analytic errors as well as real, non-systematic variations in carbon fluxes. By multiplying both sides of the above equation by $\delta^{13}C_t$, summing over all t, rearranging, and assuming that $f\left(I_t\right)$ and ε_t will tend to cancel in the sum, $\alpha_{\delta t}$ can be approximated as

$$\alpha_{\delta t} \approx \frac{\sum t\delta^{13}C_t\delta^{13}C_t}{\sum t\delta^{13}C_{t-\delta t}\delta^{13}C_t} = \frac{\sigma^2}{{\alpha'_{\delta t}}^2}$$

where ${\alpha'_{\delta t}}^2$ is the autocovariance at lag δt of the δ^{13}C record and σ^2 is the variance of the δ^{13}C record. The autocorrelation at lag δt can also be related to the residence time of carbon, C_{res}, as

$$\alpha_{\delta t} = 1 - \frac{\delta t}{C_{res}}.$$

In theory, the residence time may therefore be estimated by

$$C_{res} = \frac{\delta t}{1-\alpha_{\delta t}} \approx \frac{\delta t}{1-\frac{{\alpha'_{\delta t}}^2}{\sigma^2}},$$

The estimate will be quite biased because it relies on an estimate of the process mean based on the data and it does not attempt to take into account the effect of the underlying Milankovitch process. An alternate method that should decrease these biases is based on the theoretical Fourier power spectrum for "red" noise [e.g., 82]:

$$r_t = \alpha_{\delta t}r_{t-\delta t} + \varepsilon_t$$

Site	Time interval	δt (k.y.)	lag-1 autocovariance α	C_{res} (k.y.)	spectrum fit α	C_{res} (k.y.)
1051	full record	5	0.99442	897	0.97401	192
690	full record	20	0.95860	483	0.96737	613
1051	pre-CIE	5	0.93426	76	0.98318	297
690	pre-CIE	20	0.86242	145	0.95164	414
1051	post-CIE	5	0.98105	264	0.90810	54
690	post-CIE	5	0.96904	161	0.92206	64
849	Plio-Pleistocene	4	0.90321	41	0.86211	29

Table 5.1: Estimates of the residence time for carbon based on carbon isotope records from different time periods.

$$\hat{r}_f = S_0 \frac{1-\alpha^2}{1-2\alpha\cos(\pi f \delta_t)+\alpha^2}$$

where r_t is the red noise value at time t (e.g., the model discussed above without the signal component $f(I_t)$), $\hat{r}_f$ indicates the value of the Fourier power spectrum of r_t at frequency f, S_0 is the mean value of the power spectrum, and all other symbols are as above. Using a least squares technique, values for $\alpha_{\delta t}$ and S_0 can be found to fit the theoretical spectrum to the spectrum for the actual data. Since the Milankovitch signal will be represented by a narrow peak in the power spectrum the effect of Milankovitch forcing can be minimized by fitting to a median filter of the data power spectrum [e.g., 82].

I used the bulk carbonate δ^{13}C records from Sites 1051 and 690 (2) to estimate the residence time for carbon in the late Paleocene–early Eocene. For the full record of the late Paleocene-early Eocene the estimates seem extraordinarily high (Table 5.1). To determine how much of an effect the CIE has on these estimates, as well as the sensitivity of the estimate to the record length, I divided the records into pre-CIE and post-CIE intervals. These results are closer to expectation, ranging from 54 k.y. to 297 k.y. with one outlying estimate of 414 k.y., suspiciously close to the long eccentricity period. There does not seem to be any systematic relative bias between the estimates based on the lag-1 autocovariance and the fitted spectrum. For comparison, I also estimated the residence time for carbon based on a Plio-Pleistocene

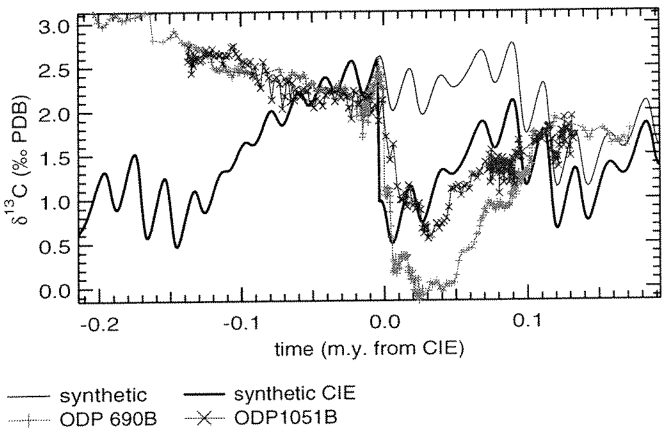

Figure 5.5: Modeled carbon isotope curve from 2.3, modified to model the CIE by adding a single point spike in the precession forcing curve. Carbon isotope records from Sites 690 and 1051 [10] are shown for comparison.

benthic foraminiferal record (Table 5.1), obtaining unreasonably low values <50 k.y. As a relatively unsophisticated attempt, all that can be said of these results is that they are generally of the right order of magnitude. The low estimates (40-70 k.y.) may indicate a stronger influence of the residence time for carbon in the ocean alone (excluding the atmosphere and biosphere) [~50 k.y., 111, 125]. A more sophisticated approach might result in more useful estimates.

5.5 Milankovitch forcing during the PETM

High resolution records through the P/E CIE show a fine-scale structure that has been interpreted as indicating several discrete methane release events [10]. However, recognition that these events are correlated to cyclicity in geophysical logs and therefore occur at ~21 k.y. intervals [109] suggests that they reflect precessional climate forcing. To investigate that possibility, I added a single-point spike to the synthetic precession curve from Chapter 2 prior to performing the convolution. The result matches the character of the high-resolution δ^{13}C curves from Sites 690 and 1051 fairly well, and several features are emphasized in the comparison (Figure 5.5):

1. In order to produce a step in the onset of the CIE the spike in the model has to be place on the increasing limb of a precession cycle. In the record from Site

690, $\delta^{13}C$ values begin to decrease prior to the most prominent abrupt shift (the record from Site 1051 in this interval cannot be evaluated due to a redeposited layer [e.g., 65]). If this decrease is the result of precession forcing, then the obvious step in the $\delta^{13}C$ record becomes enigmatic. However, it is consistent with stable isotope analyses on single-specimen planktonic foraminifera, which show an abrupt ~4 ‰ decrease in $\delta^{13}C$ coincident with the beginning of the decrease in bulk carbonate [152].

2. The second more gradual shift in the $\delta^{13}C$ records is matched in the synthetic record by the decreasing limb of a large-amplitude precession cycle at a short eccentricity maximum. In Chapter 2 I concluded that the CIE does occurs near a long eccentricity minimum and in Chapter 4 I hypothesized that the first, most abrupt $\delta^{13}C$ shift at the CIE onset resulted from input of extraterrestrial carbon via a comet impact. Based on the more detailed observations presented here two options are possible:

   The comet impact occurred near a short eccentricity maximum, increasing the apparent effects of the impact

   Global warming resulting from the comet impact resulted in dissociation of methane hydrate over several k.y., extending the effects of the impact. I have no means of differentiating between these two possibilities, which are not mutually exclusive.

3. The stepped nature of the recovery from the CIE can also be explained by precession forcing of the carbon isotope record. The apparent timing of the recovery is probably strongly dependent on the occurrence of the subsequent short eccentricity maximum, moreso than simply the residence time of carbon.

4. During the recovery from the event, the increases in δ^{13}C values are much larger than the decreases, in contrast to the synthetic record. This suggests that the CIE may have had long-term (~100 k.y.) effects on the carbon cycle.

5.6 Coda

Orbital forcing of insolation is a fundamental aspect of Earth's climate and the stratigraphy of geologic sections. Recognition of the influence of Milankovitch forcing leads to a radically different approach to paleoceanography and stratigraphy: rather than looking at the geologic record as a series of discrete events in Earth's history, the geologic record must instead be seen as a continuous time series that can be sampled at discrete intervals. Analysis of the discretely sampled continuous time series requires a level of sophistication in numerical analytical techniques previously rare in historical geology, although it must be acknowledged that these techniques are primarily useful as an investigative tool that can lead to observations that are discernible, but not obvious, in the raw data. Gaining greater sophistication in numerical analysis will inevitably lead paleoceanographers and stratigraphers to ask questions that might previously have seemed absurdly ambitious. Although some may still turn out to be unanswerable, I have posed several such questions in this synthesis chapter and outlined strategies that I believe are worth pursuing.

On a grander level, I argue that Milankovitch, moreso than the present or the Pleistocene, is the key to the past. In considering climatic enigmas such as the PETM, Mesozoic ocean anoxic events, or rapid apparent sea-level changes during a greenhouse climate it is tempting to demand information from data that is poorly understood. Esoteric geochemical measurements are published more and more frequently, but it is difficult to know whether interpretation of even the more standard measurements is sound in the context of a vastly different climate and tectonic configuration than the modern. The Milankovitch paradigm can provide a much needed predictable element in an otherwise complex mix of unconstrained assumptions. Understanding how climate proxies vary as a result of insolation changes, the amplitude of which are well constrained at any time in the past, is fundamental to interpreting changes that occur in longer intervals or at abrupt events in the geologic record.

Appendix A

Core Photo Processing

A.1 Introduction

In Chapter 1, I described a method by which usable sediment color logs could be obtained from core photographs that were not necessarily originally taken for that purpose, especially ODP and DSDP photographs. The basic principle of the method is that the background lighting effect that is unavoidable in any photograph (and imparts color changes to the photograph that do not actually exist in the sediment) can be sufficiently subdued by approximation with two third-degree polynomials, oriented horizontally and vertically with respect to the photo.

Recognizing that implementation of this algorithm presents a significant hurdle (and that the code used in completing Chapter 1, was so obtuse that even the author could have a difficult time with it) and with the hope that this use of core photos would become more widespread, I have implemented a more user friendly version of the algorithm in the "Core Photo Processing" Igor procedure file. The "user friendliness" should come from the use of a control panel within Igor that allows the user to accomplish all the necessary steps simply by moving a mouse and clicking at the right spots in the right order. As with all software, this first "release" is not as user friendly as it could be - clicking at the wrong spots in the wrong order can lead to frustrating, if not highly undesirable, results. Reference to this help file should assist the user in getting it right with minimal frustration.

In implementing this control panel I have altered somewhat the algorithm presented in Chapter 1. The biggest change (and only change significant to the result) is in the method of obtaining an approximation to the background lighting effect. In Chapter 1, this effect was approximated from the sediment portion of the photograph, using the principle that actual variations in sediment color should be uncorrelated between core sections and should therefore tend to cancel out through averaging while lighting effects should be reinforced. In the present implementation the lighting effect is approximated from the non-sediment portion of the photograph, which also allows for approximation with a two-dimensional third degree polynomial.

In part, this change is allowed by improvements in Igor's built-in image processing capabilities. In part it is allowed by improvements in my programming sophistication. However, in part I avoided this in my first implementation because the color of the tray used for taking ODP and DSDP core photos (white) is so different from the color of the sediments I was interested in. Estimating the background lighting effect in redish or dark grey sediments from a white region is not ideal. I think for the most part the problems with each method are roughly equivalent. In some cases the present method will serve much better than the previous, but in some cases the previous method will serve better. Eventually I may reintegrate the old method as an option in this package.

In an ideal world this procedure would be implemented as a stand-alone package, not requiring the user to have access to a copy of Igor. On the other hand, creating even a rudimentary software package for manipulating images is an enormous job: why reinvent the wheel when you can buy one off the shelf? Igor's programming language allows the creation of high-quality software, complete with complex graphical user interface, with very little hassle. If anyone has the desire to port this procedure to a different data analysis package or as a stand-alone, you are more than welcome to try. I doubt seriously that it is worth the effort.

Since this procedure does run within Igor, it is worth your while to understand a little bit about how Igor works. The best place to start is the Getting Started volume of the manual, the electronic version of which can be accessed through the help menu. You can also look through Learning About Igor, especially the Experiments, Files and Folders, Command Window, and Waves sections.

This procedure was developed initially on a Macintosh under OS9. It was completed and thoroughly tested on a Macintosh under OS X. It has never been tested under Windows and may require some minor alteration in the code to be usable.

A.2 Image theory

While it is possible to use this procedure without knowing what you're doing, having a rudimentary understanding of color theory and image manipulation will give a better appreciation for the output possibilities and limitations. This overview will be brief; countless references exist for a more in depth treatment. Those that I have made use of are Wyszecki and Stiles (1982) and Gonzalez and Woods (1992). Igor's Image Processing help file provides some good practical information.

A fundamental fact about color theory is that human visual perception is the primary consideration that affects every aspect of color specification and image manipulation. From defining intensity scales to compressing JPEG image files, everything about this field is done from the standpoint of the human eye and the best understanding of how images are processed by the human brain. This bias is not ideal from the standpoint of using a photograph as a scientific measuring instrument, but it is not so much a problem that we can't work around it.

From the scientific standpoint, what we are interested in is the intensity of electromagnetic radiation reflected from a rock. We recognize that it would be nice to measure not just the total intensity, but to measure the intensity in a series of ranges.

There is no a priori reason to choose one particular wavelength range over any other, but for practical reasons we are generally limited to the range of wavelengths visible to the human eye (about 400-700 nm). (Although in principle very accurate measurements could be used as mineral/elemental proxies in practice this purpose is more readily served using techniques such as X-ray fluorescence spectroscopy.) The practical reasons boil down to the fact that this is the range of interest for applications that actually make money, so the cheapest sensors (from spectrophotometers to cameras) are designed to measure light in the visual spectrum.

The main difference between a high-tech instrument like a spectrophotometer and a disposable camera is in the wavelength resolution: a spectrophotometer is capable of discriminating between wavelengths separated by 10 nm or less while photographic film divides the visual spectrum into only three 100-200 nm-wide bins. In short, the spectrophotometer will overwhelm you with data that you'll have to condense into a reasonable number of variables while a camera provides only a reasonable number of variables to begin with. The actual advantages of a spectrophotometer are better control of lighting and sensitivity to wavelengths outside the visual spectrum. The main advantage of a camera is better spatial resolution (1 mm resolution is easy to achieve).

Greyscale values as a simple measure of sediment color variations has become fairly widespread in geology, but its use has more to do with greyscale being a standard output from instruments such as spectrophotometers (e.g. the L* value published by ODP) or computer programs such as NIH Image. Greyscale is typically thought of as a measure of the lightness (or darkness) of the sediment, or a measure of the total intensity of the light reflected from the sediment. In fact greyscale (or lightness) is an empirically derived measure based on human perception. It turns out that this is a logarithmic function of intensity. While this is not a severe problem, you should be aware that a greyscale sediment log will always be a nonlinear function of sediment color. (Although a spectrophotometer makes measurements of intensity on a linear scale, by default the instrument gives readings relative to a standard lightness scale. It does seem a little backward to use a nonlinear transform when the original data was measured with a linear scale, and I doubt most researchers realize that the L* variable provided by ODP is nonlinear.)

Color data add complexity to the dataset by using three variables instead of only one. The three variables are the source of the familiar acronyms RGB (red, green, blue) and CMY (cyan, magenta, yellow - often with the addition of K for black). These are examples of tristimulus coordinate systems, which characterize color using measurements of intensity in three regions of the visible spectrum. As with lightness, each of these intensities are generally given relative to a nonlinear scale. There is a theoretical tristimulus coordinate system, termed XYZ, that can characterize every color in the visible spectrum, but no three physically realizable colors can be combined to actually form every color.

The RGB and CMY coordinate systems are fluid systems: the actual values of red, green, and blue change depending on the particular application. For instance, a CRT screen contains three phosphors for each pixel that emit light at three different wavelengths, but the red, green, and blue values for the three phosphors in a television screen are not the same as those in a computer screen. Similarly, the RGB values of inks in an inkjet printer are not the same as the values that a scanner is able to measure. Consequently, the accurate reproduction of colors involves precisely characterizing the color space, both for the tool used to obtain the image and the tool used to project the image, and correctly translating between the two.

With tristimulus color spaces each variable gives information about both intensity and wavelength. It is possible to separate the two simply by normalizing the tristimulus values to total intensity, resulting in chromaticity values (often referred to with a lowercase acronym, e.g. rgb). To fully characterize the color it is then necessary to have a lightness coordinate and two chromaticity coordinates. Spectrophotometer data from ODP are typically given in a widespread variant of this system, Lab (this is also somewhat of an unfortunate choice, since the a* and b* variables are nonlinear measurements designed to make it easy to calculate human perception of the difference between two colors). It is worth noting that, strictly speaking, the lightness parameter is not simply the sum of RGB tristimulus values: typical RGB systems have considerable overlap in wavelengths among the three coordinates so total intensity is given by a weighted sum.

If we were interested in accurately characterizing the color of a sediment sample, then all of the above considerations would lead to despair of using ODP and DSDP photographs. Too much of the process is not precisely characterized, and some things are not characterized at all. The three main problems are the lighting at the time the photo was taken, development of the negative, and reproduction as a slide. Fortunately, we are more typically interested only in the relative changes in lithology. Since there is good quality control in the development and reproduction steps, the relative changes are not affected by these (but beware slides developed in multiple batches). The main thing we have to worry about is the lighting effect.

Ambient lighting at the time of the photograph affects lightness but does not affect chromaticity. This is a very useful fact: it allows the assumption that the photographic measurement of sediment color is accurate and only the lightness is compromised. Moreover, the measured lightness is a multiplicative result of ambient lighting and the "lightness" of the object. If the ambient lighting can be sufficiently characterized, then it can be easily removed. Ideally, this effect could be ignored because a constant lighting intensity could be achieved throughout the imaged area. This is difficult to achieve, so the next best thing would be to have a simple lighting configuration, characterized by a simple mathematical function that can be fitted to a consistent background in the photo. It may seem counterintuitive, but a single light source is probably the best practical configuration, especially if the position of that light source is carefully measured. Under those circumstances, the light intensity simply decreases with the square of distance. If the positions of two or three light sources were carefully measured the correction would be fairly easy. If the positions of the light sources are unknown or if there are more than three light sources the correction is problematic, and track lighting or fluorescent tubes are completely hopeless even if the positions are well constrained.

In the case of ODP and DSDP photos there are multiple light sources whose positions relative to the field of view are unknown. Under the circumstances, I have chosen to use a two dimensional third degree polynomial to approximate the lighting background. This choice resulted from trials using various functions, some of which work well for certain photos but behave very poorly with others. For instance, a second degree polynomial can work better for a photograph where the light sources seem to be clustered, but if the sources are spaced apart it fails. A fourth degree polynomial can do a very good job for multiple light sources, but it is also prone to introducing nasty artifacts in small regions that are hard to identify in the final color log. The third degree polynomial can't fully characterize the complexity of the lighting background, but any artifacts it introduces will be evident at the scale of the full field of view rather than localized.

One final consideration has to do with the color range that is available at each step of the photograph processing. In general, every part of the imaging process responds non-linearly to intensity. The degree of nonlinearity is referred to as the gamma, defined as the slope of the line when the actual and measured intensities are plotted in a log/log plot. While we would rather not have this nonlinearity, it is not a severe problem. The severe problem is that the relationship does not go on indefinitely. With photographic film, intensities below some threshhold are recorded at a uniform minimum level while the film reaches saturation at high intensities, again recording at a constant level. Consequently, in regions of a photograph that are either too dark or too light there is information lost that cannot be resurrected through any processing technique.

A.3 Pre-processing

ODP/DSDP cores: Photographs of all ODP and DSDP cores have been taken shipboard since the beginning of DSDP. Two photographs are taken, one using black and white print film (these are reproduced in the site reports) and one using color slide film. It is worth requesting copies of the color slides. More recently, color images have been made available for download from the ODP website. I have not attempted to use these files; my hunch is that they are not well suited to this analysis.

Any scanner able to scan transparencies can be used to digitize the slides. Scanning at 1600 dpi results in a sampling resolution of $\sim$1 mm in core depth. This is obviously overkill for most applications, and is probably overly optimistic about the resolution of the photograph itself. There is no real reason not to reduce the scanning resolution to produce a log at a resolution appropriate for your application, but scanning at high resolution can give better control of the filter used to subsample the resulting log.

Most scanner software has two options for processing the digitized image. One option will allow the scanner to correct the pixel values to produce a more accurate representation of the slide colors. If the scanner has been calibrated with a standard (usually involving scanning a Kodak or other standard using special software to record the calibration values) this is probably a good thing to do. The other option will then adjust the pixel values to create a more even range of intensities. This is not a good thing to do, since the correction applied will be different for each photo depending on the sediment color.

The digitized images must be saved as TIFF files or the procedure will not see them. TIFF is the best choice in any case since it employs lossless compression techniques. JPEG and other formats that employ lossy compression techniques will result in degradation of the image, especially if they are resaved multiple times. The compression algorithm is designed, again, with human perception in mind: information is thrown out based on the likelihood that it would be perceived by a person, so that subtle differences in a uniform background (i.e., lithologic changes) are likely to be removed in order to save room for abrupt discontinuities (i.e., the edge of the core).

Other cores: This procedure file was developed to analyze ODP and DSDP photographs and it has never been tested with other photos. It should be usable even if the orientation of the core sections is not ODP/DSDP standard, but there are no guarantees. Two potential problems are the spacing between core sections (must be constant) and the background color (should be light rather than dark). In addition, if you can carefully constrain the position of the light sources when taking the photograph you will probably be able to correct for the lighting effect with a custom-made solution better than this procedure can. The digitization considerations in the ODP/DSDP section are applicable for other cores as well. If the images were taken with a digital camera, the color correction options will be available on the camera. Correction for the light quality (tungsten vs daylight, etc.) is probably a good thing.

A.4 The control panel

When the procedure is loaded it will place a "Process core photographs" option in the Macros menu. Select this option to get the control panel.

A.4.1 File Access

All of the files you want to analyze should be located in a single folder on your hard drive, CD or removable disk. That folder can be identified by clicking the Change TIFF folder button in the upper left corner of the control panel. The name of the first TIFF file will appear in the box labeled Current: and you may scroll through the files with the arrow keys to the right of that box. Clicking the button labeled

Load Image will load the current file and remove any previously loaded file. Because of the large size of the files, only one image is loaded into Igor at a time.

A.4.2 Manipulation (tabs)

Once you have loaded an image, you can manipulate that image using options grouped together on separate tabs: Geometry has controls related to orienting the photographs so the cores are vertical, Sections allows you to define the regions to be sampled, Color provides correction for lighting effects, Export allows you to save the processed files, Marquee is a poor designation for an assortment of utilities that make some of the other tasks easier to accomplish.

A.4.3 Geometry

The first step you will take is to adjust the orientation of the image and crop it. A magenta square defined the area that will be cropped when the Crop Image button is clicked. You can define the position of the edges of this square by entering values in the boxes labeled Image Top, Bottom, Left, and Right. Entering a value in the Image Rotation box will rotate the image; the value is in degrees. A good strategy is to use the section rectangles as a guide to rotate the image, then set the area of the cropping box. When setting the area of the cropping box, you'll want to exclude any dark border area but include as much of the light background area as possible in order to get a good correction for the lighting effect.

A.4.4 Sections

This is the most complex tab. A series of red rectangles with purple rectangles inset are oriented vertically and parallel across the image. The red rectangles need to be positioned to match the edges of the sections, with the top and bottom defining the section length. Positioning is accomplished by adjusting the values in the Tray Top, Tray Bottom, Tray 1 Left, and Tray separation boxes. The first two should be self explanatory. The Tray 1 Left value defines the left edge of the first section. The Tray separation value defines the distance between sections. All of these values are measured in pixels. The Number of trays value should be self explanatory.

Once the Tray Top and Tray Bottom values are set, you can enter the actual length of the sections in physical units in the Section Length box. The procedure is agnostic as to what these units are, but it is better to use the smallest practical unit (e.g. cm or decimal ft). The default value is 150, defining the length in cm of ODP/DSDP sections. You may also enter a Section Width (default value of 7 cm for ODP/DSDP) and a Sampling Width. The Sampling Width determines the region that will actually be analyzed for sediment color. Since the edges of cores are frequently affected by drilling disturbance, this width is somewhat smaller than the Section Width. For cores with severe drilling disturbance, the Sampling Width can be decreased to maximize the regions that can be analyzed.

The Scaling is calculated by dividing the difference between Tray Top and Tray Bottom by the Section Length. This in turn determines the width of the sections in pixels based on the Section Width value. Consequently, there is no point in adjusting Tray separation until after you have set the Section Length, Section Width, Tray Top, and Tray Bottom values.

The really complicated part is in the box to the left.

WARNING: When you make any adjustments to values in the two right hand columns of the Sections tab all the values in the box to the left will be reset to default values.

This box has a series of columns that allow you to define the sampling parameters for each section. The first column, Section, defines the section number. Tray defines which tray number the section is in, numbering from left to right. If a tray is empty you can uncheck the box in the Tray column to remove the purple box. Top and Bottom allow you to adjust the top and base of an individual section; values are in logging units (e.g. cm). These values should only be set if the section is shorter than standard due to recovery and if the section top is artificially low in the tray (e.g. the core catcher is sometimes placed in the same tray with the preceding section in ODP/DSDP photographs). Voids and samples are more appropriately excluded by designating a mask interval.

When the data is saved, a Sample ID will be included for each log value. The Sample ID is constructed using the name of the image file with the Section number and Top value appended, separated by dashes. For accurately translating this Sample ID into core depth, it is crucial that the Section number is correct. This is also the reason that you should not use the Top column to exclude a disturbed interval at the top of a section.

At the bottom of the list of sections (scroll down using the scroll bar to the right) there is an empty box in teh Section column. If you have more sections than trays (i.e. if two sections are placed in the same tray for the photo) you can enter a section number in this box and a full row of empty boxes will appear. You will need to specify the Tray number in addition to the Top and Base.

Further to the left in the list (scroll using the scroll bar at the bottom) there are a series of columns labeled Mask. These allow you to set up to 30 interval that should be excluded when analyzing the section. Any sampling gaps and voids should be removed. In addition, any interval of drilling disturbance should also be removed. The intervals are specified as a top and bottom separated by a dash measured in logging units (e.g. 15-20). Using this table to define mask intervals can result in an enormous headache. Fortunately (or perhaps consequently) there is an easier method in the Marquee tab.

In deciding whether or not to mask an interval of core, use the maxim that you can never have too many masks (unless you have more than 30). It is better to never take a measurement than to take a measurement that may be problematic. When calculating a log value, the procedure takes an average of all the pixel values in a row of pixels. As a result, the thin vertical crack that your Geologists eye tunes out will result in an artificial dark region extending the length of the crack. The standard deviation log can assist in identifying such regions, but it is far better if they are excluded with a mask.

A.4.5 Color

The Remove background button will remove a background lighting effect approximated by a two dimensional third degree polynomial. If the Mask trays checkbox is selected, the trays will be masked before fitting the polynomial. There is probably no reason not to select Mask trays. The algorithm also masks any dark pixels (using a cutoff of 1.5 standard deviations less than the mean). Although the Background menu allows you to select either white or black background, for the moment only a white background is supported. Selecting a black background will lead to unpredictable results.

The RGB correction button is an attempt at correcting the RGB values to more accurately reflect the sediment color by using the Kodak Q13 color scale present in ODP/DSDP photos. It works to a certain extent, but has some problems. Clicking this button opens a new window in which you are instructed to drag a marquee around the color scale (click at one corner of the color scale and drag the mouse to the other corner). After clicking Continue the marquee region is expanded and a box containing the standard Q13 color appears in the control panel. You can drag a marquee around a square in each color region in the image and select the matching color in the selection box. The average color within the marquee will appear at the right side of the selection box. It is not necessary to take a sample of every color; a minimum of three colors is necessary to perform the correction. If you use fewer than about six colors, you should probably be consistent in which six you use for every photograph from a given site. After selecting your colors and clicking Continue a dialog will ask what you want to do with the colors. You are given three options: Use to correct to standard will correct the pixel values in the image by using both a gamma correction for intensity and a tristimulus coordinate transformation for the RGB values. Correct and set new values as standard will correct the pixel values as above, but then replace the suite of standard colors with the corrected values for the colors you selected from the image. Set as standard substitutes the colors you selected as standard values but does not perform any correction.

You will notice that the performance is not spectacular. There is potential for improvement by making the algorithm more sophisticated. For now, this step is probably useful in cases where the lighting intensity varies between photographs or the photograph quality is otherwise variable. In this case you may want to use the values obtained from the first image as the standard for all subsequent images. Performance should be better matching photographs with eachother instead of matching to an absolute standard. The correction frequently will result in pixel values that are outside the range, resulting in regions of the image that appear as a uniform garish color (e.g. cyan, magenta, green, etc.). While this should not be a problem for the color log it will be a problem if you want to save the corrected image as a TIFF file. The Truncate button will replace all values outside the range with the range maximum or minimum. Do not use this button if the core itself is affected: you will produce an artificially flat region in the log. In general, only the background area will be affected; if the core is affected then you probably have problems with saturation or underexposure of the original photograph and the log will be compromised anyway.

A.4.6 Export

Before exporting the data, you'll need to select a folder to export to using the Change folder button. Then you can enter names for files that will contain the various data you may wish to export, selected using the check boxes to the left of each file name. Corrected photo will save a TIFF file with the photo as it appears on the screen.

Concatenated sections will save images of the core sections, appending each section after the previous. A Sample ID is saved as well, identifying each row of pixels using the name of the original file with the section number and pixel depth appended and separated by dashes. Color log will save the mean RGB values for each row of pixels in the section, also with a SampleID identification. The standard deviation for the averaged pixels is also saved; possible uses for the standard deviations are as weights when averaging log values to subsample the log, as quality control (although you should mask all questionable intervals before exporting the data), or as a lithologic proxy measuring the homogeneity of the sediment. Core log will save the table in the box to the right of the Sections tab. This isn't very useful at the moment; potentially it can be made useful as a log that will allow translation from Sample ID to depth in core and to facilitate reprocessing a photograph that was previously processed. The Core top depth value has no effect.

The data files are saved in Igor text data format, and they can get big. As you process successive photos, the data are appended to the same file until you enter a new name in the boxes on the Export tab. Because the files are so large it is unwieldy to open them and insert the data in the right spot. Instead, data is always appended to the end of the file along with some Igor commands that allows the full log to be reconstructed when the file is opened with Igor. One consequence is that the data files cannot be directly imported into any other program. Another consequence is that if you export the data from one photo and then realize some parameter was set wrong there is no easy way to fix the mistake. Exporting again will append a new set of data with duplicate Sample IDs to the previous set. At the moment, the easiest thing to do is to open the file in a text editor or as an Igor notebook and delete the last set of data, then resave the file before exporting again.

A.4.7 Marquee

The Marquee tab provides several utilities to ease the pain of selecting certain parameters. Many of these buttons also appear as selections in the marquee menu. To make a marquee selection, hold down the mouse button while dragging on the image. You can move the sides of the resulting rectangle by dragging one of the squares on a side or corner. When you move the cursor inside the rectangle, it will change to an upside down hat; clicking will bring up a menu with various commands that can be executed on the marquee area.

Marquee to geometry will set the magenta cropping rectangle to the edges of the current marquee. Marquee to sections will set the section top and bottom to the top and bottom of the marquee and space the sections out within the width of the marquee.

Enlarge marquee will display a second image to the right of the main image showing an enlarged area centered on the current marquee. Remove enlarged will take away the second image. The enlarged image is always displayed at the pixel resolution of the image file; the main image is a downsampled version to reduce the refresh time for the plot. As a result, using the normal Igor Expand selection in the marquee menu will result in a very blurred image. Pan up and Pan down move the enlarged image view up or down in the photo. The expanded image is useful for masking intervals: set the expanded image at the top of a section, then pan down to the bottom creating masks as you go.

Mask interval will create a mask from the top to the bottom of the marquee for the section nearest the center of the marquee. It is pretty forgiving: the marquee sides do not have to approximate the section sides and the marquee can be dragged beyond the top or bottom of the section to mask to the end of the section. Unmask interval removes a previously selected mask. It too is forgiving; the only requirement is that the center of the marquee fall within the masked interval.

sectionPost-processing After processing a series of photographs, you will end up with data stored in Igor text data format. When you open these files (use Data → Load Waves → Load Igor Text... menu option) Igor will churn for a while and finally produce a SampleID text wave and ColorLog and StDevLog waves for the color log option or a CoreImage data wave for the concatenated sections option. The data waves will all be three dimensional matrix waves, allowing you to display them as images showing the color of the core. The CoreImage wave stores a full image of all the core sections processed. The ColorLog wave stores an image representing only the average color at each level in the sections processed. In both cases, the third dimension of the matrix has three components storing each of the three color channels: red, green, and blue (in that order). See the Image Plots help file for more information.

Eventually, a few post-processing utilities may be packaged with the Core Photo Processing procedure. For now you are left to your own devices: treat these as you would any geophysical log. Two techniques are worth mentioning here, however.

This procedure reduces the lighting artifact, but cannot get rid of it. Further reduction can be attained by exploiting the fact that lighting variations affect intensities (i.e. tristimulus values) but not chromaticity values. You can therefore translate the tristimulus values to chromaticity values by dividing by total intensity and get a reduction in the lighting artifact. Technically, you should normalize to grayscale which is a weighted mean of the tristimulus values. Because of all the unconstrained color tranformations at various steps in the photographing process, it's hard to know what weights to use and an unweighted mean will provide decent results. If you want to add in weights, something like 0.3*R+0.6*G+0.1*B is probably appropriate. This technique will not work for sediment that varies mostly in shades of grey: in this case, the RGB color channels covary closely so normalizing to total intensity will destroy the signal entirely.

Principal component analysis can do an excellent job separating the lighting artifact from sediment color variations. For non-grey sediments, using PCA after transforming to chromaticity coordinates can produce a nearly artifact-free log. Since there are three color channels, you will end up with three principal components. If the strategy is applicable, the first principal component will contain the usable log, the second principal component will contain the lighting artifact (i.e., a wave with a high amplitude component with a period of 1.5 m, for ODP/DSDP cores), and the third principal component will contain low amplitude uncorrelated noise. If this interpretation doesn't make sense for the three components you get, it means either that the amplitude of the lighting artifact is of the same order as the sediment color variations or that the sediment color varies mostly in shades of grey, so that the variance due to lighting and sediment color is inseparable.

References

[1] J.R. Ali, D.V. Kent, and E.A. Hailwood. Magnetostratigraphic reinvestigation of the Palaeocene/Eocene boundary interval in Hole 690B, Maud Rise, Antarctica. *Geophysical Journal International*, 141:639–646, 2000.

[2] L.W. Alvarez, W. Alvarez, F. Asaro, and H.V. Michel. Extraterrestrial cause for the Cretaceous-Tertiary extinction. *Science*, 208:1095–1108, 1980.

[3] M.-P. Aubry. *Stratigraphic (dis)continuity and temporal resolution in the upper Paleocene-lower Eocene deep sea record.*

[4] M.-P. Aubry. Where should the Global Stratotype Section and Point (GSSP) for the Paleocene/Eocene boundary be located? *Bulletin de la Société géologique de France*, 171:461–476, 2000.

[5] M.-P. Aubry. Proposal: Global Standard Stratotype-section and Point (GSSP) at the Dababyia section (Egypt) for the Base of the Eocene Series. 2002.

[6] M.-P. Aubry, W.A. Berggren, L. Stott, and A. Sinha. The upper Paleocene-lower Eocene stratigraphic record and the Paleocene-Eocene boundary carbon isotope excursion: implications for geochronology. In R.W.O'B. Knox, R.M. Corfield, and R.E. Dunay, editors, *Correlation of the Early Paleogene in Northwest Europe, Geological Society Special Publication 101*, pages 353–380. Geological Society, London, 1996.

[7] M.-P. Aubry, B.S. Cramer, K.G. Miller, J.D. Wright, D.V. Kent, and R.K. Olsson. Late Paleocene event chronology: unconformities, not diachrony. *Bulletin de la Société géologique de France*, 171:367–378, 2000.

[8] M.-P. Aubry, S.G. Lucas, and W.A. Berggren, editors. *Late Paleocene-Early Eocene Climatic and Biotic Events in the Marine and Terrestrial Records.* Columbia University Press, New York, 1998.

[9] M.-P. Aubry and A. Sanfilippo. Late Paleocene-early Eocene sedimentary history in western Cuba: Implications for the LPTM and for regional tectonic history. *Micropaleontology*, 45:5–18, 1999.

[10] S. Bains, R.M. Corfield, and R.D. Norris. Mechanisms of climate warming at the end of the Paleocene. *Science*, 285:724–727, 1999.

[11] A. Berger, M.F. Loutre, and J. Laskar. Stability of the astronomical frequencies over the Earth's history for paleoclimate studies. *Science*, 255:560–566, 1992.

[12] W.A. Berggren and M.-P. Aubry. In R.W.O'B. Knox, R.M. Corfield, and R.E. Dunay, editors, *Correlation of the Early Paleogene in Northwest Europe, Geological Society Special Publication 101*. Geological Society, London, 1996.

[13] W.A. Berggren, D.V. Kent, C.C. Swisher, III, and M.-P. Aubry. A revised Cenozoic geochronology and chronostratigraphy. In *Geochronology, Time Scales and Global Stratigraphic Correlation, SEPM Special Publication 54*, pages 129–. SEPM (Society for Sedimentary Geology), 1995.

[14] M.-P. Bolle, T. Adatte, G. Keller, K. VonSalis, and S. Burns. The Paleocene-Eocene transition in the southern Tethys (Tunisia): Climatic and environmental fluctuations. *Bulletin de la Société géologique de France*, 170:661–680, 1999.

[15] E.W. Bolton, K.A. Maasch, and J.M. Lilly. A wavelet analysis of Plio-Pleistocene climate indicators: A new view of periodicity evolution. *Geophysical Research Letters*, 22:2753–2756, 1995.

[16] G. Bond, W. Broecker, S. Johnsen, J. McManus, L. Labeyrie, J. Jouzel, and G. Bonani. Correlations between climate records from North Atlantic sediments and Greenland ice. *Nature*, 365:143–147, 1993.

[17] G. Bond, W. Showers, M. Cheseby, R. Lotti, P. Almasi, P. deMenocal, P. Priore, H. Cullen, I. Hajdas, and G. Bonani. A pervasive millennial-scale cycle in North Atlantic Holocene and glacial climates. *Science*, 278:1257–1266, 1997.

[18] G.C. Bond, H. Heinrich, W.S. Broecker, L.D. Labeyrie, J.F. McManus, J. Andrews, S. Huon, R. Jantschik, S. Clasen, C. Simet, K. Tedesco, M. Klas, G. Bonani, and S. Ivy. Evidence for massive discharges of icebergs into the North Atlantic ocean during the last glacial period. *Nature*, 360:245–249, 1992.

[19] G.C. Bond and R. Lotti. Iceberg discharges into the North Atlantic on millenial time scales during the last glaciation. *Science*, 267:1005–1010, 1995.

[20] G.J. Bowen, P.L. Koch, P.D. Gingerich, R.D. Norris, S. Bains, and R.M. Corfield. Refined isotope stratigraphy across the continental Paleocene-Eocene boundary on Polecat Bench in the northern Bighorn Basin. In P.D. Gingerich, editor, *Paleocene-Eocene Stratigraphy and Biotic Change in the Bighorn and Clarks Fork Basins, Wyoming, University of Michigan Papers on Paleontology, No. 33*, pages 73–88. Museum of Paleontology, The University of Michigan, Ann Arbor, 2001.

[21] T.J. Bralower, D.J. Thomas, J.C. Zachos, M.M. Hirschmann, U. Röhl, H. Sigurdsson, E. Thomas, and D.L. Whitney. High-resolution records of the late Paleocene thermal maximum and circum-Caribbean volcanism: Is there a causal link? *Geology*, 25:963–966, 1997.

[22] T.J. Bralower, J.C. Zachos, E. Thomas, M. Parrow, C.K. Paull, D.C. Kelly, I. Premoli Silva, W.V. Sliter, and K.C. Lohmann. Late Paleocene to Eocene paleoceanography of the equatorial Pacific Ocean: Stable isotopes recorded at Ocean Drilling Program Site 865, Allison Guyot. *Paleoceanography*, 10:841–865, 1995.

[23] W.S. Broecker, G. Bond, M. Klas, G. Bonani, and W. Wolfli. A salt oscillator in the Glacial Atlantic? 1. The concept. *Paleoceanography*, 5:469–477, 1990.

[24] W.S. Broecker, G.C. Bond, and J.F. McManus. Heinrich events: Triggers of ocean circulation change? In W.R. Peltier, editor, *Ice in the Climate System*, volume I, pages 161–166. 1993.

[25] W.S. Broecker and T.-H. Peng. *Tracers in the Sea*. Lamont-Doherty Geological Observatory, Palisades, NY, 1982.

[26] W.S. Broecker and T.-H. Peng. Evaluation of the ^{13}C constraint on the uptake of fossil fuel CO_2 by the ocean. *Global Biogeochemical Cycles*, 7:619–626, 1993.

[27] J.V. Browning, K.G. Miller, and D.K. Pak. Global implications of lower to middle Eocene sequence boundaries on the New Jersey coastal plain: The icehouse cometh. *Geology*, 24:639–642, 1996.

[28] S.C. Cande and D.V. Kent. A new geomagnetic polarity time scale for the Late Cretaceous and Cenozoic. *Journal of Geophysical Research*, 97:13917–13951, 1992.

[29] S.C. Cande and D.V. Kent. Revised calibration of the geomagnetic polarity timescale for the Late Cretaceous and Cenozoic. *Journal of Geophysical Research*, 111:6093–6095, 1995.

[30] S.-B. R. Chang and J. L. Kirschvink. Magnetofossils, the magnetization of sediments, and the evolution of magnetite biomineralization. *Annual Review of Earth and Planetary Science*, 17:169–195, 1989.

[31] B.S. Cramer. Latest Paleocene-earliest Eocene cyclostratigraphy: using core photographs for reconnaissance geophysical logging. *Earth and Planetary Science Letters*, 186:231–244, 2001.

[32] B.S. Cramer, M.-P. Aubry, K.G. Miller, R.K. Olsson, J.D. Wright, and D.V. Kent. An exceptional chronologic, isotopic, and clay mineralogic record of the latest Paleocene thermal maximum, Bass River, NJ, ODP 174AX. *Bulletin de la Société géologique de France*, 170:883–897, 1999.

[33] B.S. Cramer, K.G. Miller, J.D. Wright, M.-P. Aubry, and R.K. Olsson. Neritic records of the late Paleocene thermal maximum from New Jersey. *GFF*, 122:38–39, 2000.

[34] S.L. D'Hondt, P. Donaghay, J.C. Zachos, D. Luttenberg, and M. Lindinger. Organic carbon fluxes and ecological recovery from the Cretaceous-Tertiary mass extinction. *Science*, 282:276–279, 1998.

[35] G.R. Dickens, M.M. Castillo, and J.C.G. Walker. A blast of gas in the latest Paleocene: Simulating first-order effects of massive dissociation of oceanic methane hydrate. *Geology*, 25:259–262, 1997.

[36] G.R. Dickens, J.R. O'Neil, D.K. Rea, and R.M. Owen. Dissociation of oceanic methane hydrate as a cause of the carbon isotope excursion at the end of the Paleocene. *Paleoceanography*, 10:965–971, 1995.

[37] G.R. Dickens, C.K. Paull, P. Wallace, and the ODP Leg 164 Scientific Party. Direct measurement of *in situ* methane quantities in a large gas-hydrate reservoir. *Nature*, 385:426–428, 1997.

[38] L. Diester-Haass. Late Eocene-Oligocene paleoceanography in the southern Indian Ocean (ODP Site 744). *Marine Geology*, 130:99–119, 1996.

[39] T. Dolenec, J. Pavsic, and S. Lojen. Ir anomalies and other elemental markers near the Palaeocene-Eocene boundary in a flysch sequence for the Western Tethys (Slovenia). *Terra Nova*, 12:199–204, 2001.

[40] D. J. Dunlop. Hysteresis properties of magnetite and their dependence on particle size: A test of pseudo-single-domain remanence models. *Journal of Geophysical Research*, 91:9569–9584, 1986.

[41] D.J. Dunlop. Superparamagnetic and single-domain threshold sizes in magnetite. *Journal of Geophysical Research*, 78:1780–1793, 1973.

[42] K.A. Farley. Cenozoic variations in the flux of interplanetary dust recorded by 3He in a deep-sea sediment. *Nature*, 376:153–156, 1995.

[43] G. Faure. John Wiley and Sons, New York, 2nd edition, 1986.

[44] B.P. Flower and J.P. Kennett. Middle Miocene deepwater paleoceanography in the southwest Pacific: Relations with East Antarctic Ice Sheet development. *Paleoceanography*, 10:1095–1112, 1995.

[45] T.G. Gibson, L.M. Bybell, and D.B. Mason. Stratigraphic and climatic implications of clay mineral changes around the Paleocene/Eocene boundary of the northeastern US margin. *Sedimentary Geology*, 134:65–92, 2000.

[46] P.D. Gingerich, editor. *Paleocene-Eocene stratigraphy and biotic change in the Bighorn and Clarks Fork Basins, Wyoming.* Museum of Paleontology, The University of Michigan, Ann Arbor.

[47] R. A. F. Grieve. Extraterrestrial impact events: the record in the rocks and the stratigraphic column. *Palaeogeography, Palaeoclimatology, Palaeoecology*, 132:5–23, 1997.

[48] T.K. Hagelberg, G.C. Bond, and P.B. deMenocal. Milankovitch band forcing of sub-Milankovitch climate variability during the Pleistocene. *Paleoceanography*, 9:545–558, 1994.

[49] T.K. Hagelberg and N.G. Pisias. Nonlinear response of Pliocene climate to orbital forcing: evidence from the eastern equatorial Pacific. *Paleoceanography*, 5:595–617, 1990.

[50] T.K. Hagelberg, N.G. Pisias, and S. Elgar. Linear and nonlinear couplings between orbital forcing and the marine δ^{18}O record during the late Neogene. *Paleoceanography*, 6:729–746, 1991.

[51] J.D. Hays, J. Imbrie, and N.J. Shackleton. Variations in the Earth's orbit: Pacemaker of the ice ages. *Science*, 194:1121–1133, 1976.

[52] T.D. Herbert. A long marine history of carbon cycle modulation by orbital-climatic changes. *Proceedings of the National Academy of Sciences*, 94:8362–8369, 1997.

[53] T.D. Herbert and S.L. D'Hondt. Precessional climate cyclicity in Late Cretaceous-Early Tertiary marine sediments: A high resolution chronometer of Cretaceous-Tertiary boundary events. *Earth and Planetary Science Letters*, 99:263–275, 1990.

[54] T.D. Herbert, I. Premoli Silva, E. Erba, and A.G. Fischer. Orbital chronology of Cretaceous-Paleocene marine sediments. In W.A. Berggren, D.V. Kent, M.-P. Aubry, and J. Hardenbol, editors, *Geochronology, Time Scales and Global Stratigraphic Correlation, SEPM Special Publication 54*, pages 81–92. SEPM (Society for Sedimentary Geology), Tulsa, OK, 1995.

[55] F.J. Hilgen. Astronomical calibration of Gauss to Matuyama sapropels in the Mediterranean and implication for the Geomagnetic Polarity Time Scale. *Earth and Planetary Science Letters*, 104:226–244, 1991.

[56] F.J. Hilgen. Extension of the astronomically calibrated (polarity) time scale to the Miocene/Pliocene boundary. *Earth and Planetary Science Letters*, 107:349–368, 1991.

[57] J. Imbrie, A.L. Berger, E.A. Boyle, S.C. Clemens, A. Duffy, W.R. Howard, G. Kukla, J. Kutzbach, D.G. Martinson, A. McIntyre, A.C. Mix, B. Molfino, J.J. Morley, L.C. Peterson, N.G. Pisias, W.L. Prell, M.E. Raymo, N.J. Shackleton, and J.R. Toggweiler. On the structure and origin of major glaciation cycles: 2. The 100,000-year cycle. *Paleoceanography*, 8:699–735, 1993.

[58] J. Imbrie, E.A. Boyle, S.C. Clemens, A. Duffy, W.R. Howard, G. Kukla, J. Kutzbach, D.G. Martinson, A. McIntyre, A.C. Mix, B. Molfino, J.J. Morley, L.C. Peterson, N.G. Pisias, W.L. Prell, M.E. Raymo, N.J. Shackleton, and J.R. Toggweiler. On the structure and origin of major glaciation cycles: 1. Linear responses to Milankovitch forcing. *Paleoceanography*, 7:701–738, 1992.

[59] J. Imbrie, J.D. Hays, D.G. Martinson, A. McIntyre, A.C. Mix, J.J. Morley, N.G. Pisias, W.L. Prell, and N.J. Shackleton. The orbital theory of Pleistocene climate: Support from a revised chronology of the marine $\delta^{18}O$ record. pages 269–305. D. Reidel Publishing Company, 1984.

[60] L. F. Jansa, G. Pe-Piper, P. B. Robertson, and O. Friedenreich. Montagnais: A submarine impact structure on the Scotian Shelf, Eastern Canada. *Geological Society of America Bulletin*, 101:450–463, 1989.

[61] E. Jessberger, K., and J. Kissel. Chemical properties of cometary dust and a note on carbon isotopes. In R.L.J. Newburn and et al., editors, *Comets in the Post-Halley Era*, pages 1075–1092. Kluwer Academic Publishers, Amsterdam, 1991.

[62] Y.G. Jin, Y. Wang, W. Wang, Q.H. Shang, C.Q. Cao, and D.H. Erwin. Pattern of marine mass extinction near the Permian-Triassic boundary in south China. *Science*, 289:432–436, 2000.

[63] K. Kaiho, T. Arinobu, R. Ishiwatari, H.E.G. Morgans, H. Okada, N. Takeda, K. Tazaki, G. Zhou, Y. Kajiwara, R. Matsumoto, A. Hirai, N. Niitsuma, and H. Wada. Latest Paleocene benthic foraminiferal extinction and environmental changes at Tawanui, New Zealand. *Paleoceanography*, 11:447–465, 1996.

[64] M.E. Katz, B.S. Cramer, G.S. Mountain, S. Katz, and K.G. Miller. Uncorking the bottle: What triggered the Paleocene-Eocene thermal maximum methane release? *Paleoceanography*, 16:549–562, 2001.

[65] M.E. Katz, D.K. Pak, G.R. Dickens, and K.G. Miller. The source and fate of massive carbon input during the latest Paleocene thermal maximum. *Science*, 286:1531–1533, 1999.

[66] D. C. Kelly, T. J. Bralower, J. C. Zachos, I. Premoli-Silva, and E. Thomas. Rapid diversification of planktonic foraminifera in the tropical Pacific (ODP Site 865) during the late Paleocene thermal maximum. *Geology*, 24:423–426, 1996.

[67] J.P. Kennett and L.D. Stott. Abrupt deep-sea warming, palaeceanographic changes and benthic extinctions at the end of the Palaeocene. *Nature*, 353:225–229, 1991.

[68] D.V. Kent, B.S. Cramer, and L. Lanci. Evidence of an Impact Trigger for the Paleocene/Eocene Thermal Maximum and Carbon Isotope Excursion. *Eos, Transactions of the American Geophysical Union*, 62:PP32A–0509, 2001.

[69] J. F. Kerridge. Carbon, hydrogen and nitrogen in carbonaceous chondrites: Abundances and isotopic compositions in bulk samples. *Geochimica et Cosmochimica Acta*, 49:1707–1714, 1985.

[70] J.L. Kirschvink. The least-squares line and plane and the analysis of palaeomagnetic data. *Geophysical Journal of the Royal Astronomical Society*, 62:699–718, 1980.

[71] R.W.O'B. Knox, R.M. Corfield, and R.E. Dunay, editors. *Correlation of the Early Paleogene in Northwest Europe*. Geological Society, Special Publication 101, London, 1996.

[72] P.L. Koch, J.C. Zachos, and D.L. Dettman. Stable isotope stratigraphy and paleoclimatology of the Paleogene Bighorn Basin (Wyoming, USA). *Palaeogeography, Palaeoclimatology, Palaeoecology*, 115:61–89, 1995.

[73] P.L. Koch, J.C. Zachos, and P.D. Gingerich. Correlation between isotope records in marine and continental carbon reservoirs near the Palaeocene/Eocene boundary. *Nature*, 358:319–322, 1992.

[74] F.T. Kyte and J.T. Wasson. Accretion rate of extraterrestrial matter: Iridium deposited 33 to 67 million years ago. *Science*, 232:1225–1229, 1986.

[75] L. Lanci and D.V. Kent. Introduction of thermal activation in forward modeling of SD hysteresis loops and implications for the interpretation of the Day diagrams. *Journal of Geophysical Research*, page in press, 2002.

[76] L. Lanci, D.V. Kent, and K.G. Miller. Detection of sequence boundaries using core-log integrateion of magnetic susceptibility and natural gamma-ray measurements at the Ancora site on the Atlantic Coastal Plain. *Journal of Geophysical Research*, in press.

[77] J. Laskar. The chaotic motion of the Solar System: a numerical estimate of the size of the chaotic zones. *Icarus*, 88:266–291, 1990.

[78] J. Laskar. The limits of Earth orbital calculations for geological time-scale use. *Philosophical Transactions of the Royal Society, London, A*, 357:1735–1759, 1999.

[79] J. Laskar, F. Joutel, and F. Boudin. Orbital, precessional, and insolation quantities for the Earth from -20 Myr to +10 Myr. *Astronomy and Astrophysics*, 270:522–533, 1993.

[80] L.J. Lourens and F.J. Hilgen. Long-periodic variations in the Earth's obliquity and their relation to third-order eustatic cycles and Late Neogene glaciations. *Quaternary International*, 40:43–52, 1997.

[81] M.C. Maas, M.R.L. Anthony, P.D. Gingerich, G.F. Gunnell, and D.W. Krause. Mammalian generic diversity and turnover in the Late Paleocene and Early Eocene of the Bighorn and Crazy Mountain Basins, Wyoming and Montana (USA). *Palaeogeography, Palaeoclimatology, Palaeoecology*, 115:181–207, 1995.

[82] M.E. Mann and J.M. Lees. Robust estimation of background noise and signal detection in climatic time series. *Climatic Change*, 33:409–445, 1996.

[83] E. Martini. *Standard Tertiary and Quaternary calcareous nannoplankton zonation*, volume Proceedings of the Second Planktonic Conference, pages 739–761. 1971.

[84] D.G. Martinson, W. Menke, and P. Stoffa. An inverse approach to signal correlation. *Journal of Geophysical Research*, 87:4807–4818, 1982.

[85] M.A. Maslin, X.S. Li, M.-F. Loutre, and A.L. Berger. The contribution of orbital forcing to the progressive intensification of Northern Hemisphere glaciation. *Quaternary Science Reviews*, 17:411–426, 1998.

[86] J.F. McManus, G.C. Bond, W.S. Broecker, S.M. Higgins, and M.Q. Fleischer. Heinrich events associated with glacial terminations. *Eos, Transactions of the American Geophysical Union*, 1994.

[87] J.F. McManus, D.W. Oppo, and J.L. Cullen. A 0.5-million-year record of millennial-scale climate variability in the North Atlantic. *Science*, 283:971–975, 1999.

[88] G.A. Mead. Correlation of Cenozoic-Late Cretaceous geomagnetic polarity time scales: An Internet archive. *Journal of Geophysical Research*, 101:8107–8109, 1996.

[89] S. Messenger. Identification of molecular-cloud material in interplanetary dust particles. *Nature*, 404:968–971, 2000.

[90] K.G. Miller and R.G. Fairbanks. Oligocene to Miocene carbon isotope cycles and abyssal circulation changes. In *The Carbon Cycle and Atmospheric CO_2: Natural Variations Archean to Present*, volume 32 of *Geophysical Monograph*, pages 469–486. American Geophysical Union, 1985.

[91] K.G. Miller, T.R. Janecek, M.E. Katz, and D.J. Keil. Abyssal circulation and benthic foraminiferal changes near the Paleocene/Eocene boundary. *Paleoceanography*, 2:741–761, 1987.

[92] K.G. Miller, P.J. Sugarman, J.V. Browning, B.S. Cramer, R.K. Olsson, L. de Romero, M.-P. Aubry, S.F. Pekar, M.D. Georgescu, K.T. Metzger, D.H. Monteverde, E.S. Skinner, J. Uptegrove, L.G. Mullikin, F.L. Muller, M.D. Feigenson, T.J. Reilly, G.J. Brenner, and D. Queen. Ancora Site. *Proceedings of the Ocean Drilling Program, Initial Reports*, 174AX (Suppl.):1–65 [Online], 1998.

[93] K.G. Miller, P.J. Sugarman, J.V. Browning, R.K. Olsson, S.F. Pekar, T.J. Reilly, B.S. Cramer, M.-P. Aubry, R.P. Lawrence, J. Curran, M. Stewart, J.M. Metzger, J. Uptegrove, D. Bukry, L.H. Burckle, J.D. Wright, M.D. Feigenson,

G.J. Brenner, and R.F. Dalton. Bass River Site. *Proceedings of the Ocean Drilling Program, Initial Reports*, 174AX:5–43, 1998.

[94] A. J. Newell and R. T. Merrill. Size dependence of hysteresis properties of small pseudo-single-domain grains. *Journal of Geophysical Research*, 105, 2000.

[95] R.D. Norris and U. Röhl. Carbon cycling and chronology of climate warming during the Palaeocene/Eocene transition. *Nature*, 401:775–778, 1999.

[96] J.G. Ogg and L. Bardot. Aptian through Eocene magnetostratigraphic correlation of the Blake Nose Transect (Leg 171B), Florida continental margin. *Proceedings of the Ocean Drilling Program, Scientific Results*, 171B:1–58, 2001.

[97] P.E. Olsen and D.V. Kent. Milankovitch climate forcing in the tropics of Pangaea during the Late Triassic. *Palaeogeography, Palaeoclimatology, Palaeoecology*, 122:1–26, 1996.

[98] D. Paillard. The timing of Pleistocene glaciations from a simple multiple-state climate model. *Nature*, 391:378–381, 1998.

[99] J. Park and T.D. Herbert. Hunting for paleoclimatic periodicities in a geologic time series with an uncertain time scale. *Journal of Geophysical Research*, 92:14027–14040, 1987.

[100] Shipboard Scientific Party. Site 1051. *Proceedings of the Ocean Drilling Program, Initial Reports*, 171B:171–239, 1998.

[101] W.J. Pegram and K.K. Turekian. The osmium isotopic composition change of Cenozoic sea water as inferred from a deep-sea core corrected for meteoritic contributions. *Geochimica et Cosmochimica Acta*, 63:4053–4058, 1999.

[102] N.G. Pisias and J. Imbrie. Orbital geometry, CO_2, and Pleistocene climate. pages 43–49.

[103] C. W. Poag, D. S. Powars, L. J. Poppe, and R. B. Mixon. Meteoroid mayhem in Ole Virginny: Source of the North American tektite strewn field. *Geology*, 22:691–694, 1994.

[104] C.W. Poag. Roadblocks on the kill curve: Testing the Raup hypothesis. *Palaios*, 12:582–590, 1997.

[105] J.J. Pospichal and S.W. Wise. Paleocene to middle Eocene calcareous nannofossils of ODP Sites 689 and 690, Maud Rise, Weddell Sea. *Proceedings of the Ocean Drilling Program, Scientific Results*, 113:613–666, 1990.

[106] G. Ravizza, R.N. Norris, J. Blusztajn, and M.-P. Aubry. An osmium isotope excursion associated with the late Paleocene thermal maximum: Evidence of intensified chemical weathering. *Paleoceanography*, 16:155–163, 2001.

[107] P.R. Renne, A.L. Deino, R.C. Walter, B.D. Turrin, C.C. Swisher, T.A.G. Becker, H. Curtis, W.D. Sharp, and A.R. Jaouni. Intercalibration of astronomical and radioisotopic time. *Geology*, 22:783–786, 1994.

[108] C. Robert and J.P. Kennett. Antarctic subtropical humid episode at the Paleocene-Eocene boundary: Clay-mineral evidence. *Geology*, 22:211–214, 1994.

[109] U. Röhl, T.J. Bralower, R.D. Norris, and G. Wefer. New chronology for the late Paleocene thermal maximum and its environmental implications. *Geology*, 28:927–930, 2000.

[110] D.L. Royer, R.A. Berner, and D.J. Beerling. Phanerozoic atmospheric CO_2 change: evaluating geochemical and paleobiological approaches. *Earth-Science Reviews*, 54:349–392, 2001.

[111] J.L. Sarmiento and M. Bender. Carbon biogeochemistry and climate-change. *Photosynthesis Research*, 39:209–234, 1994.

[112] B. Schmitz and F. Asaro. Iridium geochemistry of volcanic ash layers from the early Eocene rifting of the northeastern North Atlantic and some other Phanerozoic events. *Geological Society of America Bulletin*, 108:489–504, 1996.

[113] B. Schmitz, F. Asaro, E. Molina, S. Monechi, K. von Salis, and R.P. Speijer. High-resolution iridium, $\delta^{13}C$, $\delta^{18}O$, foraminifera and nannofossil profiles across the latest Paleocene benthic extinction event at Zumaya, Spain. *Palaeogeography, Palaeoclimatology, Palaeoecology*, 133:49–68, 1997.

[114] B. Schmitz, R.P. Speijer, and M.-P. Aubry. Latest Paleocene benthic extinction event on the southern Tethyan shelf (Egypt): Foraminiferal stable isotopic ($\delta^{13}C$, $\delta^{18}O$) records. *Geology*, 24:347–350, 1996.

[115] B. Schmitz, B. Sundquist, and F.P. Andreasson. Thematic issue on Early Paleogene Warm Climates and Biosphere Dynamics. *GFF*, 122:1–192, 2000.

[116] N.J. Shackleton. The carbon isotope record of the Cenozoic: history of organic carbon burial and of oxygen in the ocean and atmosphere. In J. Brooks and A.J. Fleet, editors, *Marine Petroleum Source Rocks, Geological Society Special Publication 26*, pages 423–434. Geological Society, London, 1987.

[117] N.J. Shackleton. The 100,000-year ice-age cycle identified and found to lag temperature, carbon dioxide, and orbital eccentricity. *Science*, 289:1897–1902, 2000.

[118] N.J. Shackleton, A.L. Berger, and W.R. Peltier. An alternative astronomical calibration of the lower Pleistocene timescale based on ODP Site 677. *Transactions of the Royal Society of Edinburgh: Earth Sciences*, 81:251–261, 1990.

[119] N.J. Shackleton, S. Crowhurst, T. Hagelberg, N.G. Pisias, and D.A. Schneider. A new Late Neogene time scale: application to Leg 138 Sites. *Proceedings of the Ocean Drilling Program, Scientific Results*, 138:73–101, 1995.

[120] N.J. Shackleton, S.J. Crowhurst, G.P. Weedon, and J. Laskar. Astronomical calibration of Oligocene-Miocene time. *Philosophical Transactions of the Royal Society of London*, 357:1907–1929, 1999.

[121] N.J. Shackleton, M.A. Hall, and U. Bleil. Carbon-isotope stratigraphy, Site 577. *Initial Reports of the Deep Sea Drilling Project*, 86:503–511, 1985.

[122] N.J. Shackleton, M.A. Hall, I. Raffi, L. Tauxe, and J. Zachos. Astronomical calibration age for the Oligocene-Miocene boundary. *Geology*, 28:447–450, 2000.

[123] E. M. Shoemaker, R. F. Wolfe, and C. S. Shoemaker. Asteroid and comet flux in the neighborhood of Earth. In V. L. Sharpton and P. D. Ward, editors, *Global catastrophes in Earth history, Special Paper 247*, pages 155–170. Geological Society of America, Boulder, CO, 1990.

[124] U. Siegenthaler. Modeling the present-day oceanic carbon cycle. In M. Heimann, editor, *The Global Carbon Cycle, NATO ASI Series I, 15*, pages 367–395. NATO, 1993.

[125] U. Siegenthaler and J.L. Sarmiento. Atmospheric carbon dioxide and the ocean. *Nature*, 365:119–125, 1993.

[126] L.D. Stott and J.P. Kennett. Antarctic Paleogene planktonic foraminifer biostratigraphy: ODP Leg 113, Sites 689 and 690. *Proceedings of the Ocean Drilling Program, Scientific Results*, 113:549–562, 1990.

[127] L.D. Stott, A. Sinha, M. Thiry, M.-P. Aubry, and W.A. Berggren. Global δ^{13}C changes across the Paleocene-Eocene boundary: criteria for terrestrial-marine correlations. In R.W.O'B. Knox, R.M. Corfield, and R.E. Dunay, editors, *Correlation of the Early Paleogene in Northwest Europe, Geological Society Special Publication 101*, pages 381–399. The Geological Society, London, 1996.

[128] C.C. Swisher, J.M. Grajales-Nishimura, A. Montanari, S.V. Margolis, P. Claeys, W. Alvarez, P. Renne, E. Cedillo-Pardo, F.L.M.R. Maurasse, G.H. Curtis, J. Smit, and M.O. McWilliams. Coeval ^{40}Ar/^{39}Ar ages of 65.0 million years ago from Chicxulub Crater melt rock and Cretaceous-Tertiary boundary tektites. *Science*, 257:954–958, 1992.

[129] C.C. Swisher, III and R.W.O'B Knox. The age of the Paleocene/Eocene boundary: ^{40}Ar/^{39}Ar dating of the lower part of NP10, North Sea Basin and Denmark, 1991.

[130] L. Tauxe, T. A. T. Mullender, and T. Pick. Potbellies, wasp-waists, and superparamagnetism in magnetic hysteresis. *Journal of Geophysical Research*, 101:571–583, 1996.

[131] M. Thiry. Palaeoclimatic interpretation of clay minerals in marine deposits: an outlook from the continental origin. *Earth-Science Reviews*, 49:201–221, 2000.

[132] D.J. Thomas, T.J. Bralower, and J.C. Zachos. New evidence for subtropical warming during the late Paleocene thermal maximum: Stable isotopes from Deep Sea Drilling Project Site 527, Walvis Ridge. *Paleoceanography*, 14:561–570, 1999.

[133] E. Thomas and N.J. Shackleton. The Paleocene-Eocene benthic foraminiferal extinction and stable isotope anomalies. In R.W.O'B. Knox, R.M. Corfield, and R.E. Dunay, editors, *Correlation of the Early Paleogene in Northwest Europe, Geological Society, Special Publication 101*, pages 401–441. The Geological Society, London, 1996.

[134] E. Thomas, J.C. Zachos, and T.J. Bralower. Deep-sea environments on a warm earth: latest Paleocene-early Eocene. In B.T. Huber, K.G. MacLeod, and S.L. Wing, editors, *Warm Climates in Earth History*, pages 132–160. Cambridge University Press, Cambridge, U.K., 2000.

[135] K. L. Thomas, G. E. Blanford, L. P. Keller, W. Klock, and D. S. McKay. Carbon abundance and silicate mineralogy of anhydrous interplanetary dust particles. *Geochemica Cosmochemica Acta*, 57:1551–1556, 1993.

[136] C. Torrence and G.P. Compo. A practical guide to wavelet analysis. *Bulletin of the American Meteorological Society*, 79:61–78, 1998.

[137] H.C. Verma, C. Upadhyay, R.P. Tripathi, A. Tripathi, A.D. Shukla, and N. Bhandari. Nano-sized iron phases at the K/T and P/T boundaries revealed by Mössbauer spectroscopy. *Lunar and Planetary Science*, 32:1270.pdf, 2001.

[138] E. Vincent and W.H. Berger. Carbon dioxide and polar cooling in the Miocene; the Monterey Hypothesis. In E.T. Sundquist and W.S. Broecker, editors, *The Carbon Cycle and Atmospheric CO_2: Natural Variations Archean to Present, Geophysical Monograph, 32*, pages 455–468. American Geophysical Union, Washington, DC, 1985.

[139] T.J. Wdowiak, L.P. Armendarez, D.G. Agresti, M.L. Wade, S.Y. Wdowiak, P. Claeys, and G. Izett. Presence of an iron-rich nanophase material in the upper layer of the Cretaceous-Tertiary boundary clay. *Meteoritics and Planetary Science*, 36:123–133, 2001.

[140] G.P. Weedon, N.J. Shackleton, and P.N. Pearson. The Oligocene time scale and cyclostratigraphy on the Ceara Rise, Western Equatorial Atlantic. *Proceedings of the Ocean Drilling Program, Scientific Results*, 154:101–114, 1997.

[141] M.V. Wickerhauser. *Adapted Wavelet Analysis from Theory to Software*. A K Peters, Ltd., Wellesley, MA, 1994.

[142] P. Wilde and M.S. Quinby-Hunt. Collisions with ice/volatile objects: Geological implications A qualitative treatment. *Palaeogeography, Palaeoclimatology, Palaeoecology*, 132:47–63, 1997.

[143] S.L. Wing, P.D. Gingerich, E. Thomas, and B. Schmitz, editors. *Causes and Consequences of Globally Warm Climates in the Early Paleocene.* Geological Society of America, in press.

[144] M. Winklhofer, K. Fabian, and F. Heider. Magnetic blocking temperatures of magnetite calculated with a three-dimensional micromagnetic model. *Journal of Geophysical Research*, 102, 1997.

[145] F. Woodruff and S.M. Savin. Mid-Miocene isotope stratigraphy in the deep sea: High-resolution correlations, paleoclimatic cycles, and sediment preservation. *Paleoceanography*, 6:755–806, 1991.

[146] G. Wyszecki and W.S. Stiles. *Color Science: Concepts and Methods, Quantitative Data and Formulae.* John Wiley and Sons, New York, 2nd edition, 1982.

[147] J. Zachos, M. Pagani, L. Sloan, E. Thomas, and K. Billups. Trends, rhythms, and aberrations in global climate 65 Ma to Present. *Science*, 292:686–693, 2001.

[148] J.C. Zachos, B.P. Flower, and H. Paul. Orbitally paced climate oscillations across the Oligocene/Miocene boundary. *Nature*, 388:567–570, 1997.

[149] J.C. Zachos, K.C. Lohmann, J.C.G. Walker, and S.W.J. Wise. Abrupt climate change and transient climates during the Paleogene: A marine perspective. *The Journal of Geology*, 101:191–213, 1993.

[150] J.C. Zachos, T.M. Quinn, and K.A. Salamy. High-resolution (104 years) deep-sea foraminiferal stable isotope records of the Eocene-Oligocene climate transition. *Paleoceanography*, 11:251–266, 1996.

[151] J.C. Zachos, N.J. Shackleton, J.S. Revenaugh, H. Pälike, and B.P. Flower. Climate response to orbital forcing across the Oligocene-Miocene Boundary. *Science*, 292:274–278, 2001.

[152] J.C. Zachos, D. Thomas, T. Bralower, and E. Thomas. New constraints on the timing and magnitude of the Paleocene-Eocene boundary carbon isotope excursion in marine environments. *Eos, Transactions of the American Geophysical Union*, 62:PP31B–07, 2001.

CURRICULUM VITA
Benjamin Stovall Cramer

Education

1995	Columbia College of Columbia University, Geology/Russian, A.B. *cum laude*
1998	Rutgers University, Geological Sciences, M.S.
2002	Rutgers University, Geological Sciences, Ph.D.

Professional Experience

1995	Cruise, R/V Ewing, hydrothermal fluid flow, Juan de Fuca Ridge.
1995	Research assistant to P.B. deMenocal, Lamont-Doherty Earth Observatory.
1996-1998	Teaching assistant (Intro. Geology Lab, Stratigraphy Lab), Rutgers University.
1996-2000	Sedimentologist, NJ Coastal Plain Drilling Project, ODP Leg 174AX.
1998	Cruise, R/V Cape Hatteras, multi- and single channel seismics.
1999	Lecturer, Honors Intro. Geology Lab, Rutgers University.
1998-2001	NSF Graduate Research Fellow, Rutgers University.
2001-2002	Lecturer, Geological Modeling, Rutgers University.
2001-2002	Schlanger Ocean Drilling Fellow, Rutgers University.

Publications

Cramer, B.S., M.-P. Aubry, K.G. Miller, R.K. Olsson, J.D. Wright and D.V. Kent, An exceptional chronologic, isotopic, and clay mineralogic record of the latest Paleocene thermal maximum, Bass River, NJ, ODP 174AX, Bulletin de la Société géologique de France, 170, p. 883-897, 1999.

Aubry, M.-P., B.S. Cramer, K.G. Miller, J.D. Wright, D.V. Kent and R.K. Olsson, Late Paleocene event chronology; unconformities, not diachrony, Bulletin de la Société géologique de France , 171, 367-378, 2000.

Cramer, B.S., Latest Paleocene-earliest Eocene cyclostratigraphy: using core photographs for reconnaissance geophysical logging, Earth and Planetary Science Letters, 186, 231-244, 2001.

Katz, M.E., G.S. Mountain, B.S. Cramer, S. Katz and K.G. Miller, Uncorking the bottle: did thermal dissociation or mechanical disruption trigger the latest Paleocene methane release?, Paleoceanography, 16, 549-562, 2001.